



Hydroclimate response in Texas and Gulf of Mexico to rapid warming during the last deglacial: High-resolution speleothem proxy and monitoring evidence

Nathan Miller ^{a, *}, Jay Banner ^a, Weimin Feng ^b, Angelique Gonzales ^c, Reinhard Kozdon ^{d, e}

^a Jackson School of Geosciences, University of Texas at Austin, Austin, TX, 78712, USA

^b Department of Physics, Astronomy, Geosciences and Engineering Technology, Valdosta State University, Valdosta, GA, 31698, USA

^c Department of Geology, Cornell College, Mount Vernon, IA, 52314, USA

^d Lamont-Doherty Earth Observatory, Palisades, NY, 10964, USA

^e WiscSIMS, Department of Geoscience, University of Wisconsin, Madison, WI, 53706, USA

ARTICLE INFO

Article history:

Received 25 July 2021

Received in revised form

9 October 2021

Accepted 14 October 2021

Available online xxx

Handling Editor: Mira Matthews

Keywords:

Speleothem

Deglacial climate change

Proxy

Texas

High resolution $\delta^{18}\text{O}$ and imaging

Growth fabric

Bølling-Allerød

Gulf of Mexico

ABSTRACT

Cave calcite (i.e., speleothem) proxy records that span abrupt warming events, such as those of the last deglacial, may prologue regional responses of hydroclimate to 21st century warming. Proxy reliability is advanced by an understanding of the modern hydrologic system and controls on calcite growth. Here we integrate monitoring of Cave CWN in central Texas with high-resolution imaging and $\delta^{18}\text{O}$ analysis of Stalagmite CWN-4 to understand how regional hydroclimate changed during a rapid deglacial warming event - the transition from Heinrich Stadial 1 (HS1) to the Bølling-Allerød (BA) warm period. This event is recorded in CWN-4 as a rapid negative $\delta^{18}\text{O}$ excursion of 1.7‰ over ~210 years (HS1-BA $\delta^{18}\text{O}$ excursion = 'HBO'), followed by a 6-fold growth rate increase.

Monitoring demonstrates that modern calcite grows during cool seasons, growth rates follow drip rate, and drip water and calcite $\delta^{18}\text{O}$ reflect the $\delta^{18}\text{O}$ of recharge. Because drip waters have interannual epikarst residence times, their $\delta^{18}\text{O}$ values are well-mixed averages of their Gulf of Mexico (GoM) moisture source $\delta^{18}\text{O}$ values, which rapidly decreased during Laurentide Ice Sheet (LIS) melting events. Confocal laser fluorescence microscopy imaging indicates that growth lamina are seasonal within U-series age constraints. The timing of the HBO (14.75 ± 0.08 to 14.54 ± 0.08 ka), corresponds with 1) the onset of Bølling warming in Greenland (14.64 ka), 2) AMOC reinvigoration (~14.61–14.25 ka), 3) Meltwater Pulse 1a (14.65–14.31 ka), and 4) Meltwater Flood 3 (MWF-3) - the most intense episode of LIS meltwater discharge into the GoM (14.97–14.46 ka). The rapid increase in growth rates following the HBO indicates an abrupt transition to a wetter hydroclimate in central Texas following these regional and global events.

The HBO $\delta^{18}\text{O}$ excursion occurred monotonically, consistent with meltwater discharge being continuous. This excursion also corresponds with climate change recognized across the HS1-BA transition in marine and terrestrial records influenced by changes in North Atlantic climate, AMOC, and ITCZ migrations. We infer that central Texas deglacial hydroclimate largely followed changes in AMOC, linked via meltwater input to the GoM. Periods of fast (slow) speleothem growth coincide with warmer (cooler) North Atlantic episodes, with the exception of the HS1 to BA transition. For this transition, slow growth rates during MWF-3 may reflect protracted cooling of GoM SST and corresponding atmospheric moisture reduction. The common timing and duration of the HBO with shifts toward wetter conditions across the HS1-BA transition in many northern Hemisphere climate records supports common ocean-atmosphere teleconnections related to AMOC intensity.

© 2021 Elsevier Ltd. All rights reserved.

1. Introduction

Reconstructing past sources and amounts of moisture delivered to terrestrial environments is significant for the Southwest US,

* Corresponding author.

E-mail address: nrmiller@jsg.utexas.edu (N. Miller).

which will face increasing water sustainability challenges with atmospheric warming during the 21st Century (Nielsen-Gammon et al., 2020; Cook et al., 2015). Climate records from such climate-sensitive, drought-prone regions during times of past warming offer perspectives for how hydroclimate changed during comparable warming events. Whereas the Pliocene and Eocene are useful analogs for the magnitude of 21st century warming (Burke et al., 2018), the last deglacial period provides proxies with sufficient chronologic control to resolve a similar rate of warming as that projected for the 21st century (Masson-Delmotte et al., 2013). Cave calcite deposits (speleothems) have become widely applied as proxies of hydroclimate. Uranium-series methods provide absolute, high-resolution ages that constrain growth rates, and in favorable cases regular alternations of growth banding or chemical/isotopic compositions elucidate seasonal resolution (e.g., Shopov et al., 1994; Genty and Quinif, 1996; Baker et al., 2008, 2015; Carlson et al., 2018). Oxygen isotopes and other geochemical parameters in speleothems are used to reconstruct temporal changes in parameters such as moisture source and moisture amount (e.g., Lachniet, 2009; Feng et al., 2012, 2014a; Orland et al., 2015). Along with these features come uncertainties in terms of the accuracy of proxy interpretation, resulting from potential non-equilibrium isotope effects, multiple processes governing a given proxy, and the lack of proxy assessment or calibration in modern settings (e.g., Genty et al., 2001; Mickler et al., 2004; Baldini, 2010; Mariethoz et al., 2012; Feng et al., 2012; Railsback, 2018). Monitoring of modern cave systems and their associated calcite growth records yields insight into speleothem growth dynamics and how hydroclimate parameters are transferred into the long-term physical and chemical record of speleothems. In the larger Southwest U.S. region (SW US hereafter; Table 1), speleothems also provide significant paleoclimate information not attainable by other means, particularly for the abrupt climate change events that characterized the

last deglacial (e.g., Wagner et al., 2010; Polyak et al., 2010; Feng et al., 2014b).

Here we consider the Late Pleistocene deglacial record preserved in a central Texas stalagmite (CWN-4) from Cave Without a Name (CWN) (Fig. 1A), focusing on the abrupt transition from Heinrich Stadial 1 (HS1) to the Bølling-Allerød interstadial period (BA) at ca. 14.7 ka. Warming associated with this transition is evident in Greenland ice cores (Rasmussen et al., 2014), where temperatures increased by 5–10 °C within decades (Kienast et al., 2003; Buizert et al., 2014), and this abrupt event is widely described as the Bølling Warming or Bølling Transition (Severinghaus and Brook, 1999). The transition from HS1 to the BA (HS1-BA transition hereafter) is also evident in marine records that preserve evidence of Meltwater Pulse 1a (MWP-1a), which contributed to 12–22 m of global sea level rise within a few hundred years (Gornitz, 2012; Deschamps et al., 2012). Temperature and precipitation changes in both hemispheres related to latitudinal heat distribution and intensity of ocean circulation are well documented (e.g., Severinghaus and Brook, 1999; Liu et al., 2009; Otto-Bliesner and Brady, 2010; Markel et al., 2016). These combined phenomena portray the HS1-BA transition as Earth's most extreme natural warming event over the past 25 k.y. (Kienast et al., 2003). Yet, summaries of North American climate change during the last deglacial are dominated by records west and east of Texas (e.g., Clark et al., 2012). There are relatively few comparable climate records in the SW US in general and in Texas in particular to determine how the climate system in this region responded to such abrupt global events (Feng et al., 2014b; Oster and Kelley, 2016).

Slow growth rates pose challenges for high-resolution speleothem paleoclimate research in semi-arid regions. Growth rates in central Texas stalagmites are on the order of 10s of $\mu\text{m}/\text{yr}$ (Musgrove et al., 2001), condensing decadal to millennial climate shifts into short stratigraphic intervals. Obtaining high-temporal

Table 1

Acronyms and abbreviations used in this paper

Common Usage	
AMOC	Atlantic Meridional Overturning Circulation
BA	Bølling-Allerød
CLFM	confocal laser fluorescence microscopy
GoM	Gulf of Mexico
HS1	Heinrich Stadial 1
HS1-BA transition	transition from Heinrich Stadial 1 to the Bølling warming interval
IRMS	(gas source) isotope ratio mass spectrometry
ITCZ	Intertropical Convergence Zone
LGM	Last Glacial Maximum
LIS	Laurentide Ice Sheet
LLJ	low level jet
MW	meltwater
MWF	meltwater flood
MWF-3	most intense LIS meltwater flood event in GoM, involving hyper- and hypo-pycnal flows
MWP-1a	Meltwater Pulse 1a
NASH	North Atlantic Subtropical High-pressure cell
NAWP	North Atlantic Warm Pool
SIMS	Secondary ion mass spectrometry
SST	sea surface temperature
SW US	southwest U.S. region
WNA	western North America
YD	Younger Dryas
Archive-specific	
BD	Brain Dead monitoring site in CWN
CWN	Cave Without a Name
CWN-4	study stalagmite
F200	200 μm micromill-step IRMS transect of Feng et al., 2014b
HBO	negative $\delta^{18}\text{O}$ excursion occurring in CWN-4 at the HS1-BA transition
HOW	Hole of Wisdom monitoring site in CWN
M50	50 μm micromill-step IRMS transect in this study
MH	murky horizon
SIMS chip	rhombohedral sample used for petrography and SIMS

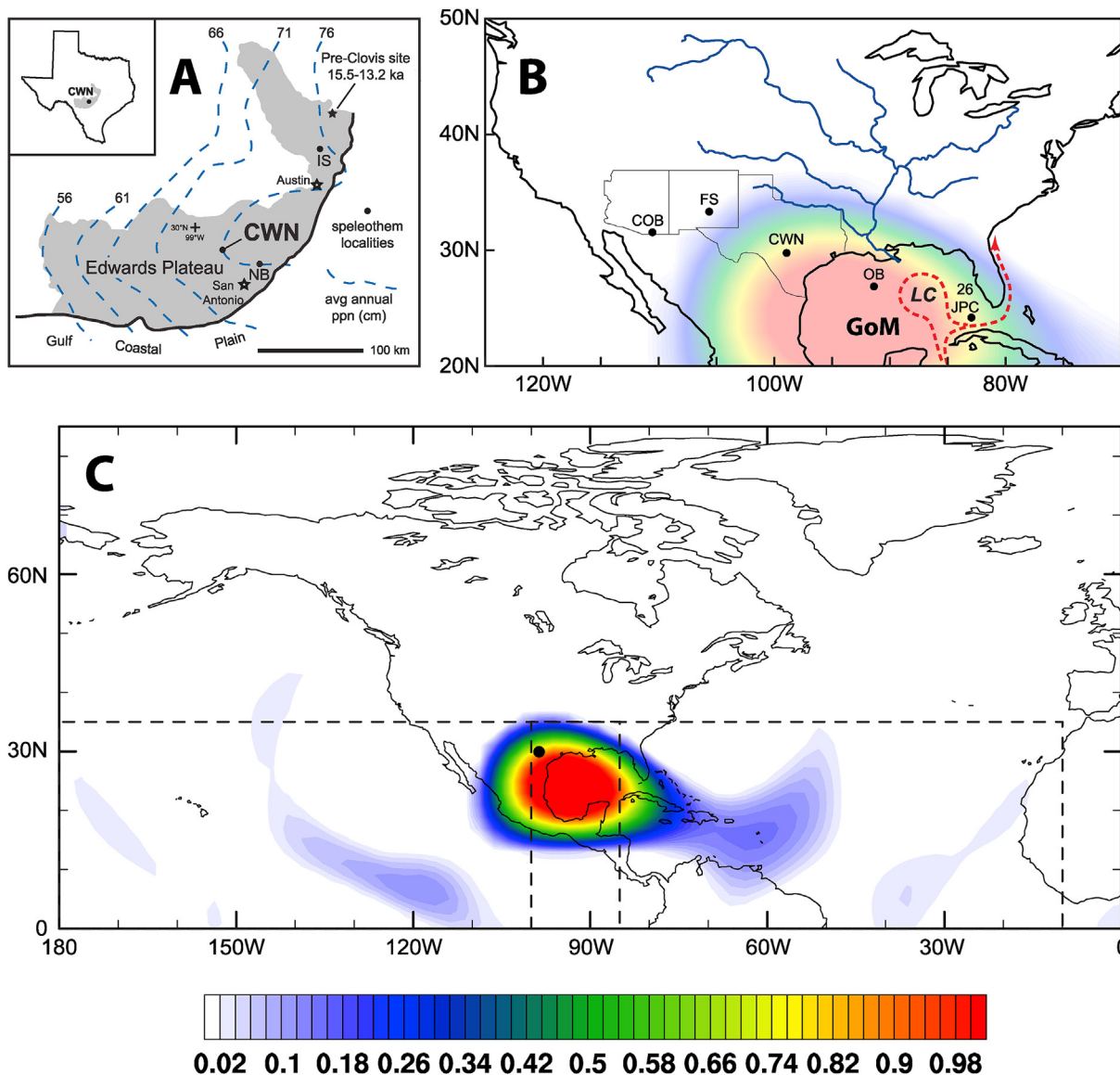


Fig. 1. A. Location map of Cave Without a Name (CWN) and other monitored caves (IS = Inner Space Cavern, NB = Natural Bridge Caverns) within the Edwards Plateau karst system of central Texas (left), showing regional precipitation gradient (after Musgrove et al., 2001). CWN is a tourist cave (29° 53' 10" N, 98° 37' 0" W) containing speleothems as old as ~40 ka. The cave is 15–30 m deep and extends laterally for more than 4 km. Pre-Clovis early Americans inhabited the region during the HS1-BA transition (Waters et al., 2011; but see Morrow et al., 2012). B. Regional map showing position of CWN, greater Mississippi River drainage system, and important $\delta^{18}\text{O}$ chronostratigraphy localities discussed: COB = Cave of the Bells, AZ; FS = Fort Stanton, NM; OB = Orca Basin, NW GoM; 26 JPC = Florida Strait. North Atlantic thermohaline circulation involves surface flow through the Gulf of Mexico via the dynamic (eddy shedding) Loop Current (LC). The LC also acts to limit riverine input, mainly from the Mississippi River, to northern and western portions of the GoM. Color moisture source contours muted from C below. C. Moisture source fraction (color contours) per grid box that contribute to annual average precipitation at the CWN proxy site (black dot) as simulated by global water tracer output from the GISS ModelE2.1 (Nusbaumer et al., 2019). Moisture sourced from dashed boxes comprise 96% of total precipitation, with 4% coming from other areas. The middle box, representing the GoM, local land recycling, parts of Mexico and Central America, and a section of the Tropical Pacific, is the largest source region and accounts for 51% of proxy site precipitation. Experiments removing the Tropical Pacific section (not shown) only modified the source fraction by ~1%, indicating that almost 50% of CWN precipitation comes from the GoM and surrounding land regions. The (sub-) Tropical Atlantic and (sub-) Tropical Pacific are next largest moisture sources, respectively contributing 23% and 21% of annual precipitation to CWN. (For interpretation of the references to color in this figure legend, the reader is referred to the Web version of this article.)

resolution isotopic and petrographic information thus requires high-spatial resolution sampling and imaging. In the case of CWN-4, the HS1-BA transition occurs within 8 mm. This interval is accompanied by a rapid negative $\delta^{18}\text{O}$ excursion (HBO hereafter), attributed to a change in Gulf of Mexico (GoM) $\delta^{18}\text{O}$ between HS1 and the BA, resulting from meltwater (MW) input from the Laurentide Ice Sheet (LIS). High resolution proxies of this input may yield insight to implications of rapid warming events (e.g., Oster and Kelley, 2016; Oster et al., 2019; Aharon, 2003, 2006; Ivanovic et al., 2016, 2017; Lin et al., 2021). For example, how much time

was required for the transition? Was the transition smooth and continuous or punctuated? How did regional hydroclimate change over the transition? Although we focus on the marked increase in growth rate across the HS1-BA transition (Fig. 2, red arrow 3), the deglacial in CWN-4 appears to have involved at least two prior and one later transition to fast growth rates (Fig. 2, red arrows 1–2, 4). Thus, it is of interest to understand whether these growth rate variations were also linked to changing deglacial hydroclimate.

Studies of CWN-4 demonstrate the regional influence of GoM-sourced moisture in the SW US during the last deglacial and

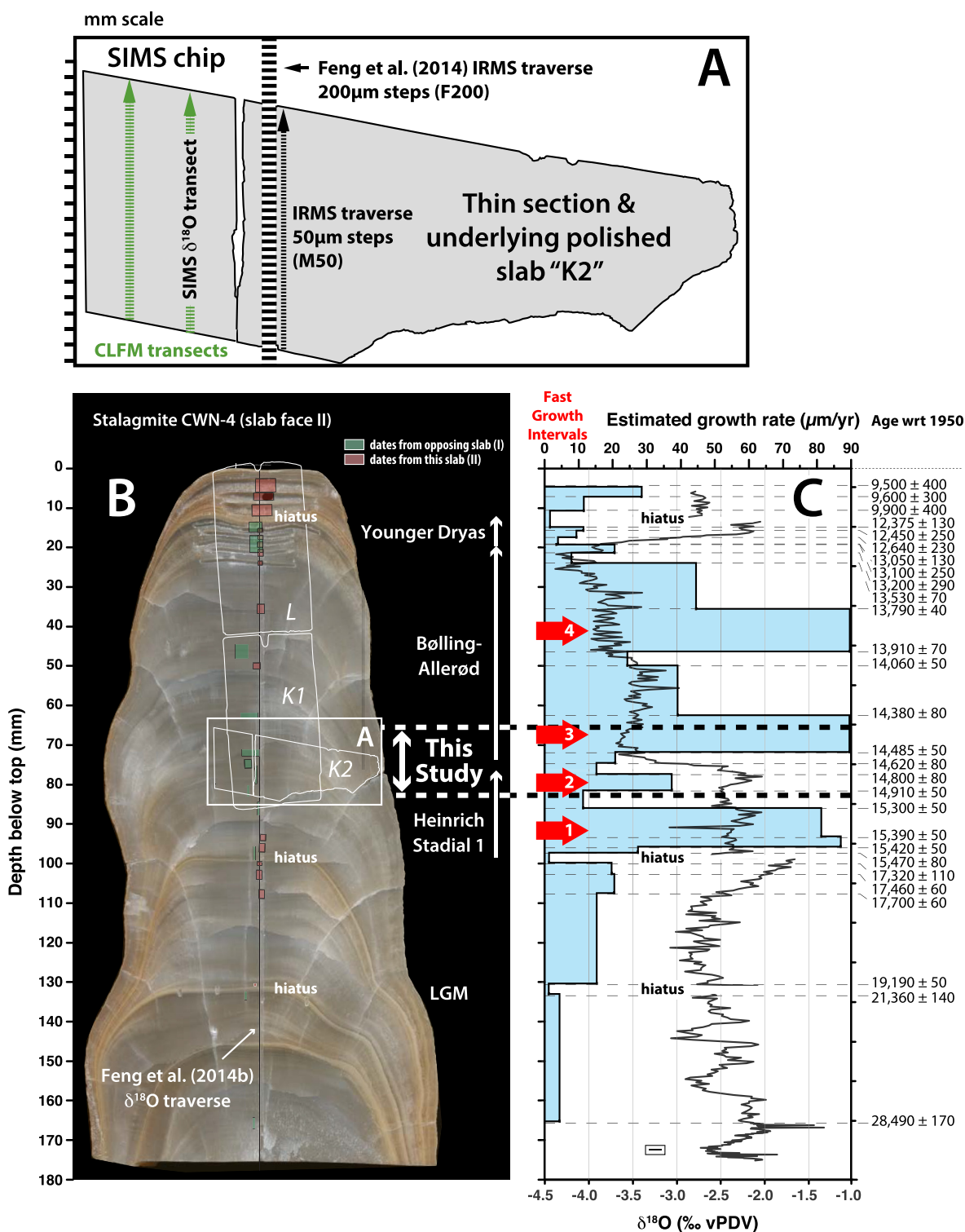


Fig. 2. Temporal and spatial context of deglacial growth rate and $\delta^{18}\text{O}$ variations over the HS1-BA transition study interval. **A.** Schematic illustration of sub-samples (SIMS chip, Slab/Thin Section K2) from B below (inset A), showing positions of high-spatial resolution transects used for CLFM imaging and SIMS and IRMS $\delta^{18}\text{O}$ sampling. **B.** Color image of CWN-4 slab face II showing positions of thin sections and sub-samples used in this study, the axial micromill 200 μm step sampling transect of Feng et al. (2014b) to establish $\delta^{18}\text{O}$ stratigraphy, and previous U-series datums (pink boxes - this slab; green 2 boxes - opposite slab) and growth hiatuses. Thin section K2 was prepared 30 μm thick from the slab face shown, whereas thin sections K1 and L were prepared 150 μm thick from the opposing slab face. The lower portion of thin section K1 overlaps with the study interval and thin section K2. Thin section L includes the top of CWN-4 and has a higher detrital content that is associated with hiatuses. **C.** Stratigraphic cross-plot of IRMS $\delta^{18}\text{O}$ (black curve) and growth rate variations (blue field), showing associated U-series age control; see Feng et al. (2014b, their Fig. 3) for corresponding $\delta^{13}\text{C}$ stratigraphy. The abrupt decline in $\delta^{18}\text{O}$ occurring between 76.4 mm and 72.7 mm below the top of CWN-4, termed the HBO, marks the central position of the HS1-BA transition study interval. Red numbered arrows show positions of fast growth rate intervals during the deglacial. Growth rates increase 4-6-fold across the HBO (red arrow #3). Error bar at bottom of figure (inside inset box) shows typical 2σ uncertainty of $\pm 0.08\text{‰}$ for IRMS $\delta^{18}\text{O}$ measurements. (For interpretation of the references to color in this figure legend, the reader is referred to the Web version of this article.)

conclude that 1) $\delta^{18}\text{O}$ variations mainly reflect MW input into and transport of moisture from GoM relative to Pacific sources, and 2) stalagmite growth rate variations reflect shifts between dry and wet conditions (Feng et al., 2014b). To advance our understanding of the driving mechanisms of hydroclimate change during the HS1-BA transition we present 1) multi-year physical and chemical monitoring of drip waters and cave atmosphere that are key to interpreting the CWN-4 archive; 2) petrographic and textural observations, including confocal laser fluorescence microscopy (CLFM) imagery, that elucidate the nature of growth increments; and 3) high-resolution $\delta^{18}\text{O}$ SIMS and IRMS data over the HS1-BA transition interval. These new contributions allow us to advance interpretations of the links between LIS MW flood occurrence in the GoM and contemporaneous $\delta^{18}\text{O}$ excursions in CWN-4. This unique approach provides evidence that delivery of GoM moisture to the central Texas region was suppressed during MWP-1a and then dramatically increased, and allows us to posit that deglacial hydroclimate in central Texas largely followed changes in North Atlantic climate that perturbed thermohaline circulation.

2. Hydrogeologic and hydroclimatic setting

2.1. Location and stalagmite CWN-4

CWN (Fig. 1A) developed within the lower Cretaceous Glen Rose Limestone associated with karstification of the Edwards Plateau. The cave has many active drips and a stream network and is part of the Trinity Aquifer system (Veni, 1994). We studied the upper 174 mm of the 500 mm-long stalagmite CWN-4 through slabs and thin sections to decipher development of growth fabrics (Fig. 2A). CWN-4 grew from approximately 38.5 to 9.5 ka (Musgrove et al., 2001; Feng et al., 2014b). The upper 174 mm grew from 29 ka to 9.5 ka, and contains the BA interval. CWN-4 consists of dense (sparitic) translucent grey calcite with faint sub-mm-scale growth layering, discernible as alternations of darker and lighter grey lamina. A prominent (palasidic) columnar calcite fabric, normal to growth layering, comprises varyingly reflective elongate “super-crystal” domains (Braithwaite, 1979). These domains radiate outward from the central growth axis. Several prominent orange-brown growth band intervals correspond to growth hiatuses at varying depths (Fig. 2B).

2.2. Present-day climate, seasonality and sources of moisture

Central Texas has a subtropical/sub-humid to semi-arid climate that is prone to droughts and floods, experiences strong seasonality in temperature (2.7–33.4 °C), and lacks a well-defined precipitation seasonality (Wong et al., 2015). The Southern Great Plains Low-Level Jet is a major transporter of spring and summer moisture from the GoM to the central U.S. (Uccellini and Johnson, 1979; Higgins et al., 1997). Mesoscale convective systems fed by this Low-Level Jet contribute 70% of warm season rainfall over the Great Plains (Fritsch et al., 1986; Feng et al., 2019). Tropical storms, originating mostly from the GoM and occasionally from the eastern tropical Pacific (Fig. 1B and C), can produce large rainfall in summer and early fall. Late fall and winter rainfall is typically driven by the Pacific winter storm track. The CWN region receives ~970 mm of annual rainfall with peaks during spring and late fall (US Climate Data, 2021). SW US drought mechanisms may be primarily driven by temperature or low rainfall (Weiss et al., 2012). The onset and persistence of drought in Texas are governed by a strong coupling between soil moisture and precipitation, with low antecedent soil moisture enhancing convective inhibition, making summer droughts more persistent (Koster et al., 2004; Myoung and Nielsen-Gammon, 2010).

2.3. Climate patterns of the LGM and deglacial period

Based on paleoclimate reconstructions, the SW US was wetter during the Late Pleistocene glacials and deglacials than the Holocene and present day (Musgrove et al., 2001; Toomey et al., 1993). Explanations for this marked difference in moisture distribution include a deeper penetration of tropical Pacific air to the continental U.S., shifts in latitude and strength of the polar jet, and shifts in atmospheric circulation due to the presence of the LIS (e.g., Oster and Kelley, 2016). Abrupt and large-magnitude climate change events during the deglacial, such as the BA warming and Younger Dryas (YD) cooling, are well documented in polar and equatorial regions, but lacking in many mid-latitude terrestrial environments. In Texas, multiple moisture proxy records indicate that this region was responsive to abrupt climate change events such as the YD cooling and early Holocene warming (Toomey et al., 1993; Holliday, 2000; Polyak et al., 2004; Ellwood and Gose, 2006; Feng et al., 2014b; Wong et al., 2015), and abrupt deglacial climate events are also recorded in GoM sediment cores (e.g., Aharon, 2003; Williams et al., 2012). These studies portray the potential for higher temporal resolution and advancing proxy interpretations. Such advancements may help address other key paleoclimate questions, such as the source(s) of MW pulses that drove deglacial sea level rise and how hydroclimate variations influenced the distributions of earliest Americans, such as pre-Clovis inhabitants in central Texas (Fig. 1A).

3. Methods

3.1. Cave monitoring, $\delta^{18}\text{O}$ analysis, age and digital reference model

Monitoring of diffuse flow drip sites (BD, Brain Dead; HOW, Hole of Wisdom) in CWN, linked to local weather records, provide a five year-record (2012–2017) with near-monthly resolution of environmental conditions within and above the cave, drip rates, drip water $\delta^{18}\text{O}$ variation and calcite accumulation on glass substrates. These findings, integrated with monitoring efforts from other central Texas caves, offer predictions for how cave atmospheric conditions along with the amount and source of recharging moisture should affect the growth and $\delta^{18}\text{O}$ calcite composition of associated stalagmites during growth. To document growth fabrics and associated $\delta^{18}\text{O}$ variations across the HS1-BA transition study interval in stalagmite CWN-4, we performed high resolution petrographic and $\delta^{18}\text{O}$ isotopic analysis. Isotopic analysis was by secondary ion mass spectrometry (SIMS hereafter) with 10 μm spots and gas source isotope ratio mass spectrometry (IRMS hereafter) of 50 μm micromill step samples, from polished sub-samples, located left and right of the $\delta^{18}\text{O}$ IRMS (200 μm micromill steps) traverse of Feng et al. (2014b) (Fig. 2A). We subsequently refer to these $\delta^{18}\text{O}$ isotopic transects, and their respective sampling resolutions, as SIMS, M50, and F200. The HS1-BA transition interval is recognized by a sharp -1.7‰ $\delta^{18}\text{O}$ excursion (M50 transect) centered ~75 mm below the top of CWN4 (Fig. 2B). The study samples, referred to as the SIMS chip, thin section K2, and slab K2, all span this stratigraphic interval (Fig. 2A, C) and can be correlated on the basis of common growth lamina and isotopic maxima/minima. The age model in Feng et al. (2014b) was modified to provide optimal age control over the study interval. Integration of identically scaled high resolution imagery of the CWN-4 slabs sampled for U-series dating and studied sub-samples provide a unified digital reference frame for precise positioning of age datums, isotopic traverse datums, and growth fabric imagery. Methodological descriptions of cave monitoring activities, stalagmite sampling and $\delta^{18}\text{O}$ analysis, and age model construction are further detailed in Section S1 of Appendix A – Supplementary Information; Tables S2–3 show key reference datums for correlating isotopic data

over the HS1-BA transition study interval.

3.2. Petrography

We applied standard petrographic techniques to thin section/slab K2 and the polished SIMS chip to examine CWN-4 growth band fabrics associated with the HS1-BA transition interval, and to identify optimal transects for SIMS and IRMS sampling (Fig. 2A). We also examined fabrics in thin sections K1-L (Fig. 2A), in order to compare the nature of growth band morphologies preserved in the CWN-4 growth record above the HS1-BA transition study interval (~14,500 to 9500 ka) with insights gained about modern speleothem growth from monitoring in CWN. Thin sections (K1-L) were prepared 150 μm thick. The lower portion of thin section K1 overlaps with the study interval (SIMS chip and thin section K2) and is thus particularly relevant. In order to better interpret growth lamina fabrics and their stratigraphic variation over the HS1-BA transition study interval, we compiled a high-resolution photo-mosaic of the SIMS chip (Section S1.2).

3.3. Confocal laser fluorescence microscopy (CLFM)

CLFM uses radiation to stimulate fluorescence in speleothem samples, which often reveals growth bands. CLFM imaging of fluorescent growth bands was performed in two growth axis-parallel transects of the SIMS chip (Fig. 2C) using a Leica TCS SP5 X confocal laser fluorescence microscope in the Imaging Core complex of the Dell Pediatric Research Institute (UT Austin). The right stratigraphic transect directly overlapped the SIMS $\delta^{18}\text{O}$ transect. The other transect was positioned 3 mm to the left. Due to the rhombohedral shape of the SIMS chip the base of the right transect records the lowest stratigraphic position, whereas the top of the left transect records the highest stratigraphic position. Both transects share a common stratigraphy over a distance of ~14.5 mm. Fluorescence was stimulated by radiation at 488 nm, using a tunable Ar laser source. After experimenting with bandwidth filters, fluorescent light collectively emitted between 495 and 669 nm was found to produce optimal images of growth bands. When converted to the green channel of RGB images, grayscale values appear as green fluorescent images. Images for each $775 \times 775 \mu\text{m}$ field of view (tile) were acquired using a 20x objective (with 0.7 numerical aperture) by rastering with a $2.039 \mu\text{m}$ voxel. Each transect involved the acquisition of 20 tiled images (with 10% overlay), a process that was repeated through 120 depth slices (corresponding to a maximum penetration depth of $244.69 \mu\text{m}$). Brightfield (all emission wavelengths) images were simultaneously acquired. Stitching of tiles to obtain composite transect slices was performed using open source software (xuvtools/xuv stitch). 2D flattening was performed using Imaris software, after selecting a subset of depth slices that provided optimal imagery of growth bands. Adobe Photoshop was used to linearly adjust brightness and contrast to best resolve growth laminae.

4. Results

4.1. Cave monitoring

Temporal variations in environmental conditions above and within CWN, as well as calcite monthly growth rates on glass plate substrates, over the monitoring interval of Mar 2012–June 2017 are shown in Fig. 3 and tabulated in the data supplement (Table S1).

Above-cave conditions: Maximum daily temperatures above the cave show clear seasonal variations (Fig. 3C; Sect. 2.2). Precipitation averaged 78 rainfall events and 879 mm per year (Fig. 3B). Drought conditions for the Edwards Plateau (Fig. 3A), as categorized by the

Palmer Drought Severity Index, were mainly moderate to severe drought through Fall 2014, then transitioned to moderately wet conditions through Fall 2016 before resuming a trend toward mild drought conditions by end 2017 (Water Data for Texas, 2021).

In-cave conditions: In-cave temperatures monitored at the two drip water sites (BD and HOW) fluctuate over a narrow range (avg: $20.1 \pm 1.6 \text{ }^\circ\text{C}$), with subtle seasonal maxima and minima that follow external temperature variations (Fig. 3C). Cave-air CO_2 levels exhibit strong seasonal contrasts with highest levels exceeding 20,000 ppm during warm months and lowest values (<1000 ppm) during cool months (Fig. 3C). Cave-air CO_2 levels gradually rise (April–May) following winter thermal minima (Dec–Jan), and decline rapidly with the arrival of consistent cold fronts in October. This seasonal CO_2 cycle is similar to those found in other central Texas caves (Banner et al., 2007; Cowan et al., 2013). Drip rates (Fig. 3B) at site BD are higher (avg: 0.14 ± 0.14 drops/sec) and more variable (range: 0.002 to 0.596 drops/sec) compared to site HOW (avg: 0.03 ± 0.01 drops/sec; range: 0.015 to 0.084 drops/sec). No correlation or lag period is evident between high-rainfall intervals/events and drip rate at either site (Fig. 3A and B). BD drip water $\delta^{18}\text{O}$ values ($n = 31$) range from -4.9 to -3.9‰ (avg: $4.5 \pm 0.2\text{‰}$) (Fig. 3B). These values are similar to the range of mean $\delta^{18}\text{O}$ values of -4.9 to -4.3 for drip water for three other central Texas caves over a ten-year interval (Pape et al., 2010). HOW drip water $\delta^{18}\text{O}$ values ($n = 22$) range higher than BD, from -4.7 to -1.6‰ (avg: $3.6 \pm 0.7\text{‰}$) SMOW (Fig. 3B). BD drip water δD compositions ($n = 16$, Table S2) range from -31.7 to -18.0‰ (avg: $25.4 \pm 3.1\text{‰}$). HOW drip water δD compositions ($n = 17$, Table S2) are systematically higher than BD, ranging from -25.9 to -9.8‰ (avg: $19.6 \pm 4.4\text{‰}$). Of the two drip sites, calcite precipitation only occurs at BD, and only during periods of low cave CO_2 concentrations (typically Oct–May; Fig. 3B vs 3C).

4.2. Age model and growth rate estimations

We advanced the age model of Feng et al. (2014b) by normalizing stratigraphic positions of U-series datums to a common reference slab face, as shown in Table S2. Relative to the Feng et al. model, this exercise results in absolute shifts among the 28 datums between 0.19 and 1.59 mm (avg: 0.57 ± 0.31 mm). The SIMS chip and thin section/slab K2 span a maximum stratigraphic thickness of 18.1 mm. Age control for this interval is provided by six ages spanning a stratigraphic thickness of 23.48 mm. The bracketing ages (referenced to 1950) constrain the HS1-BA transition study interval to be between $15,300 \pm 50$ and $14,380 \pm 80$ BP, and allow estimation of growth rates for key study intervals (Table S2, Study interval datums B–E). Over this bracketing interval, age datum shifts relative to Feng et al. range between 0.64 and 0.88 mm (avg: 0.79 ± 0.11 mm). These shifts slightly change the duration of datum intervals (calculated from average U-series age estimates) over a range between -3.6 and 25.3 years. Differences in average estimated growth rates between the respective age models are small, ranging from -1.2 to $2.1 \mu\text{m/yr}$. Uncertainties on the six U-series ages bracketing the HS1-BA transition study interval range from 50 to 80 years (avg: 67 ± 16 yrs). All of the ages are in stratigraphic order. Four of the ages fall within analytical uncertainty of each other, preventing calculation of maximum estimated growth rates. Average estimated growth rates over the HS1-BA transition study interval of the SIMS chip and adjacent thin section/slab K2 vary by a factor of nearly six, between 15.2 and $89.5 \mu\text{m/yr}$. Growth rates before the HBO average $37.4 \mu\text{m/yr}$ (Table S2, Interval B). Within the HBO, growth rates slow to 15.2 and $20.7 \mu\text{m/yr}$ (Table S2, Intervals C and D) then, above the HBO greatly increase to $89.5 \mu\text{m/yr}$ (Table S2, Interval E). Although the datum shifts and differences in growth rate estimates are relatively small compared with the Feng

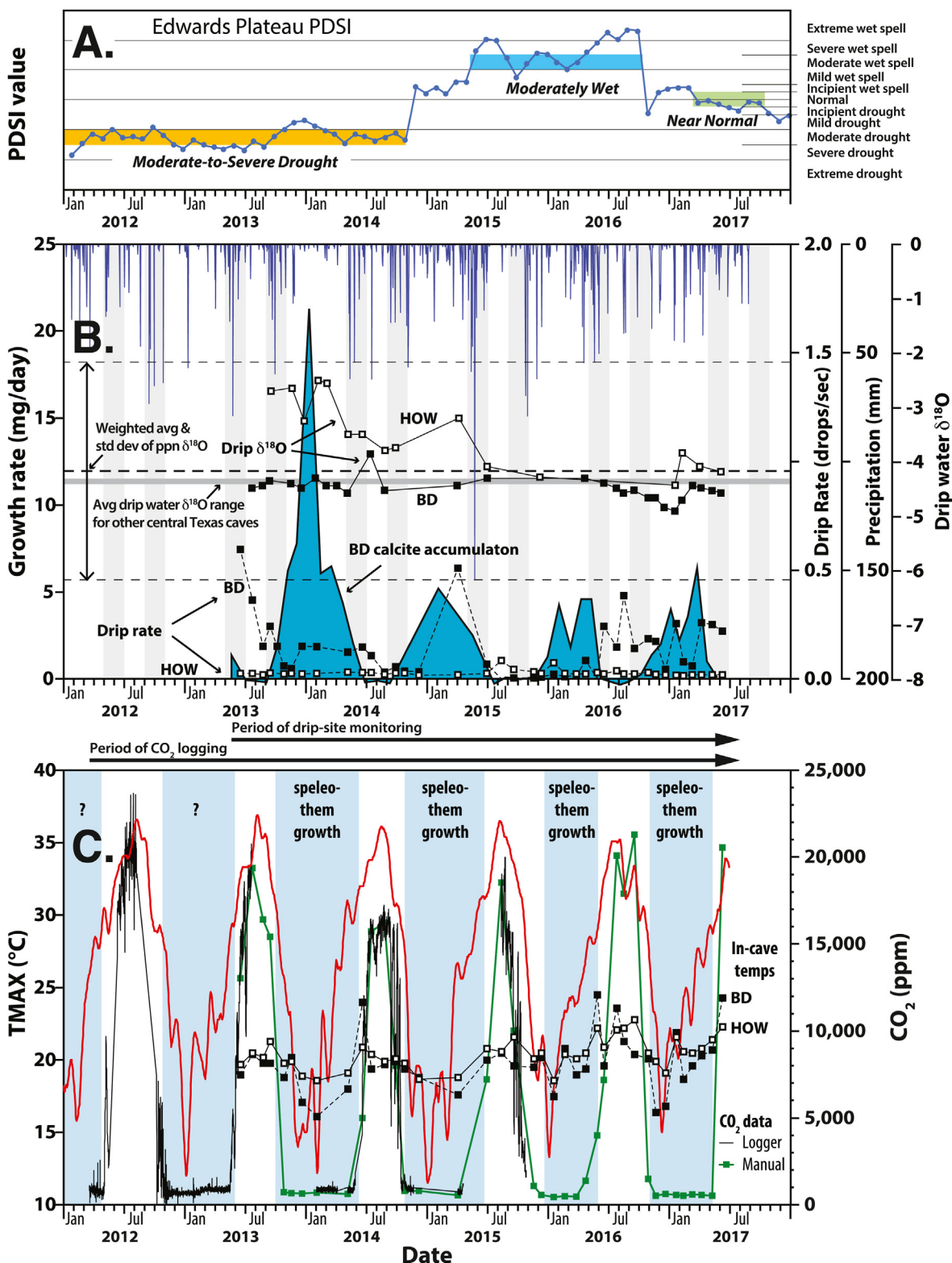


Fig. 3. 2012–2017 monitoring results for Cave Without a Name. **A.** Palmer Drought Severity Index (PDSI) for the Edwards Plateau climate region of Texas, showing varied drought conditions experienced over the monitoring interval. **B.** Drip $\delta^{18}O$ values (solid lines), drip rates (dashed lines) and associated plate calcite accumulation for Brain Dead (BD) and Hole of Wisdom (HOW) monitoring localities, relative to daily rainfall (blue “icicles”). Horizontal dashed lines show the estimated average (bold dash) and standard deviation (light dashes) $\delta^{18}O$ value for precipitation weighted for rainfall amount in the central Texas region for the period 1999–2007 (Pape et al., 2010); total $\delta^{18}O$ range for single rainfall events over this interval was -12.6 to -1.1 ‰. Horizontal grey band shows the range of average drip water $\delta^{18}O$ values in other central Texas caves. Drip rates at both localities are non-zero, but variable, with no obvious relationship to prior precipitation patterns. HOW consistently has slow drip rates with no annual accumulation of plate calcite (not plotted), whereas BD has slow to moderate drip rates and strong seasonal calcite growth during cool months (Oct–May). Minor negative values in plate calcite accumulation result from typical weighing uncertainties. **C.** Comparison of cave CO_2 levels and daily maximum temperatures (red curve). Cave CO_2 concentrations exhibit strong seasonal fluctuations, increasing from low levels (~ 1000 ppm) during cool season months to levels above 20,000 during warm season months. The rise in in-cave CO_2 levels lags seasonal temperature increases by

et al. age model, the revised age model more precisely constrains the chronostratigraphic framework of the HS1-BA transition interval in stalagmite CWN-4.

4.3. Microscopic characteristics of growth fabrics

4.3.1. Plane light petrography

Petrographic analysis of thin sections and the SIMS chip offer perspectives on growth fabric development, which facilitate an understanding of how growth layers are physically manifest. A key result is that growth layering is difficult (or impossible) to image in conventional thickness thin sections compared with thicker sections (Fig. 4 vs. 5–6). In sections cut parallel to the stalagmite's central growth axis, growth layering is recognized as alternations of inclusion-poor and inclusion-dense horizons. The inclusions are typically micron scale and too small to identify their content, but are interpreted as air or fluid-filled voids that may contain detrital impurities such as clay or organic matter. Only when a sufficient thickness of material is integrated (such as in transmitted light observation of thick sections or stacked and flattened CLFM images) is the composite inclusion density sufficient to visually define growth layers (Figs. 5–6). Inclusion-rich horizons in thickest sections (0.15–5 mm) viewed in transmitted light tend to be associated with darker (light grey-brown) calcite compared to underlying relatively inclusion-free horizons. Conventional 30 μm -thick thin sections (K2) are useful for resolving the scale of columnar calcite domains, but are too thin to consistently resolve inclusion-rich horizons (Fig. 4). Although inclusion horizons are more evident in 150 μm -thick thin sections (K1 & L), stratigraphically-continuous layer counting is impractical and restricted to intervals with higher detrital contents (Fig. 5). CLFM imagery of the 5 mm-thick SIMS chip, in particular, provided the clearest visualization of growth layers (Fig. 7).

Thin section K2 (30 μm -thick) demonstrates that coalesced columnar calcite, with negligible non-carbonate impurities, comprises the predominant fabric in the study interval (Fig. 4A–F). Individual columnar calcite crystals, best distinguished in cross-polarized light as domains of common crystallographic continuity and extinction parallel to the growth axis, may extend several mm in length, but eventually pinch out between bounding domains. Maximum widths of columnar domains near the central growth axis range from 92 to 272 μm (Fig. 4B–D). The columnar domains have length-to-width ratios >6:1 and display elongate columnar calcite fabric (Frisia and Borsato, 2010). Individual columnar calcite domains are composites of smaller sub-domains, as distinguished by slight differences in extinction direction (Fig. 4B–E). Evidence for possible growth layering in the 30 μm -thick thin section (K2), in the form of diffuse horizons of fine spindle-shaped inclusions, was only found in the upper study interval, above the HBO, associated with fastest estimated growth rates of $\sim 90 \mu\text{m}/\text{year}$ (Fig. 4G and H).

Thin section L (150 μm thick) offers valuable perspectives on growth fabric development. The top of this thin section preserves the final generation of CWN-4 calcite growth and demonstrates a complex surface topography consisting of vertically-elongate crystallites and their crystal terminations, in axial continuity with underlying crystallite generations (Fig. 5A and B). Scales and cross-sectional morphologies of crystallites are highly similar from layer to layer, but intercrystallite space decreases in underlying crystallite generations, apparently by lateral coalescence between growing crystallites (Fig. 5B). Growth during this upper interval

was associated with much higher levels of impurities (detrital OM and/or clay?) compared to the study interval, with abundant examples of brown-to-black detrital microlayers that thin above crystal terminations and pond between adjacent crystallites (Fig. 5C and D). Unpublished LA-ICP-MS spot analyses reveal elevated Al/Si in impurity-rich layers compared to impurity-poor layers, consistent with the presence of clay minerals. Concentrations of impurities are mainly apparent above coalesced crystallite growth layers as compared to within crystallite interiors, suggesting they accumulated when crystallite growth was minimal or that detrital input fluctuated during growth (Fig. 5D, F). The scale and cross-sectional morphologies of uncoalesced crystal terminations at the top of the section/stalagmite are similar to those for crystal terminations in less-detrital and more-coalesced intervals lower in the same thin section (Fig. 5E and F). Such detrital-poor intervals approach the comparatively impurity-free highly-coalesced growth fabrics comprising the HS1-BA transition study interval.

Alternating inclusion-poor and inclusion-rich couplet horizons are similarly detected in the stratigraphically lower thin section K1, which has a lower impurity content and more coalesced fabric than thin section L (Fig. 5G–J). That these features are visible in the lower part of the 150 μm -thick thin section K1, but are virtually undetectable in the same stratigraphic interval of the 30 μm -thick thin section K2 (cf. Fig. 4G and H), demonstrates the importance of thin section thickness for petrographic visualization of growth lamina. Furthermore, scales and morphologies of coalesced crystallite intervals in thin section K2, imaged petrographically, are comparable to those observed in stratigraphically equivalent portions of the adjacent SIMS chip imaged petrographically and by CLFM fluorescence imagery.

Fig. 6 shows the composite transmitted light image mosaic for the 5 mm-thick SIMS chip, with the corresponding CLFM image transects superimposed. Growth layers in the mosaic appear as alternating darker (grey-brown) inclusion-dense and lighter (white-tan) inclusion-sparse couplets, that can be traced laterally across the entire sample (including the CLFM image transects). The contrast between couplets ranges from sharp to faint, and can vary laterally and vertically. Growth layering is obscured in three mm-scale “murky” horizons (MH) in the lower half of the SIMS chip (labeled MH1-3 in Fig. 6). Thickest and most prominent growth layers characterize the upper half of the sample, above MH3 (Fig. 6A–C). U-series datums indicate a linear accumulation rate of 89.4 $\mu\text{m}/\text{year}$ for this interval, which is within the lower BA. Next thickest are growth layers below MH1, for which U-series ages indicate a linear accumulation rate of 37.4 $\mu\text{m}/\text{yr}$, which is within the upper HS1 (Fig. 6E). The intervening interval between MH1 and MH3 characterizes the HS1-BA transition and contains the thinnest growth layers, with U-series-based accumulation rates of 15.2–20.7 $\mu\text{m}/\text{yr}$. These layers are faint and difficult to trace laterally (Fig. 6D). Although the resolution of growth layers is substantially improved in the SIMS chip mosaic, contrasts between couplets are still too indistinct to be reliably counted throughout the entire study interval. Nevertheless, the vertical scale of layering can still be gauged over much of the SIMS chip and aspects of growth fabrics similar to those observed in thick sections K1 and L (Fig. 6A, cf. Fig. 5D, F) are also apparent in the SIMS chip mosaic.

4.3.2. CLFM imagery

Flattened composite CLFM images demonstrate that growth layers consist of dimmer and brighter fluorescent calcite couplets

several months, whereas cave ventilation to low CO_2 values closely corresponds with seasonal temperature decline. Integration of data demonstrates that drip sites with moderate drip rates only accumulate calcite during winter months associated with low in-cave CO_2 concentrations. (For interpretation of the references to color in this figure legend, the reader is referred to the Web version of this article.)

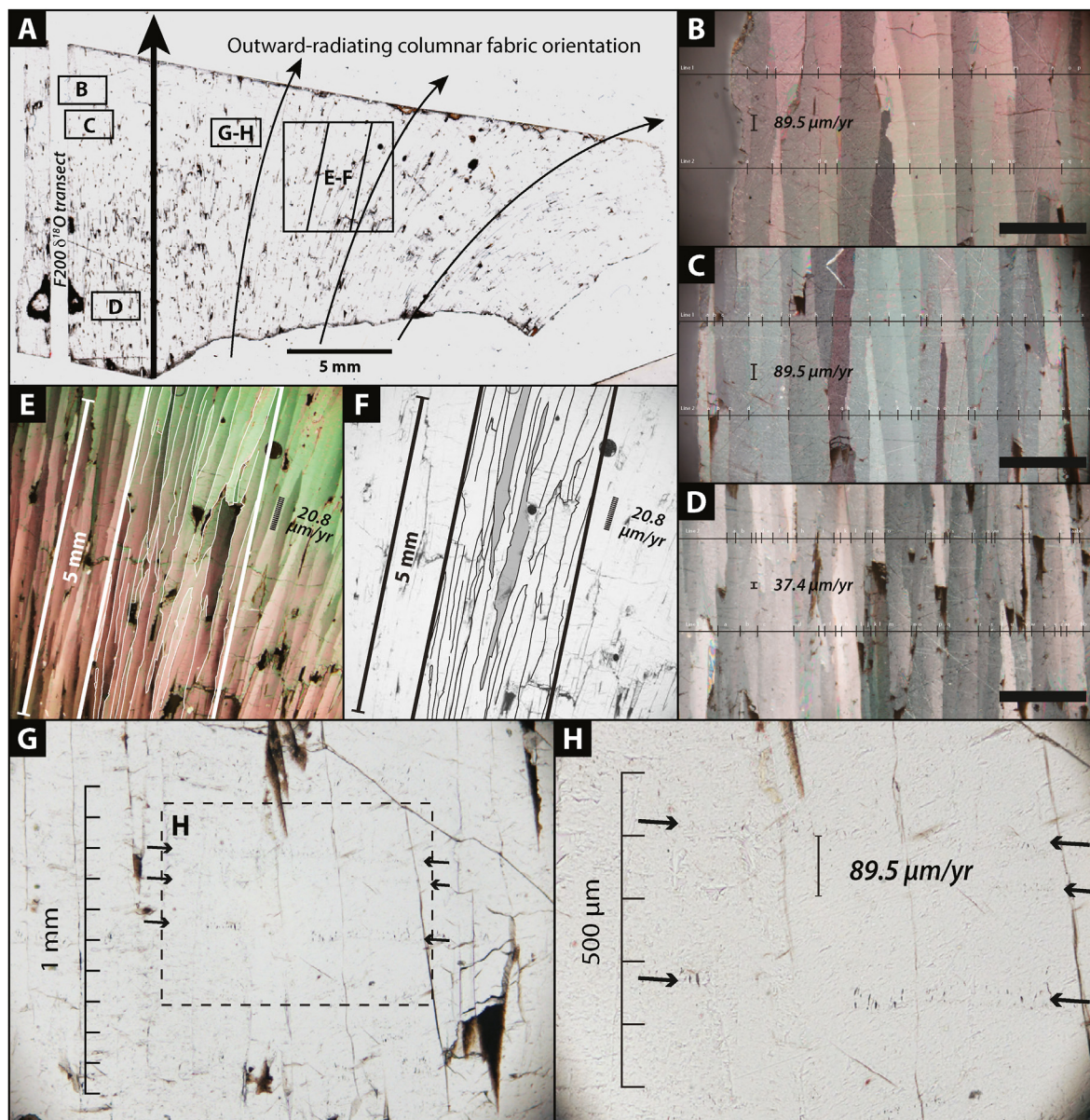


Fig. 4. Petrographic images of highly coalesced CWN-4 growth fabrics in thin section K2 (30 μm thick). For higher-resolution imagery, the reader is referred to the on-line version of the manuscript. **A.** Transmitted light overview of thin section K2 showing the location of the F200 micromill $\delta^{18}\text{O}$ transect (vertical gap running along the left edge) and inset locations of close-up images **B–H**. Sharp intercrystal boundaries and elongate pores reveal the outward-radiating orientation of columnar calcite fabric, subnormal to the stalagmite growth surface; left-to-right arrows show increasing lateral radiation away from the principal growth axis (bold arrow). **B–D.** Crossed polarized images of columnar calcite fabrics above (**B–C**) and below (**D**) the HBO negative $\delta^{18}\text{O}$ excursion interval. These intervals have fast growth rates of 89.5 $\mu\text{m}/\text{yr}$ and 37.4 $\mu\text{m}/\text{yr}$, respectively (black vertical bars), yet there is no obvious indication of growth layering. The pairs of horizontal thin black lines show locations where widths of columnar calcite domains were measured in each image; scale bars are 500 μm . **E–F.** Columnar calcite fabrics in cross-polarized (**E**) and transmitted light (**F**) within the HBO negative $\delta^{18}\text{O}$ excursion interval. Traced outlines of columnar domains over a portion of the images show that columnar (super) crystals can be several mm in length. However, the supercrystals are comprised of smaller vertically elongate subcrystals. This interval has slow growth rates of 20.8 $\mu\text{m}/\text{yr}$ (dash widths); like images **B–D**, there are no indications of horizontal growth layers. **G–H.** Close-up transmitted light images of the fast growth interval above the HBO negative $\delta^{18}\text{O}$ excursion, showing faint horizons of vertically oriented “spindle-shaped” inclusions (between black arrows). The spacing between the upper two inclusion horizons is reasonably close to the estimated growth rate for this interval from U-series age datums (black vertical bar in **H**). This was the only area of the thin section revealing evidence of horizontal layering. In stalagmites like CWN-4 with low impurity levels and highly coalesced growth fabrics, conventional 30 μm -thick thin sections are useful for petrographic imaging of columnar calcite fabrics, but offer only faint indications of horizontal growth layering.

(Fig. 7). The contrast between couplets ranges from abrupt to gradational (Fig. 7 A-A', D-D'), with brighter fluorescent couplets often being thinner and coincident with tops of crystallite growth fronts (e.g., Fig. 7 A-A', E-G). Couplet contrast is reduced to some extent by the depth integration of multiple CLFM images, which depending on the crystallographic relief of the growth front can act to broaden the apparent thickness of fluorescent couplets. Cross-sectional relief of growth layers ranges from relatively smooth

and undulating (e.g., Fig. 7 D-D') to higher relief chevron-shaped crystallites (e.g., Fig. 7 B-B'), the latter associated with growth of larger crystallites. Some sample intervals (Fig. 7E-G) display dull-fluorescent calcite separated by very narrow bright fluorescent layers. In the same field of view, the positions of crystallite terminations and inter-crystallite boundaries shift when viewed in progressively deeper depth slices - consistent with differing cross-sectional exposures of calcite polyhedra parallel to their growth

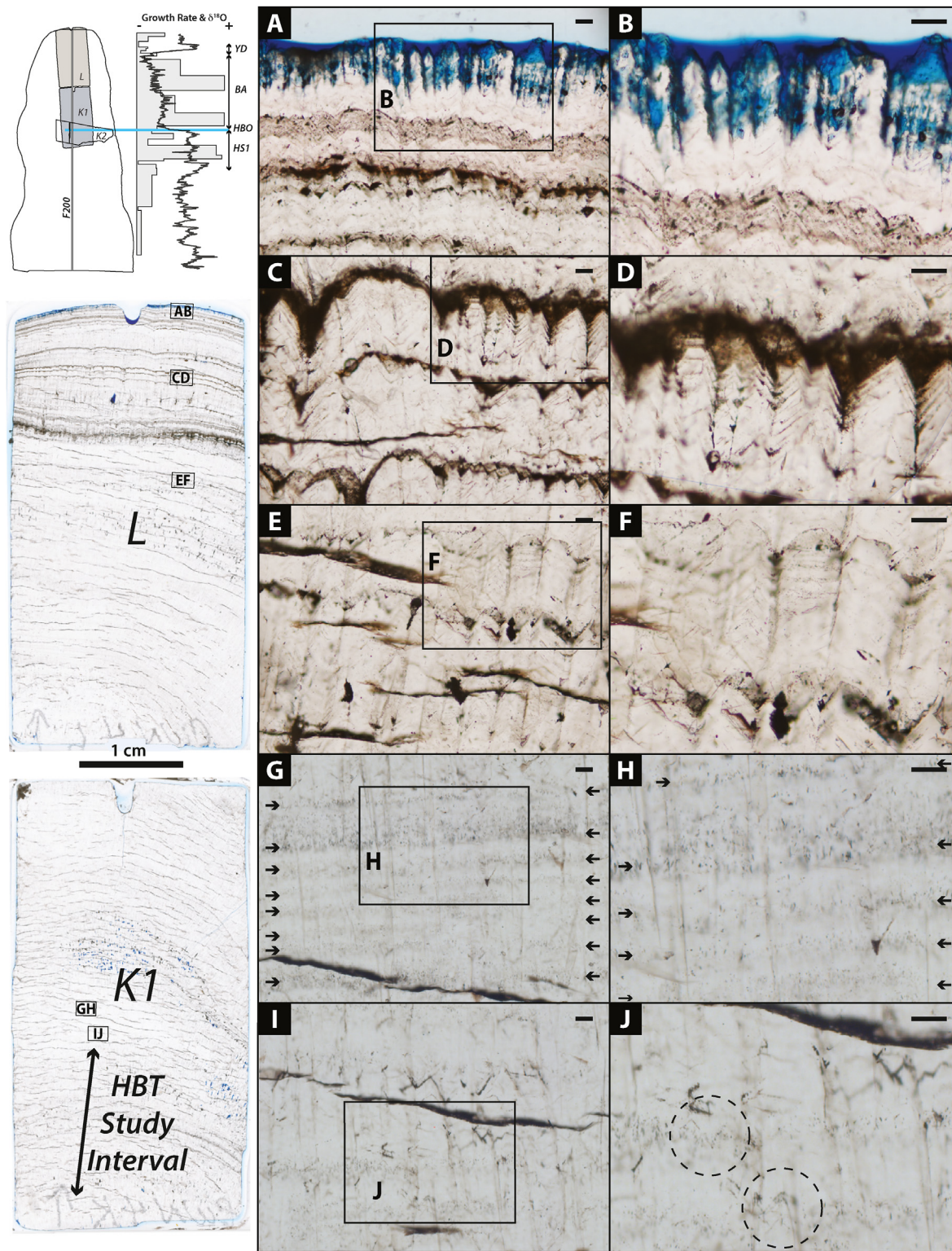


Fig. 5. Transmitted polarized light images of growth fabrics in 150 μm -thick sections L and K1, comprising the upper 85 mm of CWN-4. Upper left diagram shows stratigraphic positions of thin sections relative to the HS1-BA transition study interval. Labeled insets in whole thin section images show respective locations of images A-J. Scale bars in petrographic images A-J are 100 μm . Thin section L (images A-F) preserves the final generation of calcite growth at the top of CWN-4 and reveals the axial continuity and lateral coalescence of crystallite growth; blue epoxy reveals intercrystallite porosity (A-B). Intermittently higher levels of background detritus in this thin section reveal breaks in calcite growth, with detritus concentrating above polyhedral growth fronts, and with thick detrital-rich intervals corresponding with growth hiatuses (C-D). Ponding of detritus between adjacent crystallites (C-F) suggests that accumulation occurred while calcite growth was slow, or that detrital input was episodic. Layer truncation or microerosional surfaces consistent with Type E surfaces (Railsback et al., 2013) were not observed. Stratigraphic alternation of detrital poor and detrital rich zones reveals herringbone growth front patterns with tops and bottoms of "V's" respectively marking crystallite terminations and contact points between adjacent crystallites (D, F). Inter-crystallite contact points define vertical boundaries of columnar calcite domains that span many generations of calcite growth (B, D, F). Scales of herringbone growth fronts are similar to those frozen in time at the top of the stalagmite (cf. A-B). Thin section K1 (images G-J) overlaps with the HS1-BA transition study interval and has a less-detrital, more-coalesced, fabric compared to the upper

axes (Fig. 7E–G). This spatial amplification of fluorescence gained by stacking the 2D layers is key to seeing the fluorescent couplets.

When superimposed over the transmitted light photomosaic (Fig. 6), bright green fluorescent couplets consistently correspond to darker inclusion-rich intervals, whereas dimly fluorescent couplets correspond to more coalesced (inclusion-free) columnar calcite fabric. Couplets in some intervals can be traced laterally across the entire SIMS chip in both types of imagery (e.g., Fig. 7 A–A'). Consistent with observations from the transmitted light SIMS chip photomosaic, substantially thicker growth couplets occur in the upper half of the sample above MH3 (Fig. 7 A–A', B–B') and in the lower portion of the sample below MH1 (Fig. 7 D–D'). Couplet resolution is not apparent over portions of the intervening HS1–BA transition interval associated with slowest growth rates, particularly between MH1 and MH2. Over this interval, thin growth bands can only be resolved within select stratigraphic windows (Fig. 7 C–C'). High amplitude stacked crystallite “chevrons” occur in each of the murky horizons, possibly preserving high relief growth surfaces (Fig. 7, upper portion of C–C' spans the transition to MH3).

4.4. SIMS $\delta^{18}\text{O}$ results

SIMS $\delta^{18}\text{O}$ values, with sample datums adjusted to the digital reference model are shown in Fig. 8A and tabulated in Table S4. The SIMS $\delta^{18}\text{O}$ data range from -4.9 to -3.3‰ . Although the average 2SD precision obtained for the calcite reference standard (UWC-3) represents about 22% of the total range of measured $\delta^{18}\text{O}$, the major negative excursion associated with the Bølling transition is distinctive as a drop of 1.1‰ between 76.7 (-3.3‰) and 74.0 (-4.4‰) mm below the top of CWN-4 (Fig. 8A). The trend of decreasing $\delta^{18}\text{O}$ increases stratigraphically upwards, toward a nadir of -4.6‰ , but at a much-reduced rate. Despite the small analytical footprint of SIMS, resolution of any higher frequency structure in the stalagmite $\delta^{18}\text{O}$ trend is limited by the low precision obtained relative to IRMS.

4.5. IRMS $\delta^{18}\text{O}$ and $\delta^{13}\text{C}$ results

Datum-adjusted and age-calibrated IRMS stable isotope results for the F200 and M50 traverses are shown in Fig. 8B and C, and tabulated in Tables S5–6. In the longer F200 transect, the prominent Bølling negative $\delta^{18}\text{O}$ excursion spans a thickness of ~ 8.2 mm, beginning with highest values of $\sim -2.6\text{‰}$ at 78.083 mm and ending with values of $\sim -4.4\text{‰}$ at 69.883 mm below the top of CWN-4 ($\Delta^{18}\text{O}$ of -1.8‰ ; Fig. 2B). Within this span is a 3.4 mm-thick interval of particularly rapid decrease in $\delta^{18}\text{O}$ from values of -3.0‰ at 76.083 mm to -4.4 at 72.683 mm ($\Delta^{18}\text{O}$ of -1.4‰) (Fig. 8B). This initial portion of the negative $\delta^{18}\text{O}$ excursion featuring the highest stratigraphic rate of change defines the HBO event in this study (with $\Delta^{18}\text{O}$ of -1.7‰ in the M50 transect, discussed in Section 5.6). The corresponding interval of the $\delta^{13}\text{C}$ record (Fig. 8C) is an oscillating, higher frequency signal involving an overall decline to more negative $\delta^{13}\text{C}$ values (from -5 to -6.9‰), separated by an intermediate interval with more consistent values around -6.3‰ . The shorter but higher-sampling frequency (50 μm steps) M50 transect exhibits a similar range of $\delta^{13}\text{C}$ values that tracks well with the lower resolution F200 record, including prominent maxima and minima (red boxes in Fig. 8C) used to validate the respective

correlations of the isotope time series. The upper 1.2 mm of the M50 $\delta^{18}\text{O}$ record tracks within precision of the corresponding F200 $\delta^{18}\text{O}$ record, but is systematically offset to heavier compositions by $\sim 0.5\text{‰}$ (outside the precision of the measurements) in the lower portion of transect (Fig. 8B). The consistent $\delta^{13}\text{C}$ agreement between the two transects confirm the correlation between the records, suggesting that along-growth band $\delta^{18}\text{O}$ variations may differ by several tenths of a per mil over horizontal offsets of only a few mm (the maximum offset between the F200 and M50 traverses). Despite the $\delta^{18}\text{O}$ offset, the main features of the HBO excursion are consistent in terms of slopes and local inflections. The HBO $\delta^{18}\text{O}$ excursion (Fig. 8) in both IRMS transects and the SIMS transect, appears to begin close to the basal $\delta^{13}\text{C}$ maxima (76.483 mm) and end at 72.725 mm below the top of CWN-4, shortly above the $\delta^{13}\text{C}$ minima (73.709 mm). Although $\delta^{18}\text{O}$ stratigraphic variation between the techniques is similar overall, the range of SIMS $\delta^{18}\text{O}$ data are compressed by ~ 0.88 relative to IRMS data, and the SIMS data are systematically lighter by $\sim 0.5\text{‰}$. A similar offset between SIMS and IRMS $\delta^{18}\text{O}$ data was reported for Holocene planktic foraminifera (Wycech et al., 2018).

5. Discussion

Based on our monitoring results, CWN-4 growth fabrics, and annual growth rates over the HS1–BA transition study interval, we infer that: 1) CWN-4 growth layers were primarily deposited during cool months, 2) the $\delta^{18}\text{O}$ composition of CWN-4 calcite reflects the oxygen isotopic composition of GoM surface waters, and 3) variations in CWN-4 growth rates mainly track the amount of effective moisture (rainfall minus evapotranspiration) transmitted to the unsaturated zone. We discuss here the basis for these proxy interpretations, then apply these as paleoproxies to the CWN-4 study interval to assess how central Texas water availability changed during the HS1–BA transition. After comparing the CWN-4 record to other well-resolved northern hemisphere deglacial records, we lastly assess possible influences of ocean-atmosphere teleconnections on deglacial hydroclimate in the circum-GoM region.

5.1. Controls on CWN drip water $\delta^{18}\text{O}$ values

Central Texas Moisture Source Variations. The strongest moisture source areas for continental precipitation are located in proximal ocean basins (van der Ent and Savenije, 2013). The GoM coastline (shelf break) lies within 260 km (360 km) of CWN. Geostrophic winds deliver GoM-sourced moisture to Texas as low level jets, especially when the GoM is warm in Spring/Summer. Next closest oceanic moisture sources are further removed by factors of 3 (Gulf of Baja, 1077 km), 4.3 (Caribbean Sea, 1577 km), and 4.6 (Atlantic Ocean, 1557 km; Pacific Ocean, 1660 km).

Forward particle-tracking models that constrain global oceanic moisture sources (van der Ent and Savenije, 2013), indicate the following sources contribute to annual rainfall in central Texas: (1) the GoM/Caribbean (49%); (3) tropical Pacific (23%), (3) tropical E Atlantic (20%); (4) NE Pacific (4%) and (5) NE Atlantic (3%). Recycled continental moisture also contributes to annual rainfall, at about 35% of the total of these five source regions (van der Ent et al., 2010; Dirmeyer and Brubaker, 2007; Gimeno et al., 2012). Adding

portion of thin section L above. Here the tops of relic growth fronts appear to be preserved as stratigraphic horizons of fine inclusions that alternate with more coalesced horizons (G–H). Image G demonstrates several inclusion-dense horizons with vertical spacing on the order of 100 μm (lateral arrows). This interpretation is supported by close lateral inspection of inclusion-dense horizons that occasionally reveals inclusions that define V-shaped tops and valleys between adjacent crystallites (I, dashed circles in J). More generally, inclusions defining visible horizons occur at different depths below the thin section surface but can be reasoned to correspond with gaps in coalescence (detrital-free inclusions) and/or detrital surface layers that formed above a stalled complex 3D polyhedral crystallite growth surface. (For interpretation of the references to color in this figure legend, the reader is referred to the Web version of this article.)

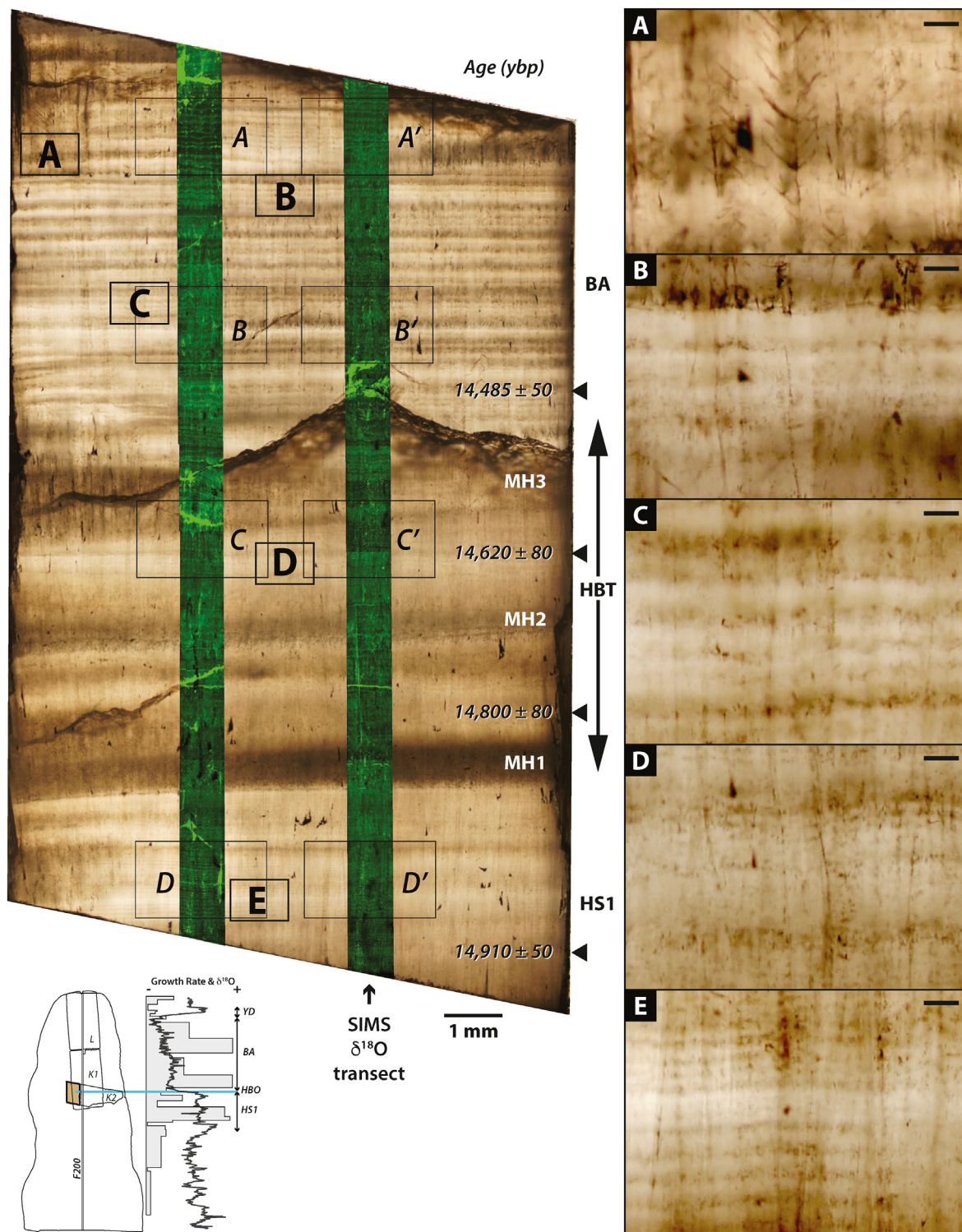


Fig. 6. Composite transmitted light image mosaic of the 5 mm-thick SIMS chip, with corresponding CLFM image transects (green) superimposed. U-series ages constraining growth rates are shown left of datums (black triangles). The SIMS $\delta^{18}\text{O}$ transect is centered within the right CLFM transect. Small black opaque areas correspond to surface pores where the gold coating required for SIMS analysis could not be removed. Insets A-E in the mosaic are enlarged in the right column images (scale bars are 100 μm for ease of comparison with Fig. 5 images). Insets A-A' through D-D' correspond to the CLFM image enlargements shown in Fig. 7. Stratigraphic variations in inclusion-dense and inclusion-sparse horizons reveal growth laminae that can be traced laterally across the entire sample. Significant variations in lamina thickness demonstrate significant changes in growth rate between moderate ($\sim 37.4 \mu\text{m/yr}$) rates during the final portion of HS1 (E), slow ($15\text{--}20 \mu\text{m/yr}$) rates during the HS1-BA transition (D), and substantially faster ($\sim 89.4 \mu\text{m/yr}$) rates during the initial BA (A-C). Resolution of growth lamina is substantially obscured in three murky horizons (MH1-3) in the lower half of the sample. Aspects of growth fabric observed in thick sections (Fig. 5, K1, L) such as columnar calcite domains (vertical traces evident in A-E) and herringbone growth fabric (image A) are similarly evident in the composite mosaic. (For interpretation of the references to color in this figure legend, the reader is referred to the Web version of this article.)

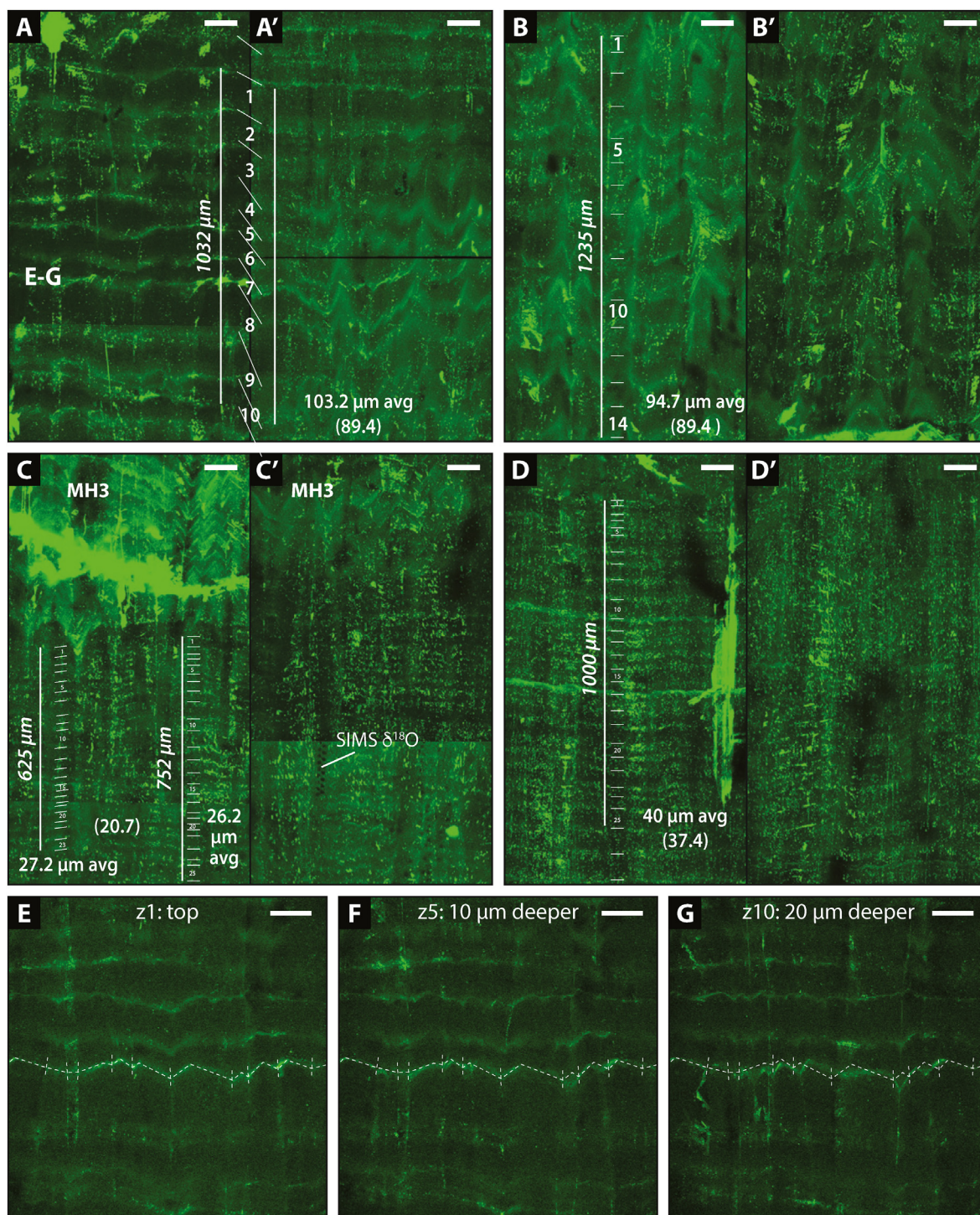


Fig. 7. CLFM composite images of growth fabrics over the study interval (refer to Fig. 6 insets for locations). Image pairs A-A', B-B', and C-C' are laterally superimposed from the left and right CLFM transects, respectively; individual SIMS δ¹⁸O sample pits can be seen in shallow flattened CLFM images (e.g., Image C'). Comparatively fluorescent and non-fluorescent laminae define horizontal growth layers, many of which can be traced laterally between left and right transects (e.g., white tie lines between brightly fluorescent bands in A-A'). Counting of fluorescence lamina in different portions of images provide estimates of average growth layer thickness (white μm labels). Brighter fluorescent bands correspond with outer surfaces of crystallites, which define nested herringbone overgrowth patterns within a broader columnar calcite fabric (e.g., image A-A', E-G). Fabric scale is similar to that observed petrographically in thin sections L and K1 (Fig. 5) and the SIMS chip (Fig. 6A); scale bars in all images are 100 μm for comparison. Sub-vertical patterns of fluorescence define faint boundaries between adjacent columnar calcite domains, which clearly span multiple growth layers (e.g., E-G). Other brightly fluorescent areas correspond with fractures (e.g., image C) and surface planes between columnar calcite domains when they are oriented parallel to the imaging plane (e.g., image D). Breaks in image contrast (e.g., image A', C') correspond to joins between different tiled and flattened images. Images A-A' and B-B', from the upper half of the SIMS chip above MH3, correspond to fast growth rates associated with onset of the Bølling warming interval. Average thicknesses of countable fluorescence couplets (103.2 and 94.7 μm) are reasonably close to the U-series interpolated growth rate of 89.4 μm/year. Images C-C', from between MH2 and MH3, correspond with slow growth rates during the HS1-BA transition. Average thicknesses of countable fluorescence couplets in three areas (26.2–28.2 μm/yr) correspond with 20.7 μm/yr for the U-series growth rate estimate. Images D-D', from below MH1, correspond to moderate growth rates at the end of HS1. An average thickness of 40.0 μm for countable fluorescence couplets closely compares to the U-series growth rate estimate of 37.4 μm/yr. Images E-G (from within Image A), show the same field of view for single voxel (z) layers at the surface (E), depths 10 μm (F) and 20 μm (G) deeper. The surface trace of a brightly

recycled moisture to the budget yields normalized source contributions of GoM/Caribbean (36%) > Recycled continental moisture (26%) > Tropical Pacific (17%) > Tropical E Atlantic (15%) > NE Pacific (4%) > NE Atlantic (2%). The predicted rainfall amounts from the moisture source regions in these models (van der Ent et al., 2010; van der Ent and Savenije, 2013) account for ~30–56% of annual rainfall amount in the CWN region, with model vs. annual rainfall difference likely attributable to model underestimation rather than omission of significant moisture sources.

General circulation models of atmospheric moisture flow over North America (Seager et al., 2018) provide further insight to temporal variations in central Texas moisture sources, notably that 1) lowest precipitation amounts (1.5–2.0 mm/day) occur during winter months (ONDJFM) in association with net NNE moisture transport; 2) highest precipitation amounts occur in spring (AMJ), 2.0–2.5 mm/day) and summer (JAS; 2.5–3.0 mm/day) months in association with net NNW moisture transport; and 3) annual moisture transport is predominantly N-trending. These results are consistent with particle back trajectory models indicating that air masses associated with summer and winter precipitation events in central Texas mainly have SE-NW and NW-SE trajectories, respectively (Feng et al., 2014b), and the year round prevalence of SE- and SSE-winds from the GoM (Gulf of Mexico Data Atlas, 2021).

These observations point to the predominance of precipitation derived from S- and SE-moisture sources, with the best-available estimates indicating that GoM/Caribbean moisture contributes about 50% of annual rainfall (direct and recycled) to central Texas, with tropical Pacific (17%) and tropical Atlantic (15%) of secondary importance. The annual persistence of diagnostic NNE- and NNW-trending moisture flow (Seager et al., 2018) demonstrates that GoM/Caribbean moisture is a year-around source, whereas lesser Pacific (and N Atlantic) sources contribute to annual rainfall mainly in winter months (Gimeno et al., 2012; van der Ent and Savenije, 2013; Wong et al., 2015). Although particle and moisture flow modeling does not parse GoM from Caribbean moisture amounts, the proximity and predominance of the GoM evapocenter, along with its associated SE- and SSE-winds, indicate it is strongly coupled with annual rainfall in central Texas.

Fig. 1B-C shows relative fractions of annual precipitation at CWN supplied from grid cell boxes (2.5x2, lat-lon) in three moisture source regions (sub-tropical Pacific, GoM, sub-tropical Atlantic) that account for 96% of annual precipitation, based on a modern climate simulation (global water tracer output from GISS ModelE2.1; Nusbaumer et al., 2019). This model demonstrates the strong predominance of GoM-sourced moisture for annual precipitation at CWN. Although monsoonal and tropical storm rainfall from any moisture source region can have very low $\delta^{18}\text{O}$ compositions (<10‰ VSMOW; Pape et al., 2010), modern GoM moisture has substantially higher $\delta^{18}\text{O}$ values (by ~10‰) compared to Pacific moisture (Feng et al., 2014b). Also shown in Fig. 1B are important deglacial $\delta^{18}\text{O}$ records in the Gulf of Mexico, New Mexico and Arizona, discussed later (Sections 5.7, S1.6), that also portray this relative GoM:Pacific influence.

During the last deglacial, the $\delta^{18}\text{O}$ composition of Mississippi River discharge was significantly lower (e.g., -38‰ to -11‰ VSMOW) than GoM seawater (~1‰ VSMOW). This was due to contributions from Laurentide Ice Sheet meltwater (LIS MW), particularly in the northern and western GoM, where modern riverine inputs concentrate due to westward longshore currents and diminished influence of the Loop Current (Oglesby et al., 1989; Vetter et al., 2017; Williams et al., 2012; Aharon 2003, 2006). GoM

moisture advected to central Texas should thus have proxied the influence of LIS MW input as negative $\delta^{18}\text{O}$ excursions (Feng et al., 2014b). Because the temperature-dependent oxygen isotope fractionation between GoM surface water and moisture during evaporation increases with lower temperature, GoM SST cooling would cause a negative $\delta^{18}\text{O}$ imprint, independent from meltwater input. To evaluate the potential impact of surface water cooling (alone) on the HBO, we assessed the change in $\delta^{18}\text{O}$ of speleothem calcite resulting from deglacial SST reduction across contrasting time intervals (Section S1.6). Our analysis, based on reported deglacial SST variations in the GoM (2–6 °C), indicates that moderate surface water cooling could account for no more than 30% of the -1.7‰ HBO excursion, and thus an additional source of isotopically depleted $\delta^{18}\text{O}$, such as meltwater input, is required.

Central Texas Precipitation $\delta^{18}\text{O}$ Variability. We compare the $\delta^{18}\text{O}$ variability of CWN drip waters to that of Austin precipitation, as Austin is ~95 km from CWN and has comparable annual precipitation amounts and average temperatures. $\delta^{18}\text{O}$ (VSMOW) of Austin precipitation, measured monthly to bimonthly over the period 1999–2007, had a range of -12.6 to -1.1 and a mean value of $-3.8 \pm 1.8\text{‰}$ (1σ), with a poor relation to seasonal temperature variations (Pape et al., 2010). Event-based sampling over the period 2015–2017 yielded a similar mean value of $-3.9 \pm 3.3\text{‰}$ (Sun et al., 2019). When weighted for rainfall amount, the average $\delta^{18}\text{O}$ of Austin monthly to bimonthly precipitation was $-4.1 \pm 1.8\text{‰}$ (Pape et al., 2010). Tropical storm systems from either the GoM or the Pacific Ocean occasionally bring rainfall with much lower $\delta^{18}\text{O}$ (~-13‰) to the region (Pape et al., 2010, Sun et al., in review).

Central Texas Drip Water $\delta^{18}\text{O}$ Variability. Drip waters in many central Texas caves exhibit a similar range of relatively constant $\delta^{18}\text{O}$ and δD values through time (Fig. 3B, grey horizontal band), and plot close to or slightly below the local meteoric water line (Guilfoyle, 2006; Pape et al., 2010; Feng et al., 2012, 2014b; Carlson et al., 2018). This stability has been demonstrated for drip sites characterized by both conduit and diffuse flow (e.g., Guilfoyle, 2006; Bunnell, 2019), demonstrating that infiltrating meteoric water is well-mixed with residence times long enough to dampen the larger variations observed among annual rainfall events in the region. Regional residence times therefore are likely to be at least interannual. Mean $\delta^{18}\text{O}$ values for central Texas drip sites commonly show an offset to lower values than mean weighted rainfall $\delta^{18}\text{O}$, consistent with a seasonal bias toward rainfall received during recharge periods (Pape et al., 2010; Bunnell, 2019; Baker et al., 2019; Hu et al., 2021).

CWN Drip Water $\delta^{18}\text{O}$ Variability. Average $\delta^{18}\text{O}$ and δD compositions of drip water at the slower HOW drip site are higher and more variable ($\delta^{18}\text{O} = -3.41 \pm 0.75\text{‰}$; $\delta\text{D} = -19.6 \pm 4.4$) than those at the faster BD drip site ($\delta^{18}\text{O} = -4.4 \pm 0.18\text{‰}$; $\delta\text{D} = -24.4 \pm 5.3\text{‰}$). BD average $\delta^{18}\text{O}$ and δD values plot on the local meteoric water line of Pape et al. (2010), consistent with precipitation above CWN being sourced from moisture masses comparable to those in the Austin area and with HOW drip water being affected more by evaporation (Fig. 3B). The BD drip water $\delta^{18}\text{O}$ average is identical to those from other central Texas caves within 100 km of Austin (Fig. 3B; $-4.3 \pm 0.4\text{‰}$ for Cave NB, $-4.4 \pm 0.2\text{‰}$ for Cave IS; $-4.4 \pm 0.2\text{‰}$ for Cave WC; Pape et al., 2010; Carlson et al., 2018). This indicates that central Texas drip waters reflect a regional meteoric water $\delta^{18}\text{O}$ signal (Pape et al., 2010; Feng et al., 2012, 2014b; Carlson et al., 2018; Hu et al., 2021). The consistency of $\delta^{18}\text{O}$ of the faster dripping and actively growing BD monitoring site, along with lack of drip rate response to preceding rainfall events,

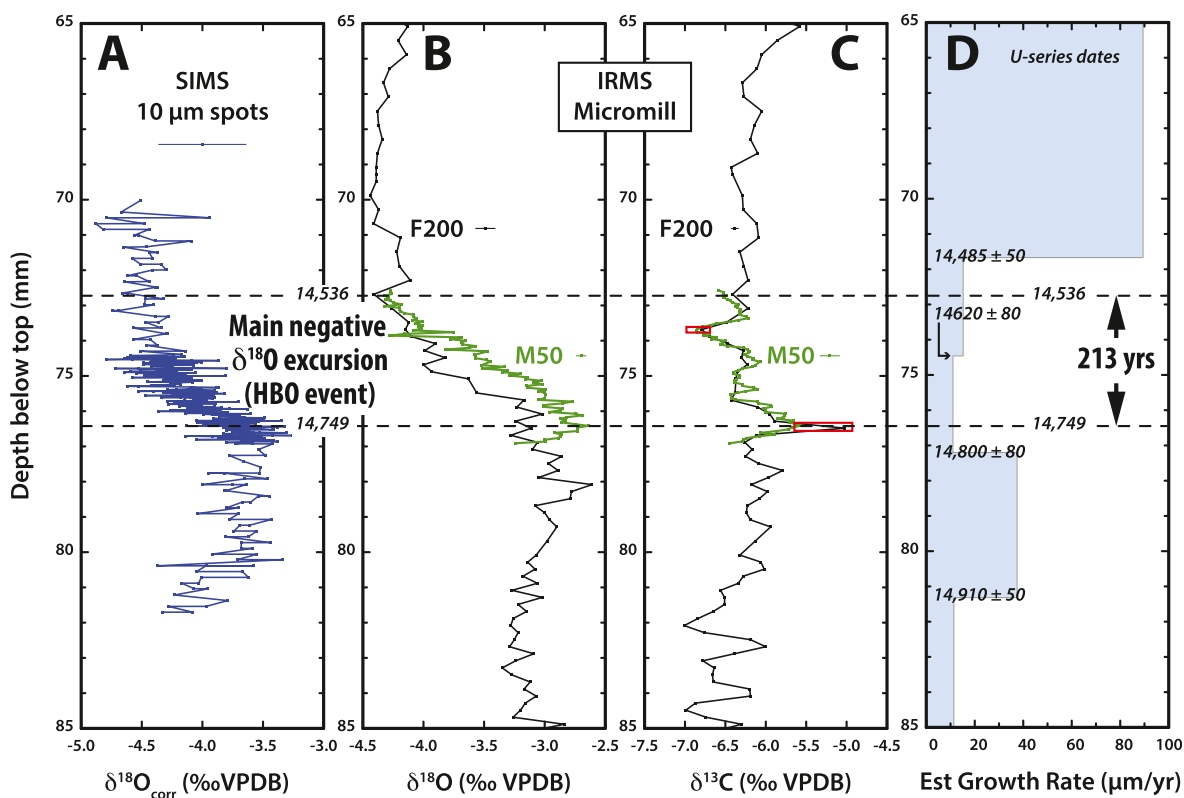


Fig. 8. Stable isotope results for the Bølling transition study interval in CWN-4. **A.** SIMS $\delta^{18}\text{O}$ results ($n = 384$). **B–C.** IRMS $\delta^{18}\text{O}$ and $\delta^{13}\text{C}$ transect results for continuous micromill sampling. The F200 transect corresponds to 200 μm sampling steps in Feng et al. (2014b). The M50 transect (this study) was sampled in continuous 50 μm steps ($n = 89$). Red boxes in C outline corresponding $\delta^{13}\text{C}$ minima and maxima used to correlate F200 with the M50 transect. Horizontal error bars in A–C show corresponding 2-sigma precisions obtained for standard replicates (Section 3.4 and 3.5). **D.** Growth rate estimates determined from U-series ages. The main negative $\delta^{18}\text{O}$ excursion marking the transition 6 from Heinrich Stadial 1 to the Bølling-Allerød (the HBO event) corresponds with an interval of slow growth rates. Linear extrapolation from U-series ages indicate the HBO event spans a 213-year interval, from $14,749 \pm 80$ to $14,536 \pm 80$ years before present. (For interpretation of the references to color in this figure legend, the reader is referred to the Web version of this article.)

indicates a well-mixed meteoric water source in the epikarst. Similarly, drip rates at different diffuse CWN drip sites waned but did not stop during an historic drought (Schwartz et al., 2013). Precipitation infiltrating beyond the reach of evapotranspiration (1–2 m) is therefore likely to contribute to a well-mixed regional reservoir dominated by matrix and fracture porosity with multiyear residence times (Schwartz et al., 2013). Monitoring and proxy system model studies across central Texas indicate that drip sites most commonly reflect long-term recharge $\delta^{18}\text{O}$ values and rarely reflect intra-annual hydroclimate events, including droughts and floods (Hu et al., 2021; Bunnell, 2019). Because the GoM is a consistent principal source of moisture for precipitation in central Texas (Bomar, 1995; Slade and Patton, 2003; Wong et al., 2015), its weighted average recharge $\delta^{18}\text{O}$ should mainly follow the composition of GoM vapor masses reaching central Texas. Regional atmospheric temperature changes could be responsible for some of the deglacial $\delta^{18}\text{O}$ variation in the CWN-4 records, but we note that the 1.7‰ decrease associated with the HS1-BA transition would require a 9.5 °C temperature increase based on the temperature-dependent fractionation relationship between water and calcite (-0.177‰ C^{-1} ; Tremaine et al., 2011). Given that subtropical/tropical western Atlantic SST changes across Heinrich stadials are estimated to have been 3–5 °C (Arienzo et al., 2015), the HBO is far outside being controlled by temperature alone. Past changes in convective vs. stratiform rainfall in mesoscale convective systems cannot be excluded as a contributor to past rainfall $\delta^{18}\text{O}$ variability in the region (Sun et al., 2019; Maupin et al., 2021). The correspondence between GoM surface water and CWN-4 $\delta^{18}\text{O}$ changes,

in both timing and magnitude (Figs. 10–11; Feng et al., 2014b) is, however, consistent with GoM surface water evolution as a dominant control on CWN dripwater decadal-to millennial-scale $\delta^{18}\text{O}$ variations during the deglacial. Based on this, the multiyear residence times, and consistent region-wide drip water $\delta^{18}\text{O}$ signals, we interpret decadal-to millennial-scale changes in stalagmite CWN-4 in the context of changing $\delta^{18}\text{O}$ of GoM surface waters.

5.2. Controls of CWN calcite growth based on monitoring

Integration of monitoring results over the five-year interval at CWN and over 5–20 year intervals at other caves in the region indicates that drip rate and ventilation-controlled cave-air CO_2 levels are primary controls regulating CWN calcite growth (Banner et al., 2007; James et al., 2015; Casteel and Banner, 2015). Mean drip rate for the BD site is five times faster than the HOW site. Although drip rates are continuous throughout the year at both sites, calcite precipitation on glass plate substrates only occurs at the faster drip site and only during seasonally cooler months, associated with low cave-air CO_2 levels driven by cave ventilation (Fig. 3B and C). The continuous CO_2 logging data yields perspective on the role and timing of cave-air CO_2 variations in regulating calcite accumulation. Transitions from high to low cave-air CO_2 concentrations that initiate cool-season calcite growth are relatively fast, within the period of monthly plate collection. Spring transitions to sustained high cave-air CO_2 concentrations are slower compared to fall transitions to sustained low CO_2 concentrations, consistent with the sawtooth nature of seasonal CO_2 shifts observed in this region

(Banner et al., 2007; Wong and Banner, 2010; Wong et al., 2011; Cowan et al., 2013). For example, the increase from CO₂ values less than 1000 ppm to sustained values greater than 13,000 ppm occurred within 40 days (5/23/14 to 7/3/14), whereas the subsequent drop from CO₂ values of 13,000 ppm to sustained values less than 1000 ppm occurred in less than a week (10/11/14 to 10/16/17). Although the monthly plate calcite collection rate cannot constrain the maximum CO₂ concentration under which calcite precipitates, all periods of active growth occurred during cool months (typically Oct–May) under relatively constant low CO₂ levels of <1000 ppm and within a narrow atmospheric temperature range (avg: 18.7 ± 0.5 °C). This is consistent with the delineation of CO₂ thresholds on calcite precipitation in central Texas caves by James et al. (2015).

5.3. Seasonality of CWN-4 growth fabrics

Based on the above monitoring results (Fig. 3B and C), annual growth fabrics for CWN stalagmites growing from diffuse flow drip sites like BD can be expected to consist of a series of fairly continuous cool-month growth intervals that are abruptly punctuated by warm-month hiatuses. More continuous annual calcite deposition might have occurred in the past if ventilated conditions were maintained over longer intervals (longer winters) and/or if transitions to low CO₂ conditions were more gradual (climate with reduced seasonal temperature gradient), but it is reasonable to expect that CWN-4 stalagmite growth fabrics should preserve strong seasonality. The physical expression of calcite growth fabrics over the HS1-BA transition interval, especially from inspection of thick sections and CLFM imagery of the SIMS chip, is consistent with this prediction (Figs. 5–7). We find that inclusion-rich horizons, with associated higher levels of impurities, closely correspond with tops of polyhedral calcite crystallites and associated intercrystallite porosity, whereas the immediately underlying intervals are more coalesced and inclusion-free. These alternating inclusion-rich and inclusion-poor growth layers accumulate over time in crystallographic continuity and form multi-millimeter long columnar calcite domains. This observation comports with the benchmark finding of Kendall and Broughton (1978) that columnar calcite fabrics in most speleothems develop progressively through the orderly stacking and lateral coalescence of polyhedral crystallites over many generations of syntaxial overgrowths. Based on estimated annual growth rates over the study interval (15–90 μm/yr) from U-series ages, such multi-millimeter-scale columnar domains must span decades to centuries of speleothem growth, whereas the finer-scale inclusion-rich and inclusion-poor growth layers correspond with annual couplets.

Hiatuses in stalagmite growth often correspond to impurity-rich layers or dissolution surfaces (Tan et al., 2006). We suggest that in CWN-4 growth layer couplets, the inclusion-rich lamina correspond to warm season growth hiatuses and the increased abundance of impurities is associated with stalled crystallite growth fronts. This reasoning follows from observations in the top portion of CWN-4, which 1) preserves the morphology of the final stalled growth front and the increased intercrystallite porosity at the top of the stalagmite (Fig. 5A and B), and 2) records an increased level of impurity input as detrital-rich layers of variable thicknesses, some of which thin over crystal terminations and pond in valleys between crystallites (Fig. 5C and D). Since U-series ages link thicker detrital microlayers to long-term hiatuses in CWN-4's growth history (Feng et al., 2014b), and impurities are mainly restricted to exposed upper growth surfaces of crystallites, we infer that the amount of impurities (i.e., thickness of an inclusion-rich layer) may scale with the amount of time that growth was stalled. These inclusion-rich layers thus bracket episodes of more continuous

calcite growth. Supporting this inference is CLFM imagery, which demonstrates that sites of brightest fluorescence occur as distinct stratigraphic horizons that closely correspond to the upper surfaces of polyhedral calcite crystals (Fig. 7E–G).

Organic compounds are widely considered to be the principal source of fluorescence in speleothems (Baker et al., 1993; Shopov et al., 1994; Ramseyer et al., 1997). These may take the form of fluorophores, possibly enriched in colloidal metals, adsorbed onto crystal faces, occupying inclusions or lattice defects. The distinct orange to brown colors associated with thicker impurity layers (e.g., Fig. 2B) is consistent with organic colloids. We note that closed fractures and edges of columnar calcite domains exposed in vertical pores are also characterized by bright fluorescent emission (Fig. 7C and D), presumably caused by light scattering associated with sharp edges. Smaller inclusions or pores associated growth layer fronts could thus potentially fluoresce for similar reasons not associated with organic detrital enrichment. Assuming detrital input is constant and sourced from drip water, evidence of ponding of detrital microlayers between adjacent crystallites (Fig. 5D–F) suggests that impurities tend to accumulate during warm season intervals when calcite growth stalls but drips remain active. By this reasoning, impurities are diluted during cool season calcite growth. Alternative explanations include 1) that drip waters have higher impurity contents during warm seasons; or 2) that impurities are substantially aeolian and either concentrate over stalled crystallite growth fronts during warm seasons or enter the cave environment episodically regardless of the season. The former explanation is consistent with a strong seasonal control of growth fabrics. The latter explanation is at odds with the timing of cool season cave ventilation (air movement into the cave), the regularity of growth layering documented within portions of the study interval, and the occurrence of the high-impurity growth layers in stalagmites far from cave entrances. If background detrital input is low, high inclusion densities (marking horizons of incomplete intercrystallite coalescence), may instead provide the principal evidence of stalled growth fronts. Our interpretation of inclusions (±organic colloids) associated with seasonally stalled growth fronts driving fluorescence differs from other cave systems having drip waters with subannual residence times in the epikarst. For example, Orland et al. (2012) attribute bright-to-dim fluorescent growth band cycles in Soreq cave speleothems to annual wet season flushing of organic acids that accumulated in the upper soil horizon during the previous dry summer season. Speleothem fluorescence may thus have differing controls.

Although monitoring confirms that modern calcite accumulation in CWN has a seasonal periodicity, CWN-4 growth fabric variations over the study interval could potentially have had a different recurrence rate. We address this by counting the number of growth layers between well-dated U-series datums. The CLFM imagery best resolves the inclusion-rich (i.e., inferred stalled summer growth front) horizons. We compare the number of countable growth couplets in CLFM imagery to the number of annual growth couplets predicted to occur over the same stratigraphic interval using bounding U-series dates. In the upper portion of the SIMS chip, with an estimated growth rate of 89.4 μm/yr, we count 10 and 14 growth bands in Fig. 7A and B, over respective 1.032 mm and 1.235 mm intervals, versus counts of 11.5 and 13.8 predicted over the same distances from U-series constraints. In the lower portion of the SIMS chip, with an estimated growth rate of 37.4 μm/yr, we count 25 growth bands in 1 mm (Fig. 7D), versus 26.9 predicted from U-series. In the middle of the SIMS chip with slowest estimated growth rates (15–21 μm/yr), resolution of countable fluorescent layers is much more limited. We attempted growth band counting in two laterally offset areas (Fig. 7C) from the study interval having slow growth rates of 20.7 μm/yr. Counts of 23 and 25

fluorescent growth bands over distances of 0.625 mm and 0.752 mm are lower than predicted counts of 30 and 36 from U-series. This discrepancy may result from undercounting less distinct layers in the CLFM imagery and/or significant growth rate variations between the bounding U-series age datums. Despite this inconsistency, we note that the stratigraphic frequency of growth layers predicted from U-series interpolation is compatible with the vertical scale of the faint layering, where it is best expressed in this interval (e.g., Fig. 7D). The consistency of layer counting results obtained by these two independent approaches in the moderate and fast growth rate intervals strongly support 1) the hypothesis that the growth layers in CWN-4 accumulated seasonally over the HS1-BA transition study interval, and 2) the interpretation of temporal growth fabric development based on monitoring the modern system and petrographic analysis.

5.4. Stalagmite $\delta^{18}\text{O}$ as a moisture source proxy

The extent to which drip water $\delta^{18}\text{O}$ reflects rainfall $\delta^{18}\text{O}$ is a function of several processes occurring within and above the vadose zone (Section 5.1). In turn, the extent to which stalagmite $\delta^{18}\text{O}$ reflects drip water $\delta^{18}\text{O}$ requires knowledge of how in-cave processes may influence calcite-water oxygen isotope fractionation through equilibrium and kinetic isotope effects. To assess this, we compare oxygen isotopic compositions between drip water and associated calcite deposited on glass substrates for the period of 1998–2008 at four drip sites in two central Texas caves with analogous hydrogeologic and ventilation settings as CWN (Natural Bridge, Cave NB, and Inner Space, Cave IS, Caverns; Feng et al., 2012).

Most substrate calcite $\delta^{18}\text{O}$ values from Caves NB and IS have modest departures from those calculated for equilibrium fractionation: between -0.7‰ and 1.4‰ (using fractionation factor of Coplen, 2007). Such departures are likely due to non-equilibrium (kinetic) isotope effects that may result from rapid CO_2 degassing, calcite precipitation prior to dripping on to substrate surfaces (PCP), and/or Rayleigh distillation as calcite precipitates along surfaces (Mickler et al., 2004; El-Shenawy et al., 2020; Deininger et al., 2021). There is uncertainty around determining the most appropriate fractionation factor to apply in speleothem water-calcite systems that limits our ability to precisely determine the direction and magnitude that substrate calcite samples are offset from expected equilibrium values (Tremaine et al., 2011; Feng et al., 2012; Deininger et al., 2021). Therefore, rather than quantifying the magnitude of departures from isotopic equilibrium, we use constraints on processes (e.g., growth rate, evaporation) that may control the extent of non-equilibrium isotope effects. There is good agreement between laboratory experiments and field monitoring results at Caves NB and IS in terms of the relationship between calcite growth rate and $\delta^{18}\text{O}$ values of calcite. The experimental relationship indicates a -0.8‰ shift of calcite $\delta^{18}\text{O}$ for every ten-fold increase in growth rate ($5\text{--}25\text{ }^\circ\text{C}$, $\text{pH} = 8.3$; Dietzel et al., 2009).

For Cave CWN, we suggest that the stalagmite $\delta^{18}\text{O}$ proxy of drip-water $\delta^{18}\text{O}$ should be most accurate when fed from drip sites analogous to the BD diffuse flow monitoring locality (Fig. 3A), which has sufficiently fast drip rates and sufficiently high humidity to render evaporative effects on drip-water $\delta^{18}\text{O}$ negligible (Feng et al., 2012). These conditions also support calcite accumulation during cool months when seasonal ventilation results in low cave-air CO_2 levels (Fig. 3B and C). Cool season growth rates at the BD monitoring site average 4.3 ± 3.3 mg/day. This modest range of growth rates, relative to the range in Dietzel et al.'s (2009) experimental study, suggests that calcite $\delta^{18}\text{O}$ values should be minimally influenced ($<0.8\text{‰}$) by calcite precipitation rates.

The consistency between local growth layer thickness and

annual thickness predicted from bounding U-series constraints within CWN-4, which yield growth rates that vary over a six-fold range (Section 5.3), is similarly consistent with a minimal influence of growth rate on calcite $\delta^{18}\text{O}$. The SIMS, F200 and M50 $\delta^{18}\text{O}$ transects over the same interval have some offset in absolute values, but all replicate the same negative excursion (Fig. 8A–C). If there are extents of kinetic effects that in some cases exceed the analytical uncertainty of measurements, this replication suggests that the effects were consistent through time. These findings, coupled with evidence for interannual vadose residence times of water supplying drip sites, support that CWN stalagmite $\delta^{18}\text{O}$ compositions are likely to proxy the modal $\delta^{18}\text{O}$ composition of recharge water, and thus mainly long-term (multiyear) variations in the $\delta^{18}\text{O}$ composition of GoM-sourced moisture.

5.5. Calcite growth rate as a moisture amount proxy

Growth rate of speleothems has been widely applied as a moisture amount proxy, typically by inferring a correspondence between growth rate and drip rate, which in turn is inferred to reflect effective moisture (e.g., United Kingdom: Baker et al., 1993; Botswana: Railsback et al., 1994; Norway: Lauritzen, 1995; Belgium: Genty and Quinif, 1996; Namibia: Holmgren et al., 1999; China: Qin et al., 1999; Scotland: Procter et al., 2000; Tasmania: Zhao et al., 2001; Xia et al., 2001; Spain: Stoll et al., 2013; Oman: Fleitmann et al., 2004). Low growth rates are logically expected in settings where rainfall is limited because essential reactants for calcite deposition (H_2O , Ca^{2+} , dissolved CO_2) depend on a positive meteoric water balance to facilitate soil CO_2 production, water-rock interaction, and transport of evolved meteoric water to the drip site (Emmerich, 2003; Mielnick et al., 2005). A number of studies, however, show the complexity in applying this proxy and the need for studies at individual sites, caves or regions to most rigorously assess the environmental processes that govern growth rate (Baker and Smart, 1995; Genty et al., 2001; Fairchild et al., 2006; Banner et al., 2007; Railsback, 2018).

In moisture-limited regions of the SW US, speleothem growth rate and rainfall are correlated. This has been documented both empirically and theoretically. Studies in New Mexico conclude that annual band thickness in speleothems is a measure of effective moisture (Polyak and Asmerom, 2001; Rasmussen et al., 2006; Asmerom et al., 2007, 2013). In Texas, long-term variations in speleothem growth rates across the Edwards Plateau correspond to glacial - interglacial moisture supply variations since the LGM (Musgrove et al., 2001). The growth rate proxy has also been assessed for several drip sites in multiple Texas caves through decadal-scale monitoring studies of cave meteorology, hydrogeology, and calcite growth on artificial substrates placed below drip sites. Such studies demonstrate that average calcite growth rate is a function of average drip rate, with seasonal CO_2 variations - whereby high summer CO_2 levels inhibit calcite precipitation - as a secondary, higher-frequency control (Banner et al., 2007; Cowan et al., 2013; Feng et al., 2014b; James et al., 2015). A role of drip rate in controlling calcite growth is now suggested in CWN, whereby only the faster dripping BD locality accumulates calcite (Fig. 3B). Although the characteristics of the drip site supplying reactants to CWN-4 are unknown, its growth fabric characteristics are consistent with seasonal deposition occurring under steady hydrological conditions that changed systematically through time. These empirical relationships for central Texas caves are consistent with models of calcite deposition kinetics and speleothem growth that accurately predict the effects of variations in water supply (Dreybrodt 1988, 1999; Baker et al., 2014, 2015). Although growth rate is unlikely to be a simple proxy for water supply, particularly in non-water-limited settings (e.g., Frisia et al., 2003), available

moisture is a major control on growth rate for ventilation-style caves across the Edwards Plateau.

5.6. Timing and duration of Bølling negative $\delta^{18}\text{O}$ excursion in CWN-4

The onset of the BA coincides with a major drop in the $\delta^{18}\text{O}$ value of speleothem calcite in CWN-4, which based on monitoring of the modern cave system we interpret to follow a significant change in the $\delta^{18}\text{O}$ value of advected moisture from the Gulf of Mexico into central Texas. The overall negative $\delta^{18}\text{O}$ excursion spanning the entire BA is protracted over a 1600 yr interval, from 14.8 to 13.2 ka, involving a decline of $\sim 2.5\text{‰}$ over ~ 56 mm (Fig. 2C). However, 70% of the total excursion ($\sim 1.7\text{‰}$) occurs in the initial ~ 4 mm, and it is this narrow stratigraphic interval within the HS1-BA transition that we refer to as the HBO (Heinrich Stadial 1-Bølling oxygen isotope excursion event). Specifically, the interval from 76.4 mm to 72.7 mm below the top of CWN-4 contains the most abrupt $\delta^{18}\text{O}$ decline in both the 200- and 50- μm step $\delta^{18}\text{O}$ transects (Fig. 8B).

We use the datums in the 50- μm transect to constrain the timing and duration of the HBO. Three U-series ages within 5.53 mm, two bracketing and one within the HBO interval, indicate respective linear accumulation rates of 15.2 and 20.67 $\mu\text{m}/\text{year}$ (Fig. 8D), which also correspond with the slowest growth rate intervals in the entire HS1-BA transition study interval. The extrapolated lower and upper ages of 14,749 and 14,536 BP, respectively, indicate that the HBO spans a duration of 213 years. The lower bounding U-series age of 14,800 yrs (77.200 mm), marking the onset of slow growth rates in Interval C (Table S3) of the age model, precedes the HBO by 51 yrs (0.783 mm). The upper bounding U-series age of 14,485 (71.679 mm), marking the onset of fast growth rates in interval E (Table S3), follows the HBO by 49 yrs (1.055 mm). These U-series ages have associated uncertainties of ± 50 –80 years (Table S3), which result from instrumental errors and the uncertainty associated with the estimated initial $^{230}\text{Th}/^{232}\text{Th}$ ratio of detrital Th incorporated into a given calcite growth layer; the latter uncertainty has a larger range and is less constrained. The agreement between estimated annual growth rates and the number of growth layers (as quantified in Section 5.3) is consistent with the estimated 213-year duration of HBO. The age datums constraining slow growth rates (intervals C and D in Table S3) are within the range of U-series analytical uncertainty of the extrapolated upper and lower HBO ages. Thus, it is possible that the entire interval of slow growth corresponds with the HBO, or that slow growth initiation slightly preceded the HBO. Regardless, the HBO was entirely associated with markedly slow growth rates, after which growth rates dramatically increased by a factor of 4–6 (Fig. 8D).

5.7. Comparisons with other records of the last deglaciation

The onset of the BA as an interval of abrupt northern Hemisphere warming and global sea level rise is well documented in ice cores, as well as in marine and terrestrial deglacial climate records around the world. Here we assess how the 14.75–14.54 ka HBO interval documented in the CWN-4 stalagmite record compares to these deglacial records. A significant challenge for such comparisons is the extent to which precise and accurate age control can be established among respective records, and expressed in calendar years before present (YBP or BP), or kiloyears before present (ka) where by convention YBP/BP/ka refers to 1950 AD (e.g., Dutton et al., 2017). We review and integrate the locations (Fig. 9), types of proxies and the timing of their abrupt deglacial changes (Table 2, Figs. 10–11), and the uncertainties on the various geochronologic methods used to construct the proxy time series (Sections S2–3). In Figs. 10–11, the CWN-4 record is positioned as the lowest record

and the stadial-interstadial subdivisions derived for Greenland ice cores are shown at the top, and extended vertically. The occurrence of hiatuses (light blue bands) and the HBO (dark blue band) in CWN-4, and the mid-point positions of Heinrich events [dashed black lines: H1.1 (17.1–15.55 ka) and H1.2 (~ 15.9 –14.3 ka)] recognized in the polar North Atlantic (Hodell et al., 2017) are also extended vertically in these figures for comparison with other records.

5.7.1. Greenland ice cores

We compare our central Texas stalagmite record with the sentinel climate record ($\delta^{18}\text{O}$, Ca^{2+}) of the Greenland ice cores (Fig. 11A). High latitude temperature perturbations, such as those that occurred during the last deglacial, can propagate into tropical latitudes via atmosphere-surface and ocean interactions within a few years, changing precipitation and wind intensities (Chiang and Bitz, 2005; Cvijanovic and Chiang, 2013), yet for many regions the teleconnections with high latitude regions are not well known. In the INTIMATE compilation of Greenland ice cores (Rasmussen et al., 2014), the boundary age (onset of GI-1e) between Greenland Stadial 2.1a (\sim equivalent to HS1) and Greenland Interstadial 1 (equivalent to the BA) is $14,642 \pm 4$ BP, with a maximum seasonal ice layer counting error of 186 yrs (Tables 2, S7). The individual core records indicate that the period of most rapid change had durations of ~ 39 –53 years. The estimated onset of the HBO at 14,749 BP is within uncertainty of the start of Greenland Interstadial 1 (GI-1e). Thus, the HBO in central Texas corresponds with the climatic transition from cold stadial to warm interstadial conditions in the North Atlantic, and the single greatest episode of LIS meltwater input to the GoM (Section 5.7.4). Several highly resolved deglacial records (including CWN-4) discussed below show proxy alternations that correspond with GI-1 (BA) interstadial variations between warmer (a, c1, c3, e) and cooler (b, c2, d) climate states, the latter of which have been termed the intra-Bølling cold period, Older Dryas, inter-Allerød cold period in various records (e.g., Hughen et al., 1996; Karpuz and Jansen, 1992). The letters x-y-z are superimposed on these records in Figs. 10–11 to indicate possible correlations with these GI-1 subzone events.

5.7.2. AMOC records

$^{231}\text{Pa}/^{230}\text{Th}$ sediment records for the western subtropical Atlantic document deglacial fluctuations in the intensity of Atlantic Meridional Overturning Circulation (AMOC, Fig. 10B). In the Bermuda Rise, high $^{231}\text{Pa}/^{230}\text{Th}$ production ratios, indicative of sluggish circulation, characterized HS1 and YD stadials, and vigorous circulation marked by low $^{231}\text{Pa}/^{230}\text{Th}$ production ratios characterized the BA (McManus et al., 2004). The abrupt shift in that record from sluggish to vigorous circulation occurs between ~ 14.66 and 14.51 ka (Table 2), and coincides with an abrupt 0.7‰ $\delta^{18}\text{O}$ depletion trend in planktonic foraminifera (*G. inflata*) in the same core. Similarly timed transitions to lower $^{231}\text{Pa}/^{230}\text{Th}$ production ratios occur off South America in the Ceara Rise (Ng et al., 2018; core EW9209-IJPC) between 15.06 and 14.11 ka, with fastest decline after 14.42 ka, and Brazil margin (Mulitza et al., 2017; core Geob16202-2) between 15.29 and 14.12 ka, with fastest decline after 14.57 ka.

5.7.3. Meltwater Pulse – 1a records

The last deglaciation (ca. 19–11 ka) involved several episodes of rapid sea-level rise (Fig. 10D), termed Meltwater Pulses (Clark et al., 2004, 2012; Lambeck et al., 2014). The most significant MW pulse, known as Meltwater Pulse 1a (MWP-1a), is inferred to have involved a 12–22 m sea-level rise within 340 years that approximately coincided with the transition to the BA, ~ 14.7 –14.2 ka (Clark et al., 2012; Deschamps et al., 2012; Ivanovic et al., 2016). Meltwater

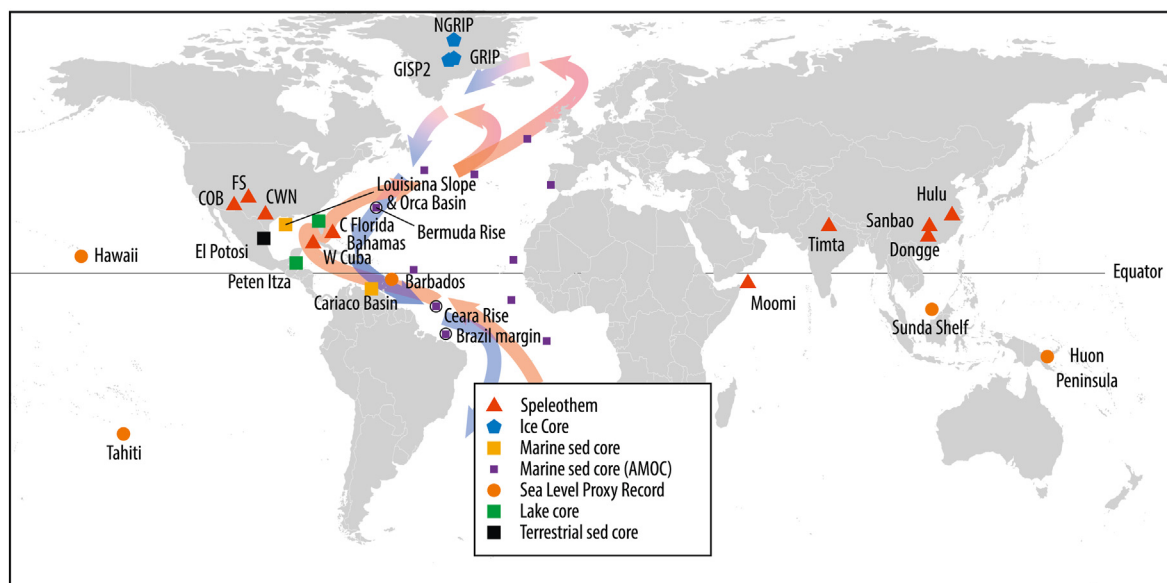


Fig. 9. Global deglacial proxy records considered in this study. CWN, FS, and COB denote Cave Without a Name in central Texas, Fort Stanton Cave in New Mexico, and Cave of the Bells in Arizona, respectively. NGRIP, GRIP, and GISP2 are Greenland ice core records synchronized for the INTIMATE event stratigraphy compilation (Rasmussen et al., 2014). Arrows show shallow (orange) and deep (blue) Atlantic Ocean thermohaline circulation. (For interpretation of the references to color in this figure legend, the reader is referred to the Web version of this article.)

discharging into the North Atlantic likely disrupted AMOC, leading to cold conditions in the North Atlantic and climate change elsewhere through coupled atmosphere-ocean teleconnections (Broecker et al., 1989; Licciardi et al., 1999; Tarasov and Peltier, 2005). In contrast to MW pulses that accompanied cold HS1 and YD stadials, MWP-1a was curiously associated with a resumption in AMOC and North Atlantic warming. The MW source responsible for this rapid flux of freshwater to the ocean over this interval is unresolved, with studies advocating 1) a largely southern hemisphere (Antarctic) source (Weaver et al., 2003; Bassett et al., 2007; Carlson, 2009), 2) limited Antarctic contributions (<4.3 m of eustatic sea level equivalent) (Licht, 2004; Whitehouse et al., 2012; Mackintosh et al., 2014; Golledge et al., 2014), and 3) mainly northern hemisphere contributions (Peltier, 2005; Gregoire et al., 2012; Tarasov et al., 2012; Lin et al., 2021).

The timing and magnitude of MWP-1a is best constrained by U–Th dated Tahiti coral records, that indicate a sea level rise of 14–18 m between 14.65 and 14.31 ka, coincident with the Bølling warming period (Deschamps et al., 2012). This timing is consistent with sea level rise records from the Sunda Shelf, Huon Peninsula, and Hawaii (Table 2, Fig. 10E). The age of the HBO event in the CWN-4 record (14.75 ± 0.08 to 14.54 ± 0.08 ka) falls within the lower and upper age constraints for MWP-1a (14.65 ± 0.02 to 14.31 ± 0.04), consistent with the notion that the same rapid melting episode was the driver of both events. Recognizing the uncertainties of identifying inception and termination points from paleodepth indicators, the 340-year duration for MWP-1a is considered a maximum estimate (Deschamps et al., 2012). The estimated 212 year duration for the HBO event is thus not only compatible with MWP-1a, but it may also constrain the timing of a particularly prominent episode of LIS-derived MW input to the GoM. This is consistent with a sea level fingerprinting study that concludes that 65–80% of MWP-1a's meltwater came from North America, followed by Scandinavia, with a relatively minor Antarctic contribution (Lin et al., 2021).

5.7.4. GoM $\delta^{18}O$ records

CWN's location is most proximal to the northwestern part of the GoM (Fig. 1). Particle tracking and water accounting models for the

present-day conclude that 1) the most frequent air mass trajectories between CWN and the GoM trend NW-SE from the northwestern GoM, 2) the majority of summer and winter precipitation events are associated with these trajectories, and 3) the most common identifiable sources of moisture to central Texas are the GoM and recycled terrestrial moisture (Feng et al., 2014b; Wong et al., 2015). We thus address here deglacial $\delta^{18}O$ records of GoM seawater, in particular from the northwestern GoM.

The low density and significantly lower $\delta^{18}O$ value of deglacial LIS MW (e.g., -35 to -25‰ SMOW; Aharon, 2006) compared to open seawater (e.g., 1 – 2‰ , Vetter et al., 2017) should have entered the GoM as cool, hypopycnal flows that formed a widespread low density surface layer with a $\delta^{18}O$ value more negative than GoM seawater (Emiliani et al., 1978; Oglesby et al., 1989; Aharon, 2003). Direct input of LIS MW into the GoM was originally inferred from foraminiferal $\delta^{18}O$ time series for cores from the western and northeastern GoM, where $\delta^{18}O$ anomalies on the order of -2‰ were superimposed on the expected deglacial seawater $\delta^{18}O$ curve (Kennett and Shackleton, 1975; Emiliani et al., 1975, 1978). Subsequent studies extended foraminiferal $\delta^{18}O$ time series in the northern, southern, western, and northeastern GoM (e.g., Leventer et al., 1982; Williams, 1984; Poore et al., 2003; Nürnberg et al., 2008, 2015). Precise temporal resolution of MW input is limited in most shelfal localities by slow sedimentation rates, bioturbation, and relatively few accelerator mass spectrometry radiocarbon dates. A synthesis of studies along the Louisiana shelf and the Orca Basin slope shows that localities south and west of the Mississippi River Delta preserve evidence of MW input, (Williams, 1984; Flower et al., 2011). LIS MW signatures may have been constrained within the GoM to occur west of the influence of the Loop Current (Emiliani et al., 1975; Nürnberg et al., 2015), or delivered to the deep ocean as well-mixed hyperpycnal flows (Roche et al., 2007). Regardless, northwestern GoM surface waters were most likely to have tracked the input of LIS MW into the GoM through time.

Foraminiferal $\delta^{18}O$ time series between the Louisiana Shelf and Orca Basin (Fig. 10M and N) provide a basis for reconstructing the timing and magnitude of MW flood events for comparison with the CWN-4 record (Fig. 10F). These northwestern GoM records,

Table 2
Regional proxy records, climate change interpretation, and timing of change associated with onset of BA warming.

Location ^a	Manu- script Figure	Record	Change, amount	Proxy change interpretation	Proxy change time period ka (\pm unc ^b)	Reference(s)	Age Model Basis ^c	No. of 15 –14 ka proxy measure- ments	No. of 15–14 ka datums	Avg unc of spanning dates in kyr (n)	Calendar year dates and uncertainties ^d bracketing 15–14 ka interval
Greenland Ice Core localities											
Greenland (NGRIP, GRIP, GISP2)	10A	Dust as proxied by Ca ²⁺ Ice $\delta^{18}O$	Decrease, 100 ppb Increase, 6‰	Decrease in dust source/transport paths Local temperature increase	14.73–14.53 (\pm 0.020)	Rasmussen et al. (2014)	Seasonal layer counting	300	1000	Max counting errors 0.33 –0.17	Dates based on layer counting chronology with maximum counting error between 170 and 330 yrs for the 15–14 ka interval. Composite ice core record is based on 20-yr averaging. This uncertainty is applied to the proxy change interval, but datums could be off by the previously specified counting errors.
AMOC localities											
Bermuda Rise (OCE326-GCC5)	10B	Sediment ²³¹ Pa/ ²³⁰ Th	Decrease, 0.019	Shift to more vigorous AMOC	14.61–14.25 (\pm 0.05)	McManus et al. (2004)	AMS ¹⁴ C on <i>G. inflata</i> , <i>G. 5 ruber</i> (400/IntCal98/Calib 4.3)		3	0.050 (5)	Three bracketing ages: 16,097 \pm 50, 14,523 \pm 50, 14,401 \pm 50, 13,915 \pm 50 BP. Average 2 σ uncertainties for these dates tabulated.
Ceara Rise (EW9209-3JPC)		Sediment ²³¹ Pa/ ²³⁰ Th	Decrease, 0.022	Shift to more vigorous AMOC	14.42–14.11 (\pm 0.404)	Ng et al. (2018)	AMS ¹⁴ C on plank forams (400/MarineCal13)	2	1	1.11 (3)	Three dates constrain the 15–14 ka interval: 16,188 \pm 0.272, 14,484 \pm 0.34, 12,3575 \pm 1.4835 ka. Uncertainties (2 σ) for proxy change interval are from radiocarbon to calendar year age model. Uncertainties (2 σ) for 15–14 ka interval are average uncertainties for closest bracketing dates (bold).
Brazil Margin (GeoB16202-2)		Sediment ²³¹ Pa/ ²³⁰ Th	Decrease, 0.027	Shift to more vigorous AMOC	14.57–14.11 (\pm 0.483)	Mulitza et al. (2017)	AMS ¹⁴ C on plank forams (400 \pm 200/IntCal13)	2	1	0.37 (3)	Mulitza et al., (2017): Core GeoB16202-2 age model is based on 13 accelerator mass spectrometry radiocarbon dates on planktonic foraminifera (<i>Globigerinoides ruber</i> and <i>Globigerinoides sacculifer</i>). Intervals of interest tabulated heret have three bracketing ages: 16.365 \pm 0.398; 14.528 \pm 0.471; 13.047 \pm 0.242 ka. Uncertainty (0.47 kyr) for proxy record interval is average 2 σ based on radiocarbon to calendar year age model. Uncertainty (0.37 kyr) for 15–14 ka interval is average 2 σ uncertainty based on radiocarbon to calendar year age model for bracketing ages.
N. & Tropical Atlantic Sites (13)		Sediment ²³¹ Pa/ ²³⁰ Th (9 pt mov avg)	Decrease, 0.021	Shift to more vigorous AMOC	15.52–14.07 (\pm 0.290)	Ng et al. (2018)	AMS ¹⁴ C on plank forams (400/MarineCal13)	15	6	0.265 (6)	Age control for this composite is based mainly on AMS ¹⁴ C. Uncertainties for proxy change interval are 2 σ based on radiocarbon age conversion model for proxy change period and based on age error of datums. Uncertainties for 15–14 ka interval are 2 σ based on the average of bracketing dates; from Ng et al. (2018); personal communication 2021.
Meltwater Pulse – 1a records											
Barbados	10D-E	Coral (mainly Acropora palmata) elevations/sea level indicator	Abrupt deepening of coral assemblages	Sea level rise of 20 m	14.082 \pm 0.056 –13.605 (\pm 0.042)	Fairbanks (1989); Bard et al. (1990); Fairbanks et al. (2005); Peltier and Fairbanks (2006)	²³⁰ Th/U	0	7	0.044 (7)	Proxy change time period from Deschamps et al. (2012). Proxy time period ages and uncertainties (converted to 2 σ) from Peltier and Fairbanks (2006) for sample RFG 9-8-2 and average of samples RFG 12-21-7 and RFG-21-10. No. of 15–14 ka measurements and uncertainties (1 σ x 2) from Peltier and Fairbanks (2006). Same as above
					14.3–14.0	Liu and Milliman (2004)					

Table 2 (continued)

Location ^a	Manu- script Figure	Record	Change, amount	Proxy change interpretation	Proxy change time period ka (\pm unc ^b)	Reference(s)	Age Model Basis ^c	No. of 15 –14 ka proxy measure- ments	No. of 15–14 ka datums	Avg unc of spanning dates in kyr (n)	Calendar year dates and uncertainties ^d bracketing 15–14 ka interval
Yemen (Moomi Cave)	10H	Stalagmite $\delta^{18}\text{O}$	Decrease, 1 –2‰	Monsoon intensity increase	14.53–14.43 (\pm 0.17)	Shakun et al. (2007)	²³⁰ Th/U	62	4	0.176 (6)	Six bracketing dates: 15.908 \pm 0.214, 14.931 \pm 0.183, 14.534 \pm 0.122, 14.428 \pm 0.168, 14.199 \pm 0.183, 13.558 \pm 0.183. Average 2 σ age uncertainties tabulated.
North India (Timta Cave)	10I	Stalagmite $\delta^{18}\text{O}$	Decrease, 2‰	Monsoon intensity increase	15.2–14.3 (\pm 0.3)	Sinha et al. (2005)	²³⁰ Th/U	80	2	0.281 (3)	Three bracketing dates: 14.580 \pm 410, 14,220 \pm 230, 13,800 \pm 200. Average 2 σ age uncertainties tabulated
South China (Dongge Cave)	10J	Stalagmite $\delta^{18}\text{O}$	Decrease, 1.8‰	Monsoon intensity increase	14.76–14.57 (\pm 0.11)	Dykoski et al. (2005)	²³⁰ Th/U	24	2	0.104 (4)	Four bracketing dates: 15,541 \pm 95, 14,835 \pm 114, 14,117 \pm 103, 13,638 \pm 104. Average 2 σ age uncertainties tabulated
Central China (Sanbao Cave)	10K	Stalagmite SB $\delta^{18}\text{O}$	Decrease, 1.4‰	Monsoon intensity increase	14.74–14.54 (\pm 0.10)	Wang et al. (2008)	²³⁰ Th/U	49	0	0.100 (2)	Two bracketing dates: 15.1 \pm 0.1; 13.5 \pm 0.1. Average 2 σ age uncertainties tabulated
Eastern China (Hulu Cave)	10L	Stalagmite YT, H82 $\delta^{18}\text{O}$	Decrease, 1.4 –2‰	Monsoon intensity increase	14.74–14.55 (\pm 0.06)	Wang et al. (2001)	²³⁰ Th/U	PD 15; YT 52; HB 220	PD 3; YT 1; HB 0	PD 0.361 (3); YT 0.101 (2); HB 0.101 (2)	Three stalagmites with 7 bracketing dates: PD 0.361 (3): 15,123 \pm 464, 14,555 \pm 391, 12,962 \pm 227; YT 0.101 (2): 15,908 \pm 59, 14,613 \pm 71; HB 0.101 (2): 16,115 \pm 105, 11,052 \pm 97. Average 2 σ age uncertainties tabulated; fastest $\delta^{18}\text{O}$ decrease of 180 yrs centered at 14.645 \pm 0.060 based on band counting.
Circum-GoM terrestrial localities											
Texas (Cave Without A Name)	10F, 11A	Stalagmite CWN-4 $\delta^{18}\text{O}$ Growth rate	Decrease, 1.6‰ Increase, 4.3x	Meltwater input to GoM Increase in rainfall	14.75–14.54 (\pm 0.08) 14.62–14.49 (\pm 0.08)	This study Feng et al. (2014b)	²³⁰ Th/U	106 6	6	0.080 (8)	Eight bracketing dates: 13,910 \pm 70, 14,060 \pm 50, 14,380 \pm 80, 14,485 \pm 50, 14,620 \pm 80, 14,800 \pm 80, 14,910 \pm 50, 15,300 \pm 50. Max 2 σ age uncertainties among bracketing dates tabulated.
NW GoM (Orca Basin core MD02-2550)	11M- N, 12B	Planktonic foraminifera	Foram barren core interval 455–431 cm	MW-driven salinity reduction	14.66–14.11 (\pm 0.33)	Williams et al. (2010); Vetter et al. (2017)	AMS ¹⁴ C on white & pink <i>G. ruber</i> (405/ MARINE09)	38	6	0.330 (8)	Eight bracketing dates: 13.953 (+0.144/ –0.157), 14.033 (+0.162/–0.157), 14.662 (+0.461/–0.41), 14.418 (+0.332/–0.499), 14.437 (+0.328/–0.491), 14.833 (+0.344/ –0.341), 14.444 (+0.329/–0.49), 15.042 (+0.423/–0.219) ka. Tabulated 2 σ uncertainty (0.330 kyr) is average among bracketing ages in Williams et al. (2010).
NW GoM (LOUIS core composite)	Not shown	Planktonic and benthonic foraminifera $\delta^{18}\text{O}$	Decrease, 2‰	Meltwater Flood-3 involving hyper- and hypopycnal flows (contemporary with MWP-1a)	14.97–14.46 (\pm ???)	Aharon (2003), 2006	AMS ¹⁴ C on white <i>G.</i> <i>ruber</i> (400/CALIB5.0)	39	2	??? (4)	Revised age model from 6 AMS radiocarbon dates from <i>G. ruber</i> (white) shells in Aharon (2003) converted to calendar years using most recent CALIB 5.0 at 2 σ confidence level. For 15- 14ka interval, constraining ¹⁴ C ages (1s unc) are 14.4 \pm 0.32, 12.6 \pm 0.13, 12.2 \pm 0.12, 11.2 \pm 0.19, which correspond to age model calendar years of 16.85, 14.59, 14.09, and 12.83 ka. Corresponding calendar year uncertainty not published.
Northeast Mexico	11D	Basin sediment Ti	Increase, ~0.25%–17.5 to 13 ka†† with pulse at ~15 –14.5 ka	Increase in rate of runoff	~15–14.5 (\pm 0.17)	Roy et al. (2016)	AMS ¹⁴ C on bulk sed (0/ INTCAL13)	unpublished 0	0	0.165 (2)	Two bracketing dates: 19,690 (+220/–130), 13,890 (+170/–140) BP; tabulated 2 σ uncertainty is the average from age model (from Table 1, Roy et al., 2016). Approximate age range of increase in Ti% obtained graphically from Fig. 6, Roy et al., 2016).
Florida	11G	Lake pollen	Decrease in Pinus, ~40%;	Deglacial transition to	~15.6–12.8 (\pm 0.19)	Grimm et al. (2006)	AMS ¹⁴ C on bulk sed (0/ INTCAL04)	4	0	0.192 (2)	Eight dates over proxy change time period: 16,050 (+193/–208, 15,007 (+131/–113),

			Increase in Quercus, ~30%	cooler and drier climate								13,862 (+72/-80), 13,585 (+84/-96), 13,542 (+73/-85), 12,901 (+27/-36), 12,813 (+39/-30), 11,857 (+134/-134) BP; uncertainties are 1σ about the 50% median probability age. Tabulated (0.192 kyr) uncertainty is average 2σ for 15–14 ka ages used in the age model
Bahamas	11E	Stalagmite δ ¹⁸ O	Decrease, 2.4‰ 14.98–13.93; Rapid decrease, 2‰ 14.98–14.96 ka	Post HS1 warming	14.98–13.93 (±0.2)	Arienzo et al., 2015, 2017	²³⁰ Th/U	218	3	0.191 (4)	Bracketing dates (4) are: 17,244 ± 246, 14,902 ± 174; 14,872 ± 178; 14,468 ± 166 BP. Tabulated 2σ age uncertainty (0.191) is average of bracketing dates.	
Cuba	11F	Stalagmite growth rate	Increase, 4x between slow growth/hiatuses during H1.1 and YD	Unexplained in reference; Increase in deglacial rainfall?	16.39 (±0.17) - 13.0 (±0.16)	Warken et al. (2019)	²³⁰ Th/U	100	1	0.903 (3)	Deglacial age model based on: MC-ICP-MS: 24.34 ± 0.21, 20.11 ± 0.19, 16.39 ± 0.17; 15.89 ± 2.13; 14.55 ± 0.42; 13.00 ± 0.16 ka; TIMS: 9.29 ± 0.23; 8.19 ± 0.46 ka. Tabulated 2σ age uncertainty (0.903 kyr) is average of bracketing ages (bold). Hiatus from 13–9.29 ka.	
		Stalagmite δ ¹⁸ O	Rel constant (-4.2 ± 0.6‰) from H1.1 to YD; higher than Holo	Persistent dryness, relative to older glacial, due to shifted Caribbean LLJ?								
Yucatan Peninsula (Lake Petén Itzá)	11C	Magnetic susceptibility (SI) of lake lithologies	Increase, 33 SI units	Post HS1 wetter climate	14.74 (-0.40/+0.38) - 14.64 (-0.43/+0.40)	Hodell et al., 2008; Escobar et al., 2012	AMS ¹⁴ C on 44 terrestrial macrofossil from 3 cores, mutually correlated from magnetic susceptibility, 39 (0/INTCAL09)	93	1	0.402 (3)	Bracketing dates are: 15,860 ± 629.5; 14,565 ± 438.5; 13,734 ± 139 BP, with 2σ uncertainties from age model in Escobar et al., 2012. Tabulated (0.402 kyr) uncertainty is average from bracketing ages.	
		Ostracod δ ¹⁸ O	Decrease, 1.4‰	Post HS1 warming, precipitation increase	14.68–14.20 (±0.40)	Escobar et al. (2012)						
		Ostracod paleoecology, δ ¹⁸ O, δ ¹³ C	Increase in deep water fauna; Decrease in δ ¹⁸ O, 2.5‰; Decrease in δ ¹³ C, 4‰	Increase in lake level associated with post HS1 warmer and wetter climate	Parallels mag susc. increase (above)	Pérez et al., 2013						

^a Details of proxy records given in Supplementary Information.

^b Uncertainty is typical uncertainty for age determinations used to bracket interval of interest. Details of geochronology given in Supplementary Information.

^c For AMS¹⁴C geochronology, parentheses enclose the reservoir correction years applied and method used to derive calendar years (#/method).

^d Uncertainties are 2-sigma; unless otherwise specified.

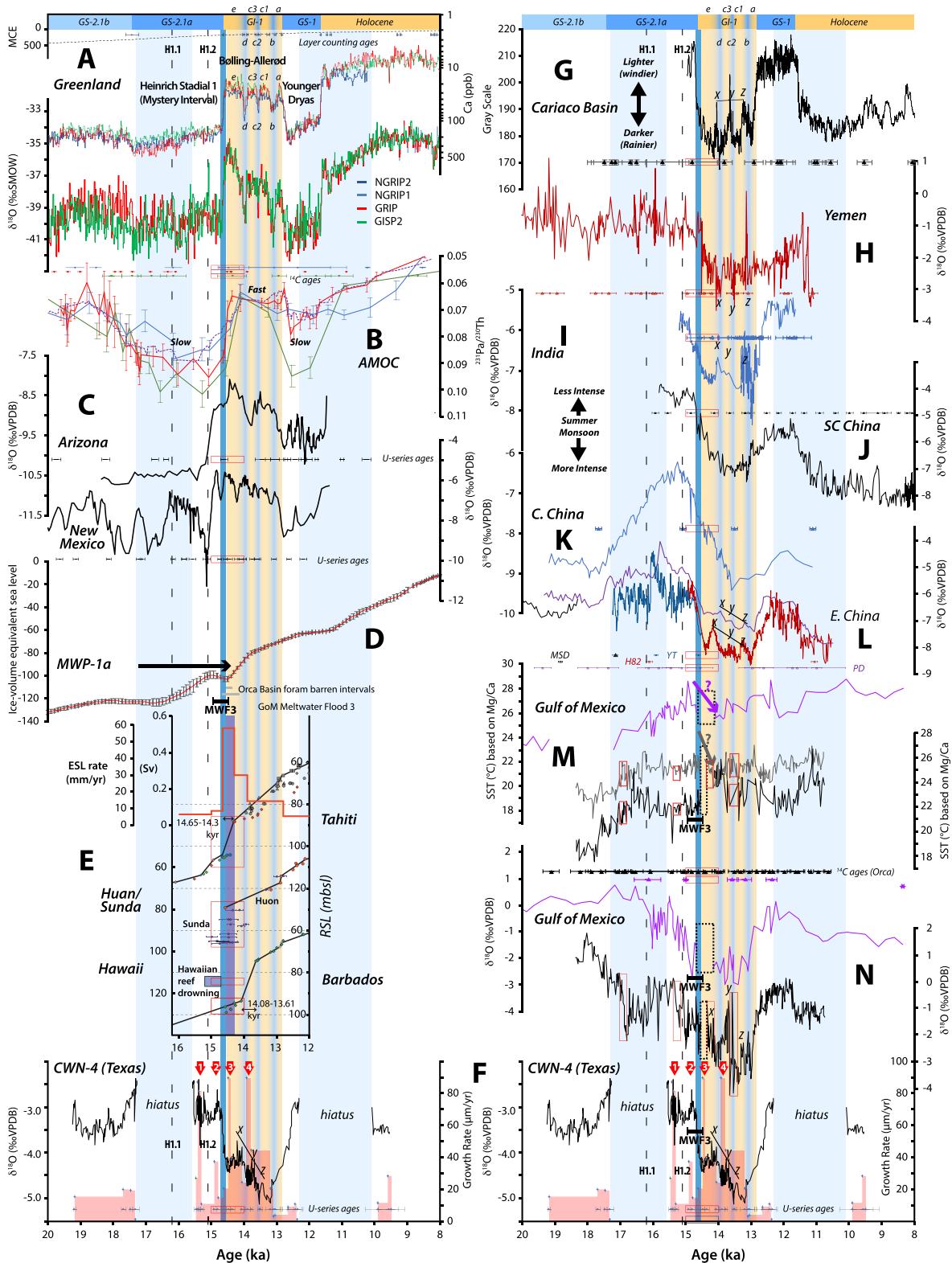


Fig. 10. Comparison of Texas stalagmite CWN-4 $\delta^{18}\text{O}$ and growth rate record with other deglacial records over the 20–8 ka time window. Red boxes show 15–14ka age control in each record as compiled in Table 2. **A.** Greenland ice core $\delta^{18}\text{O}$ (‰SMOW) and Ca (dust) concentrations, and corresponding stadial-interstadial subdivisions (Rasmussen et al., 2014). MCE = mean layer counting error. Heinrich Stadial 1 (aka Mystery Interval), Bølling-Allerød, and Younger Dryas climate intervals respectively correspond with GS-2.1a, GI-1, and GS-1 ice core intervals, although are defined in other archives. Within GS-2.1, the mid-point temporal positions of Heinrich events H1.1 (~16.2ka; 17.1–15.5 ka) and H1.2 (~15.1 ka; 15.9–14.3 ka) in Hodell et al. (2017) are shown as vertical dashed lines. Within GI-1 (Bølling-Allerød), warm (tan intervals: a, c1, c3, 4) and cold (blue intervals: b, c2, d) episode are continued downwards in the background for comparison with other records. **B.** Atlantic meridional overturning circulation (AMOC) records ($^{231}\text{Pa}/^{230}\text{Th}$) and ^{14}C age control in the western subtropical Atlantic: Bermuda Rise (red curve, McManus et al., 2004); Brazil Margin (green curve, Miltzta et al., 2017); Ceara Rise (blue curve) and Atlantic composite (purple curve, Ng et al., 2018, described in Supplement Section 3). **C.** Western North American (WNA) speleothem records and U-series age control from New Mexico (Fort Stanton Cave, Asmerom et al., 2010) and Arizona (Cave of Bells, Wagner et al., 2010). **D.** Estimated ice-volume corrected sea level (ESL) and MWP-1a

separated by up to 185 km, demonstrate that prominent MW influence in the GoM began during HS1 and continued through the BA (Williams et al., 2012) and, as noted by Feng et al. (2014b), there is a striking similarity between the deglacial CWN-4 $\delta^{18}\text{O}$ record and corresponding GoM foraminiferal $\delta^{18}\text{O}$ records (Fig. 10F, M-N). LIS MW input likely involved several MW flood (MWF) episodes rather than one continuous event (Aharon, 2003). With an advanced chronology, Aharon (2006, personal communication) identified MWF-3 (14.97–14.46 ka) as most closely approximating MWP-1a (Table 2). The MWF-3 signature is recorded in two Louisiana shelf cores 100 km apart by foraminifera that lived in both shallow and deep parts the water column. Regional evidence, including changes in erosion intensity (e.g., spike in reworked nannofossils in Orca Basin core EN32-PC4 234–256 cm; Marchitto and Wei, 1995), sediment load, and runoff, supports the hypothesis that MWF-3 was an exceptionally strong MW flood event that involved hyperpycnal flows over a substantial area of the GoM, and was likely contemporaneous with MWP-1a (Aharon, 2006).

A high-resolution Orca Basin core (MD02-2550, Biller, 2012) has a conspicuous foraminifera-barren interval (homogeneous interval at 456–437 cm; Meckler et al., 2008), constrained by a radiocarbon age model to be 14.66–14.11 (± 0.40) ka, and may thus reflect an influx of terrigenous material and low-salinity water associated with MWP-1a (Table 2). The age and duration of the HBO event in the CWN-4 record (14.75 ± 0.08 to 14.54 ± 0.08 ka, ~ 210 yrs) occurred within uncertainty of this foram-barren interval. This temporal agreement supports a significant influx of LIS MW into northwestern GoM that coincided with MWP-1a and the Bølling warming period, but also suggests that the impact of MWP-1a on GOM surface water $\delta^{18}\text{O}$ composition is likely missing or dampened in Orca Basin foraminiferal records. The CWN-4 record may thus provide new insights as an index of GoM surface water $\delta^{18}\text{O}$ composition, considering its seasonal deposition from drip water that is likely a well-mixed average of predominantly GoM-sourced annual precipitation. On the other hand, CWN-4 did not grow during portions of cold stadials (HS1, YD), and thus provides no record of the GoM moisture source, except that it did not provide significant recharging moisture to central Texas during these periods.

Over the HBO, 50 μm spatial sampling resolution for the M50 IRMS transect (Fig. 8) corresponds to temporal sampling resolution between 0.6 and 3.3 years, and is thus likely to be comparable to the interannual residence times of drip waters. Even if capable of $\delta^{18}\text{O}$ precision equivalent to IRMS, the small sampling footprint of SIMS (~ 10 μm), offering temporal resolution between 0.1 and 0.7 years, could only obtain an interannual average of precipitation. The lack of evidence for strong $\delta^{18}\text{O}$ oscillations in the HBO record (Fig. 8) suggests that the flux and/or $\delta^{18}\text{O}$ of LIS MW input was relatively

constant over this timescale. Vetter et al. (2017) suggest that LIS MW entering the GoM was isotopically heterogeneous, ranging between -11% and -38% , and becoming more negative between 15.5 and 13.3 ka. Considering that LIS MW input was likely highest during summers, some seasonality in GoM surface water $\delta^{18}\text{O}$ compositions is possible. However, preservation of such high resolution $\delta^{18}\text{O}$ variations from the CWN-4 record would be obscured by the interannual residence time of dripwater.

5.7.5. Western North American speleothems

Statistical analysis and network visualizations of speleothem $\delta^{18}\text{O}$ records from western North America (WNA) show temporal shifts associated with climate change events of the last deglaciation that are broadly consistent within the WNA region, and that reflect differing controls on the $\delta^{18}\text{O}$ of rainfall across the region (Oster and Kelley, 2016). These speleothem records are also consistent with deglacial records from other regions, including those discussed throughout Section 5.7 and shown in Table 2.

Exemplifying the WNA trend is a regional transect from Texas to New Mexico to Arizona (Figs. 1C and 10F, C). The Texas CWN-4 stalagmite exhibits a broad decrease in $\delta^{18}\text{O}$ of nearly 3‰, starting ~ 15.5 ka and ending with a nearly equivalent $\delta^{18}\text{O}$ increase across the BA to YD transition (~ 13 – 12.5 ka). In contrast, both the New Mexico and Arizona stalagmites show an increase and then decrease in $\delta^{18}\text{O}$ across this same interval (Feng et al., 2014b). The initial increase in Arizona closely coincides with the initial CWN-4 decline, whereas the increase in New Mexico lags by ~ 100 yrs. The most abrupt CWN-4 $\delta^{18}\text{O}$ decline (1.7‰) within that interval defines the HBO of the present study (Table 2; Fig. 8). The HBO intersects with a ~ 500 yr plateau in $\delta^{18}\text{O}$ values in the Arizona record and with a distinct $\sim 1.5\%$ negative excursion spanning ~ 290 years in New Mexico (Fig. 10F, C; Table 2). Although the Arizona record has limited age control, the opposite sign and broadly synchronous timing of the Texas deglacial response relative to the New Mexico and Arizona response (and most other WNA speleothem records) can be accounted for by the same process – mixing of multiple moisture sources having different $\delta^{18}\text{O}$ values and temporal patterns. A dominant, persistent influence from a GoM moisture source (high $\delta^{18}\text{O}$) for Texas contrasts with a dominantly westerly storm Pacific moisture source (low $\delta^{18}\text{O}$) relative to the GoM for the other WNA localities (Feng et al., 2014b). The unique temporal trend of a rapid decrease in GoM $\delta^{18}\text{O}$ through the deglaciation is mirrored by the CWN-4 record (Fig. 10F), yet it is also consistent with $\delta^{18}\text{O}$ increases observed through the same time interval in New Mexico and Arizona (Fig. 10C, Table 2). In this scenario, periods of increased moisture flux from the GoM relative to the normally dominant Pacific moisture source to WNA, results in a net increase in speleothem $\delta^{18}\text{O}$ because the meltwater-influenced GoM $\delta^{18}\text{O}$

based on integration of global proxy records (Lambeck et al., 2014). Timeframes for proxy records delimiting MWP-1a and for MWF-3 and Orca Basin foram-barren intervals in the Gulf of Mexico also shown. E. Detailed relative sea-level (RSL) records spanning MWP-1a, including U–Th dated corals (Barbados, Hawaii, Huon, Tahiti) and ^{14}C -dated mangrove organic matter (Sunda), as modified from Deschamps et al. (2012). Pacific Ocean records are consistent with MWP-1a occurring 14.65–14.30 ka (purple vertical rectangle), whereas the Barbados record indicates MWP-1a occurred 14.08–13.61 ka (light green vertical rectangle). Glacial meltwater discharge (ESL) in mm/yr and sverdrup (Sv) volumetric flow units (Sv; $1 \text{ Sv} = 1 \times 10^6 \text{ m}^3/\text{s}$) estimated from the Tahiti Record. F. Texas CWN-4 $\delta^{18}\text{O}$ and growth rate record (pink histogram). Positions of hiatuses (light blue fields) and the prominent negative $\delta^{18}\text{O}$ excursion between Heinrich Stadial 1 and the Bølling-Allerød (HBO, dark blue field) are continued upward for comparison with other records. Red numbered arrows show positions of fast-growth intervals. Letters x, y, z show small $\delta^{18}\text{O}$ inflections that may correlate to warm and cold events within Greenland G1-1. G. Cariaco Basin sediment grey scale reflectivity for core PL07-56 PC (Hughen et al., 2000). Lighter colored intervals (higher grey scale values) correspond with higher wind-driven upwelling and productivity, considered to have been driven by higher thermal gradients associated with cold north Atlantic climate states. Darker colored intervals (lower grey scale values) correspond with greater proportions of detrital runoff when latitudinal thermal gradients were lower (warmer north Atlantic) and productivity was lower. Accelerator mass spectrometry radiocarbon dates on foraminifera integrated with varve chronology from core PL07-58 PC provide nearly continuous age control. H–K. Indo-Asian stalagmite $\delta^{18}\text{O}$ records demonstrating changing summer monsoon intensity: H. Moomi Cave, Yemen; I. Timta Cave, India; J. Dongge Cave, China; K. Sanbao Cave, China; L. Hulu Cave, China, stalagmites MSD, H82, PD; letters x–y–z in various records denote possible correlations with warm and cold events within G1-1. U-series age control shown for each record; some records correlated from annual band counting and $\delta^{18}\text{O}$ inflections. M–N. Gulf of Mexico Mg/Ca SST estimates (M) and $\delta^{18}\text{O}$ variations (N) from Orca Basin foraminifera in cores MD02-2550 (black curve; Williams et al., 2012) and EN32-PC6 (purple curve; Flower et al., 2004). Foraminiferal ^{14}C ages converted to calendar years provide age control (shown between M and N). Dashed boxes show positions of homogeneous foram-barren units, considered to have been caused by MWF-3 (Aharon, 2006). Downward arrows in M show potential SST cooling across MWF-3. Letters x–y–z in N show possible correlations with the CWN-4 record (F) that may correspond to warm and cold events in the Greenland G1-1 ice core record (A). (For interpretation of the references to color in this figure legend, the reader is referred to the Web version of this article.)

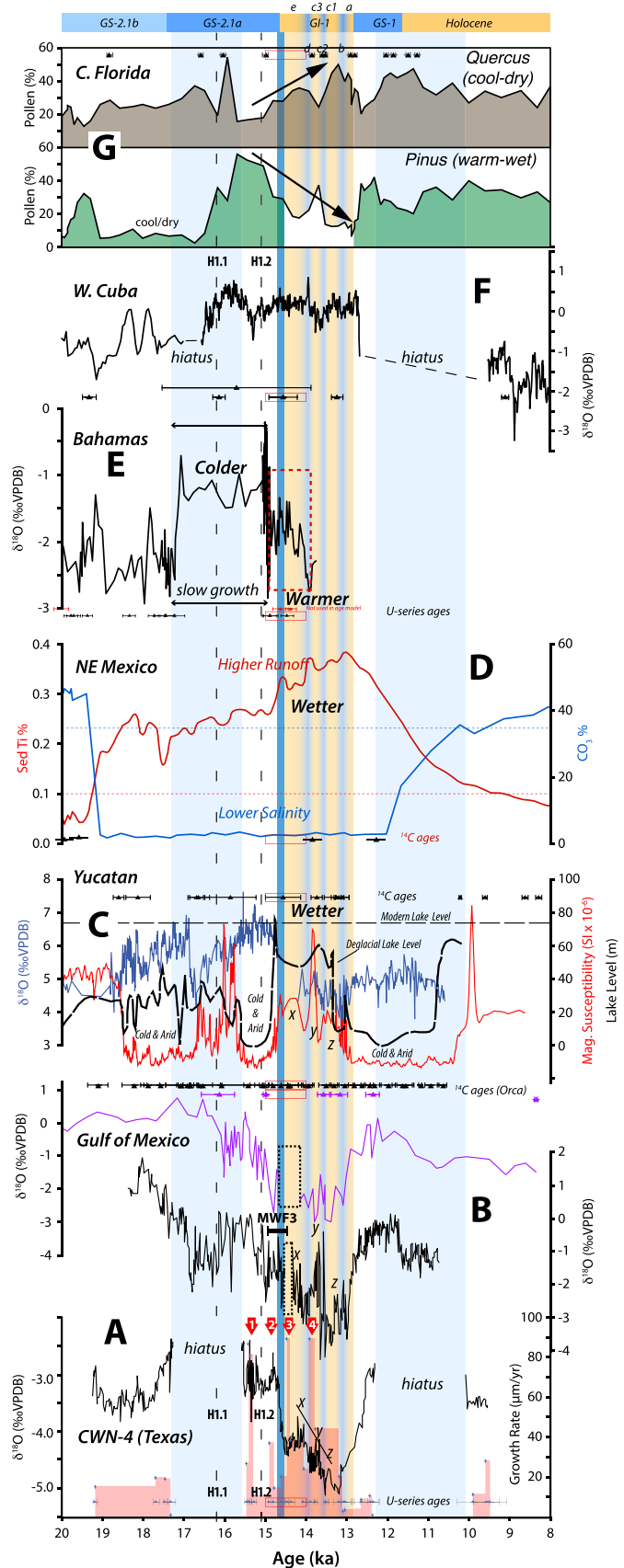


Fig. 11. Comparison of CWN-4 $\delta^{18}\text{O}$ and growth rate record with circum-Gulf of Mexico deglacial records over the 20–8 ka time window. Same as Fig. 10, Greenland stadal and interstadial divisions are shown at the top and GI-1 warm (yellow: a, c1, c3, 3) and

signal is still higher than the Pacific $\delta^{18}\text{O}$ moisture signal (Feng et al., 2014b). A major contrast for CWN-4 is its growth rate of zero during the prior deglacial (~17.3–15.6 ka; within HS1), but all three records stopped growing within the YD. Hiatus initiation appears to have been ~800 years earlier at CWN-4 (~12.3 ka) than at New Mexico (~11.4 ka) and Arizona (~11.5 ka), perhaps because the suppression of GoM moisture had a large/earlier impact in Texas compared to New Mexico and Arizona, which must lose both GoM and Pacific sources to go ‘full hiatus’. Among these records, stalled or reduced growth rates thus notably accompanied cold stadial intervals. Compared with other WNA speleothem $\delta^{18}\text{O}$ records, CWN-4 stands out in displaying moderate to strong positive correlations with Cariaco Basin (0.80) and Indo-Asian Monsoon records (0.59–1.00, avg: 0.78), considered below, which have been linked to deglacial changes in AMOC and latitudinal migration of the ITCZ (Oster and Kelley, 2016).

5.7.6. Cariaco Basin

Sediment reflectance records in the anoxic Cariaco basin (Fig. 10G) show seasonal variations inferred to be driven by north-south migrations of the ITCZ over the last 15 kyr (Hughen et al., 1996). Lighter laminae (marine components) are deposited in winter (southward ITCZ shift) in response to enhanced Ekman upwelling caused by stronger trade winds. Darker laminae (terrigenous components) are deposited in summer (northward ITCZ shift) reflecting higher rainfall and runoff from the Venezuelan margin. These reflectance changes follow the intensity of North Atlantic trade winds, which respond to changes in the temperature gradient in the North Atlantic (Hughen et al., 1996; Overpeck et al., 1989; Rind et al., 1986). The Cariaco record parallels the Greenland

cool (blue: b, c2, d) episodes, North Atlantic Heinrich events H1.1, H1.2, and the CWN-4 HBO (dark blue) and hiatus (light blue) intervals are stretched vertically for comparison with other records. Red boxes show 15–14 ka age control in each record. A. Texas stalagmite CWN-4 $\delta^{18}\text{O}$ and growth rate record (same as Fig. 11F). B. Orca Basin foraminiferal $d^{18}\text{O}$ record from cores MDO2-2550 (black curve) and EN32-PC6 (purple curve), showing position of MWF-3 and foram-barren interval (same as Fig. 11M). C. Lake Peten Itza (Guatemala, Yucatan Peninsula) drill core records and ostracod $\delta^{18}\text{O}$ (Hodell et al., 2008; Escobar et al., 2012; Pérez et al., 2013). Magnetic susceptibility (SI, red curve) of lake sediments fluctuates between enrichments in clay (high SI, wet climate), such as characterized the BA, and gypsum (low SI, arid climate), such as characterized the LGM, HS1 and YD. Benthic ostracod *Limnocythere opesta* $\delta^{18}\text{O}$ values (blue curve) are more depleted during warm intervals associated with high lake levels (black dashed curve). The timing of SI and ostracod $\delta^{18}\text{O}$ fluctuations in the Guatemala record are similar to $\delta^{18}\text{O}$ fluctuations in the Orca Basin foraminifera and Texas CWN-4 stalagmite record. Ostracod-estimated lake level indicates an abrupt 60m increase near the HBO consistent with a rapid shift to a wetter climate. x-y-z letters show possible correlations between the Guatemala SI record and Greenland GI-1 warm-cold fluctuations. D. El Potosi Basin (NE Mexico) deglacial lake sedimentary evolution (Roy et al., 2016) has sparse ^{14}C age control, but demonstrates an overall increase in riverine runoff (wetter climate) as proxied by sedimentary Ti abundance, which increases near the HBO boundary through the BA and then decreases in the YD. Carbonate content is a proxy of authigenic carbonate formation from saline waters. Low carbonate content through the 19–12 ka interval, and its negative correlation with Ti abundance, indicate more saline basin waters in the LGM and YD when climate was dryer. E. Bahamas (Abaco Island) submerged stalagmite AB-DC-09 $\delta^{18}\text{O}$ record and U-series age control (Arienzo et al., 2015). The HS1-BA transition to 1–2‰ lighter $\delta^{18}\text{O}$ values (dashed red box) is interpreted to reflect a temperature increase on the order of 4 °C. An interval of slow growth in HS1 overlaps with the HS1 hiatus in the Texas CWN-4 record, consistent with cool-arid conditions. F. Western Cuba stalagmite CM $\delta^{18}\text{O}$ record (Warken et al., 2019). Enriched $\delta^{18}\text{O}$ values for the HS1-BA interval compared to Holocene (and older) values were interpreted to reflect lower relative levels of rainfall. Hiatuses at 17.3–15.6 and 12.3–10.1 ka are reasonably consistent with the CWN-4 record, although U-series age control is sparse and variable in the Cuba record. G. Central Florida, Lake Tulane pollen record (Grimm et al., 2006) indicates that deglacial climate shifts were opposite those recorded in other circum-GoM localities. Rather than cold-dry stadials (HS1, YD) and a warm-wet BA, pollen abundances suggest the HS1-BA transition was toward a cooler and dryer climate (*Quercus* > *Pinus*). Accelerator mass spectrometry radiocarbon dates on wood and sediment provide age control. (For interpretation of the references to color in this figure legend, the reader is referred to the Web version of this article.)

ice core records, with cold stadials corresponding to periods with higher trade wind activity and marine productivity and vice versa for warm interstadials. The rapid transition to the BA warming interval occurred between 14.73 and 14.53 ka, with the most abrupt increase occurring during the initial 56 years. Following this ~200 yr transition, which overlaps in time within uncertainty of the HBO at CWN-4 (14.75 ± 0.08 to 14.54 ± 0.08 ka; Table 2), trade wind intensity waned and precipitation increased in the Cariaco Basin. At CWN-4, growth rates jumped from ~21 µm/yr to ~89 µm/yr between 14.62 ± 0.08 and 14.485 ± 0.08 ka (Figs. 2 and 8), similar in time to the inferred increased levels of precipitation in the Cariaco Basin at 14.53 ka. Similar forcing mechanisms are required to account for the synchronicity of decadal to centennial-scale climate events between the Cariaco and the North Atlantic (Hughen et al., 1996). The ~200-yr duration of the HBO in CWN-4 may be somewhat longer than the abrupt transition to higher rainfall in the Cariaco record. This may reflect the longer transfer time for atmospheric warmth to initiate significant LIS melting, compared to a change in trade wind conditions.

5.7.7. Indo-Asian Monsoon speleothems

A series of highly-resolved stalagmite $\delta^{18}\text{O}$ records from localities influenced by changes in the Indian and East Asian Monsoon (Table 2, Fig. 10H-L) track variations in the intensity of monsoon precipitation (Pausata et al., 2011). Strong correspondence of these isotopic variations with Greenland ice core temperature records indicate that changes in monsoon strength in this region followed the pace of millennial-scale climate variations (D-O events) and Heinrich cooling events in the North Atlantic (e.g., Wang et al., 2001). These speleothem time series preserve 1–3.5‰ depletions that indicate monsoon intensification events and offer age constraints relative to the HS1-BA transition for comparison with the HBO in CWN-4. These include records from Yemen (depletion event centered at 14.51 ka; Fig. 10H), northern India (14.6 ka; Fig. 10I), south China (14.7 ka; Fig. 10J), central China (14.76 ka to 14.66 ka; Fig. 10K), and eastern China (14.74 ka to 14.55 ka for two records; Fig. 10L). Initial rapid portions of excursions in best-resolved records have ~200 year durations similar to the HBO in CWN-4 (Table 2, Section S3).

5.7.8. Circum-GoM terrestrial localities

Climatic transitions at the start of the BA are also recognized in several terrestrial circum-GoM localities shown in Fig. 11. Although age control in these records is sparser and of lower precision compared to the records examined above, the interpreted temperature and precipitation patterns demonstrate a broadly synchronous pattern of climate change in much of the circum-GoM region. Among these, records from Florida and to a lesser extent Cuba show important contrasts.

Yucatan. Sediment mineralogy and ostracod $\delta^{18}\text{O}$ studies of Lake Petén Itzá, Guatemala (Hodell et al., 2008; Escobar et al., 2012; Pérez et al., 2013) reflect alternating wet and dry deglacial climate conditions (Fig. 11C). The wet-dry time series is similar to the temperature record of Greenland ice cores, whereby cold stadials correspond to arid conditions. A switch from arid to moist conditions occurs between HS1 and the BA at ~14.7 ka, with moist conditions persisting until a sharp return to dry conditions at the onset of the YD (~12.8 ka). CWN-4 growth rates mirror this behavior, with stalled accumulation during HS1 (17.3–15.5 ka) and YD (13.0–9.9 ka) – when Petén Itzá recorded dry conditions, and fastest growth rates during the BA – when Petén Itzá records wet conditions. The lake rapidly filled across the HS1-BA transition (Fig. 11C), consistent with a rapid increase in moisture delivery to the region at this time (Pérez et al., 2013).

Northeast Mexico. The sedimentary record for El Potosi Basin

(Roy et al., 2016) records wetter conditions (proxied by abundance of Ti-bearing clastics) that increased during the last deglaciation (HS1-BA) and reversed during the YD (Fig. 11D).

Bahamas. Paired fluid inclusion and calcite $\delta^{18}\text{O}$ values for four stalagmites from a submerged cave are used to reconstruct temperature across HS 1–3 (Fig. 11E; Arienzo et al., 2015, 2017). Stadial to interstadial transitions are marked by negative $\delta^{18}\text{O}$ excursions, with lower temperatures during Heinrich stadials. The HS1-BA transition is best recorded as a rapid ~1–2‰ decrease in $\delta^{18}\text{O}$ between ~14.9 and 13.9 ka and inferred ~4 °C temperature increase. Within the sparse age control, the timing and duration for the HS1-BA transition are compatible with the HBO in CWN-4 (Table 2). This is consistent with a shift to warmer and wetter conditions in the northern tropics at the start of the BA in response to the resumption in AMOC following HS1, that increased North Atlantic SST and shifted the ITCZ northward (Peterson et al., 2000; McManus et al., 2004).

Cuba. $\delta^{18}\text{O}$ values for Stalagmite CM from Cuba are interpreted to follow precipitation amount, with higher values corresponding to drier conditions (Warken et al., 2019, Fig. 11F). North Atlantic climate variability, insolation, and AMOC strength are inferred to be linked to precipitation, with comparatively cool and/or dry climatic conditions during Heinrich stadials and the YD, and wetter conditions during warm D-O cycles. However, the last deglacial from HS1 through the YD, is characterized by the highest $\delta^{18}\text{O}$ values, interpreted to indicate the driest and coolest conditions. Growth rates were slow between 24 and 17 ka, with hiatuses from 17 to 16.5 ka and from 12.9 to 9.9 ka, but the fastest growth occurred between 16.4 and 13.0 ka. This growth pattern is similar to CWN-4 (Fig. 11A), which has comparable hiatuses during HS1 (17.32–15.47 ka) and YD (12.38–9.90 ka) and fastest growth rates in the intermediate time interval (late HS1 through BA). There is little paleoclimate variation in Cuba when many other circum-GoM records show prompt climate shifts, such as across the HS1 through BA transition. Cuban precipitation over this time may have followed from a weakened northern branch of the Caribbean Low-Level Jet while the ITCZ shifted south, but the increase in growth rates between HS1 and YD stadials could be consistent with an increase in precipitation.

Central Florida. Lake sediment (Grimm et al., 2006; Arnold et al., 2018) and speleothem (van Beynen et al., 2017) reconstructions indicate warmer and wetter conditions in Florida during cold North Atlantic stadials (HS1, YD). The transition from HS1 to the BA is only sampled in the Lake Tulane pollen record (Fig. 11G). The transition to the BA in this record coincides with pollen shifts that indicate a change from warm and wet conditions during HS1 and to colder and drier conditions during the BA. The opposing polarity of these climate states compared to other circum-GoM records may be attributable to an abundance of heat in waters flanking Florida as Loop Current and Gulf Stream heat transport decreased during cold North Atlantic stadials with slowdowns in AMOC (Grimm et al., 2006).

5.8. Central Texas hydroclimate variation over the HS1-BA transition

The comparison of the HBO in CWN to other highly resolved deglacial records demonstrates that it coincided with 1) the strongest episode of LIS MW input to the GoM, namely MWF-3 of Aharon (2003, 2006) that uniquely involved hyperpycnal flows, 2) MWP-1a, as recognized in different ocean basins, and 3) strong shifts in precipitation patterns in subtropical North Atlantic and Indo-Asian records influenced by latitudinal migrations of the ITCZ and associated wind and pressure systems (Table 2, Fig. 10G-L). The 213 year duration of the HBO in CWN is remarkably similar to

comparable HS1-BA excursions in the Cariaco Basin (200 yr), best constrained East Asian Monsoon stalagmite records in Hulu (~195 yr) and Dongge (~189 yr) caves, and the INTIMATE Greenland ice core composite (210 yr). Individual Greenland ice core records indicate that the period of most rapid change had shorter durations of ~39–53 years, which is also similar to the fastest rate of change within the Cariaco Basin HS1-BA sediment reflectance record (56 yr). The ~200 year duration of the HBO in CWN and other records is also similar to the ~100–200 year transit time for deep water in the Atlantic Basin (Broecker, 1979; Broecker, 1998; McManus et al., 2004). The interval from 14.75–14.55 ka was clearly a dynamic episode that rapidly and significantly affected Northern Hemisphere climate regimes, while also contributing 14–18 m of sea level rise (Deschamps et al., 2012). The further broad synchronicity of dry-wet climate trends across the HS1-BA transition between CWN-4 and many other circum-GoM records (Fig. 11B–E) demonstrates that the regional hydroclimate shift across the HS1-BA transition was not limited to central Texas.

Recognizing this broad coincidence in Northern Hemisphere climate change, and the similarity between CWN-4 $\delta^{18}\text{O}$ and other deglacial climate records that were affected by changing North Atlantic conditions, it is worth considering how hydroclimate in central Texas may have changed across the HS1-BA transition. The HS1-BA transition study interval in CWN-4 shows a clear, marked slowdown in growth rate coincident with the HBO (20–15 $\mu\text{m}/\text{yr}$), and then a rapid six-fold increase (89 $\mu\text{m}/\text{yr}$) immediately following this excursion. From our inference that growth rate followed effective precipitation, advection of GoM moisture to central Texas was substantially limited during the HBO, and then greatly increased. The density of U-series dates is sufficient to identify two previous slow-fast growth intervals beginning above a hiatus that occurred from 17.32–15.42 ka: 1) a fast growth episode with growth rates in excess of 80 $\mu\text{m}/\text{yr}$ between 15.42 and 15.30 ka, and 2) a second episode between 14.91 and 14.80 ka with growth rates of 37 $\mu\text{m}/\text{yr}$ (Fig. 2B). It is notable that slow growth episodes preceding these initial fast growth intervals coincide with Heinrich events H1.1 (~16.2 ka) and H1.2 (~15.1 ka), recognized as times of meltwater input to the north Atlantic (Fig. 10F). These alternations between slow and fast growth indicate that moisture delivery to central Texas was episodic during the early deglacial. There is some correspondence between slow growth in CWN-4 following decreases in $\delta^{18}\text{O}$, that could indicate an association between LIS MW input to the GoM and suppressed moisture advection. In any scenario, the HBO by far involved the greatest single decrease in $\delta^{18}\text{O}$, consistent with it reflecting the largest deglacial meltwater flood episode.

The predominant moisture source for central Texas and North America are warm waters of the GoM, Caribbean Sea, and tropical North Atlantic, which collectively define the North Atlantic Warm Pool (NAWP) (Wang and Enfield, 2001). Atmospheric circulation dictating moisture transfer from the NAWP depends on the respective positions of the Jet Stream, the North Atlantic Subtropical High (NASH) pressure cell (aka, Bermuda High, Azores High), which corresponds to the descending limb of the Hadley cell, and the ITCZ (Forman et al., 1995; Liu and Fearn, 2000; Knox, 2000) (Fig. 12). These highs and the ITCZ all shift latitudinally with seasonal changes in Northern Hemisphere insolation and SST (Lechleitner et al., 2017; Wang and Fiedler, 2006; Wang and Fu, 2007). During boreal winter, when the ITCZ is furthest south, warm tropical waters are limited to the southeastern GoM, whereas in boreal summer, when the ITCZ is furthest north (~15°, Hodell et al., 2008), the AWP reaches its northern and western extent (Wang et al., 2001; Wang and Enfield, 2001; Poore et al., 2004; Nürnberg et al., 2008; Ziegler et al., 2008). Because moisture tends to move clockwise around high pressure systems in the Northern

Hemisphere, the transfer of moisture in the circum-GoM region often occurs as Low Level Jet (LLJ) systems (e.g., Caribbean Low Level Jet, Southern Great Plains Low Level Jet) that develop along the western ridge of the NASH. These LLJ systems can have southern branches that transport moisture inland to central America, Mexico and western North America as part of the North American Monsoon system, and northern branches that route moisture directly into the southern US. Heating of the elevated Rocky Mountains forms a summertime low pressure system and the region between the Rockies and NASH define a pressure gradient that also influences the trajectories of LLJ systems. The meridional position of northward moisture flow associated with LLJ systems thus depends on the size and location of the NASH with respect to the Jet Stream and ITCZ, which during the deglacial were likely governed by high- and low-latitude forcing; in addition to the presence of the LIS (Montero-Serrano et al., 2011). Periods of rapid CWN-4 growth may have followed deglacial intervals when the size and positions of the NAWP and NASH established enduring LLJ systems that routed moisture conditioned from the warm Caribbean and GoM surface waters into central Texas (e.g., Forman et al., 1995).

Tropical atmospheric circulation is sensitive to AMOC variability and to sea ice extent (Chiang and Bitz, 2005; Hughen et al., 1996; Peterson et al., 2000; Ziegler et al., 2008). When AMOC is weak and sea ice extends south, the ITCZ shifts south. When AMOC is active and sea ice extent retreats, the ITCZ shifts north. Cold stadials had larger thermal gradients that enhanced trade winds and seasonality, whereas warm interstadials had reduced thermal gradients and seasonality (Hughen et al., 1996, 1998; Cheng et al., 2012). The entire Hadley circulation cells and jet streams shifted south (cold stadials) and north (warm interstadials) with these respective changes in AMOC state, which in turn influenced the location and size of high pressure zones associated with sinking air (dry conditions) and peripheral low pressure systems associated with rising air (that can bring wet conditions at inversions with dry air masses). During the last deglaciation, these variations extended to subtropical and mid-latitudes and were synchronous within U-series age precision (Oster and Kelley, 2016). Many circum-GoM records, including CWN-4, demonstrate drier conditions with reduced runoff or slow downs/hiatuses in speleothem records during HS1 and YD stadials associated with cold North Atlantic climate states. These records indicate changes in atmospheric circulation and reduced atmospheric moisture associated with sluggish or stopped AMOC. Many of the same records, including CWN-4, show evidence of a shift to wetter conditions and faster speleothem growth during the BA, when AMOC intensity resumed. As a potential modern analog, Li et al. (2011) demonstrated that the western ridge of NASH has shifted westward by ~6° over recent decades (1948–2007) in response to warming North Atlantic SST, which has changed summer precipitation across the southeast US. The NASH system is expected to intensify, expand and move further west with increasing atmospheric CO₂ levels and warming North Atlantic SST. Generally similar variations in the NASH system may have occurred across the HS1-BA transition in the circum GoM region, when AMOC vigorously resumed at the beginning of the Bølling warming and the ITCZ shifted northward. These records can be reconciled by a scenario involving greatly enhanced moisture transfer to central Texas following the HBO in response to warming GoM SST and enhanced activity of LLJ systems established along the western ridge of NASH. Some of the anomalous circum-GoM records may be explained by proximity to high pressure or major heat-transporting ocean currents. For example, the inferred reduced overall precipitation amounts spanning HS1-BA-YD time for W. Cuba (Warken et al., 2019) could be explained by the dominance of high pressure limiting LLJ moisture transport, perhaps related to NASH proximity.

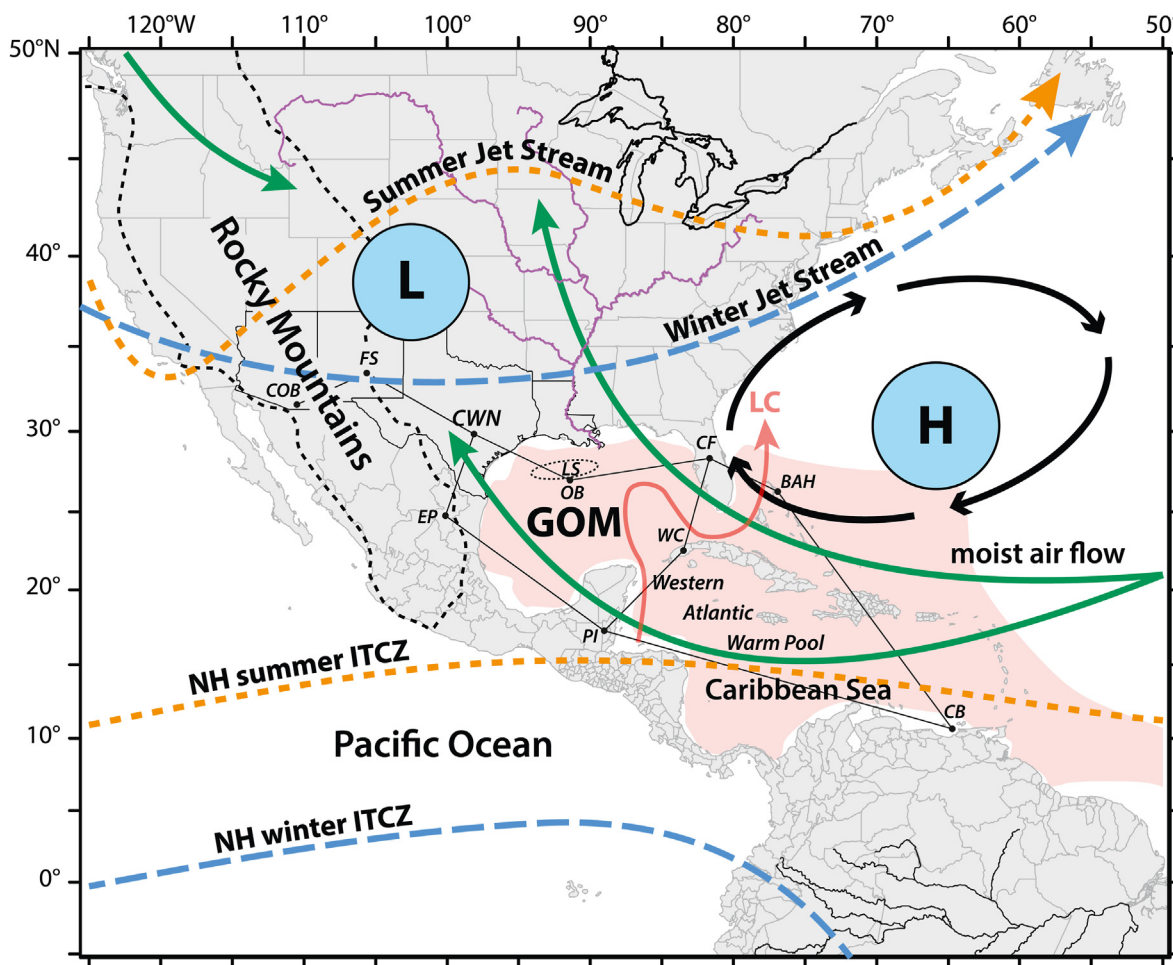


Fig. 12. Factors regulating tropical moisture transport to central Texas and the southern US. A pressure gradient forms during warm months between a low-pressure cell associated with the Rocky Mountains and a high-pressure cell formed in the North Atlantic Ocean as a portion of the descending Hadley cell, known as the Bermuda High or North Atlantic Subtropical High (NASH). The summer jet stream wobbles latitudinally and the intertropical convergence zone (ITCZ) migrates ~10° further north than its winter latitude. With increasing summer insolation, waters of the western Atlantic, Caribbean Sea and Gulf of Mexico warm anomalously to form the Western Atlantic Warm Pool (light red shaded area). Moisture-rich low level jet systems (green arrows) are routed northward into the southern US and Mexico by cyclonic movement around the western ridge of the NASH cell. North Atlantic thermohaline circulation involves surface flow through the Gulf of Mexico via the dynamic (eddy shedding) Loop Current (LC). Mississippi River system is shown in purple. Fine black lines connect deglacial localities compared with the CWN-4 record (cf. Fig. 9), including speleothems from COB - Cave of the Bells, AZ; FS - Fort Stanton Cave, NM; WC - W. Cuba; and BAH - Bahamas; terrestrial basin/lakes from EP - El Potosi Basin, N. Mex; PI - Lake Peten Itza, Guatemala; and CF - Central Florida; marine sediment cores from LS - Louisiana Slope and OB - Orca Basin, N. Gulf of Mexico; CB - Cariaco Basin, and offshore N. Venezuela. Figure modified after [Montero-Serrano et al. \(2011\)](#) and references therein. (For interpretation of the references to color in this figure legend, the reader is referred to the Web version of this article.)

5.8.1. Why was moisture amount limited during the HBO?

The considerable hiatuses accompanying HS1 and the YD in the CWN-4 record demonstrate that advection of GoM moisture to central Texas was limited during cold stadials (Fig. 10F). These were times when AMOC was sluggish and the ITCZ was shifted south. The BA onset is thought to correspond with rapid North Atlantic warming associated with a vigorous resumption of AMOC (McManus et al., 2004), and a northward shift in the ITCZ and associated Hadley circulation. The temperature increase across the HS1-BA boundary in Greenland ice cores (GS-2.1a to GI-1e) at 14,642 BP, with a 186 year maximum counting error (Rasmussen et al., 2014), is consistent with the HBO in CWN-4 between 14.75 ± 0.08 ka and 14.54 ± 0.08 ka, within the uncertainties of age determinations (Table 2). Given the combined age uncertainties, the HBO could also have predated the onset of the BA (GI-1e), allowing for exploration to two scenarios bearing on central Texas deglacial hydroclimate: 1) If the HBO predated the onset of the BA (GI-1e), then the slow growth conditions in CWN-4 during the HBO could correspond with the last gasp of cold North Atlantic climate

conditions, and their associated ocean-atmosphere teleconnections in central Texas. This scenario would be consistent with cold, arid conditions during HS1 and the YD in CWN-4 and other northern hemisphere terrestrial localities influenced by AMOC stagnation. 2) However, if the HBO coincides with the onset of the BA (GI-1e), then slow growth conditions in CWN-4 occurred at the same time that AMOC reinvigorated and Greenland warmed. In this case the reorganization of ocean/atmosphere teleconnections is expected to shift toward increased precipitation and faster speleothem growth rates – so the slowdown during the HBO is perplexing, and requires an alternative scenario.

Regardless of timing, the CWN-4 δ¹⁸O record demonstrates that the HBO coincided with the tremendous addition of LIS MW, most likely as MWF-3 (Aharon, 2006) and MWP-1a (Deschamps et al., 2012). Indeed, a significant contribution of LIS MW to sites of NADW formation, via the GoM, Loop Current, and Gulf Stream, has previously been considered in relation to AMOC reduction and cold north Atlantic conditions (Flower et al., 2004; Stanford et al., 2006; Roche et al., 2007; Erlingsson, 2008; Gregoire et al., 2012). Such

additions would seem to require extensive and progressive LIS melting, but other more rapid scenarios have been considered. Erlingsson (2008), for example, postulated that a sub-glacial outburst flood may have discharged into the GoM, coincident with MWP-1a, and stimulated the Gulf Stream to reinvigorate AMOC and trigger the Bølling warming phase. Gregoire et al. (2012) suggested that MW outflows related to rapid melting of the saddle between the Laurentide and Cordilleran ice sheets, involving delivery of large amounts of MW to the GoM, could explain the rapid sea level rise during MWP-1a. As highly-resolved GoM foraminiferal $\delta^{18}\text{O}$ records during MWF-3/MWP-1a are thus far lacking, it is difficult to constrain the volume of LIS MW addition that accompanied this exceptional flood event and its potential impact on AMOC stability. However, considering the similarity between the ~200 year duration of the HBO in CWN-4 and the transit time for deep water in the north Atlantic, it is conceivable that the MWF-3 coincided with rapid resumption of AMOC and northward transfer of heat accumulated in southern hemisphere oceans during HS1, as the bipolar seesaw flipped to resume enhanced north Atlantic deep water formation (Broecker, 1998). Assessing a causal relationship between MWF-3 and the resumption of AMOC is beyond the scope of this study, but slow growth rates over the HBO demonstrate that GoM moisture advection was suppressed over a ~200 yr interval.

Considering the strong effect of SST on atmospheric moisture content, protracted cooling of GoM surface waters in response to MWF-3 might explain slow growth rates in CWN-4 during the HBO. Oglesby et al. (1989) modelled this effect using an atmospheric general circulation model, for various cooling scenarios (3°, 6°, 12 °C). The rationale for appreciable GoM SST cooling during MW flood episodes follows from arguments that: 1) modern riverine input is 5–10 °C cooler than GoM SST; 2) MW addition should further enhance cooling, considering the melting ice source, large flow volumes, relatively short travel distance (~1000 km), and limited vertical exchange with denser underlying GoM water; 3) deglacial GoM surface waters were likely cooler anyway because lower sea level would have reduced Loop Current flow through shallow (~250 m) depths of the Florida Strait and thus reduced heat exchange with GoM waters and because Caribbean surface waters feeding the Loop Current were ~2 °C cooler during the LGM; and 4) winter month insolation may have been insufficient to increase SSTs above cooling levels reached during voluminous MW input the previous summer. From the model boundary conditions, all scenarios reduced GoM SST and sharply decreased the flow of moist air advected northward, resulting in cooler and drier conditions. Thus, if MWF-3 caused exceptional cooling of GoM surface waters, the regional effect of dampened moisture transport over ~200 yrs might account for the slow growth rates in CWN-4 that accompanied the HBO. At the end of MWF-3, GoM SSTs must have increased, enhancing water vapor production. The coincidence of slow growth rates and decreasing $\delta^{18}\text{O}$ in the CWN-4 record is consistent with increasing MW input to the GoM during this SST cooling period.

The temperature-sensitive Mg/Ca proxy of planktonic foraminifera (Flower et al., 2004; Williams et al., 2010, 2012; Vetter et al., 2017) could conceivably corroborate significant cooling episodes associated with MW flood events. Evidence of GoM SST conditions during the HBO are unfortunately lacking because studies have only been conducted from Orca Basin cores (Fig. 10M and N), which conspicuously lack foram preservation during MWF-3/MWP-1A (Aharon, 2006). In the Mg/Ca-SST study of Flower et al. (2004) for Orca Basin core EN32-PC6, the all-year *Globigerinoides ruber* (white) species indicates a 1.5 °C decline in consecutive samples above the foram-sparse interval (~14.16–14.07 ka; Fig. 10M purple arrow). In the Mg/Ca-SST study of Williams et al. (2012) for Orca Basin core MD02-2550, the non-winter *G. ruber* (pink) species also indicates a cooling trend on the order of 2 °C in nine samples

(~14.34–14.19 ka) immediately above the foram-barren interval (Fig. 10M grey arrow); similar comparisons for the all-year *G. ruber* (white) species were not reported over the same interval. Whether or not these intervals represent a continuation or recovery from cooler SSTs during MWF-3/MWP-1a is unclear, but substantially cooler SSTs during the HBO cannot be excluded. From analysis of individual planktonic foraminifer specimens (*Obulina universa*) in the same core, Vetter et al. (2017) documented a broad range of deglacial salinities (Ba/Ca: 0.6–4.8 $\mu\text{mol/mol}$) and temperatures (10.4–27.3 °C, based on Mg/Ca) bounding the foram-barren interval between ~17.4 and ~13.4 ka.

6. Conclusions

Monitoring the CWN karst system in central Texas demonstrates that drip water and calcite $\delta^{18}\text{O}$ reflect the $\delta^{18}\text{O}$ of effective precipitation, and that calcite grows during cool seasons when the cave has low cave-air CO_2 levels. Growth lamina express alternations (couplets) in inclusion density and in confocal laser fluorescence microscopy (CLFM) imagery. Monitoring insights support the inference that inclusion-poor lamina grew during the cool season and high-fluorescence, inclusion-rich lamina grew during warm seasons. The couplets are annual based on the correspondence of the stratigraphic frequency of lamina counted in CLFM with those calculated from U-series age constraints. These seasonal fabrics are visible in CLFM, but only when using unconventionally-thick sections (150–500 μm). This method may help reveal seasonal lamina in speleothems from other localities.

Speleothem moisture source and moisture amount proxies, developed from monitoring of the modern cave system and high-resolution petrographic and $\delta^{18}\text{O}$ analysis of stalagmite CWN-4 growth fabrics, are used to reconstruct hydroclimate in central Texas and the Gulf of Mexico (GoM). Key to interpreting these hydroclimate proxies is the coupling between the GoM as the primary moisture source for central Texas, and the signal of low $\delta^{18}\text{O}$ Laurentide Ice Sheet (LIS) meltwater that changed the composition of GoM surface waters, as the transition from Heinrich Stadial 1 to the Bølling warming period (HS1-BA transition) corresponds with a rapid negative $\delta^{18}\text{O}$ excursion (–1.7‰) within CWN-4 (abbreviated as the HBO episode). Growth rates were slow (~15–20 $\mu\text{m/yr}$) during the HBO, then increased six-fold (~90 $\mu\text{m/yr}$). The dominant hydroclimate response in central Texas to the most significant natural warming event of the last deglacial, the HS1-BA transition, was a pronounced increase in regional rainfall.

The CWN-4 $\delta^{18}\text{O}$ time series constrains the HBO to a duration of ~210 years, between 14.75 ± 0.08 and 14.54 ± 0.08 ka. Within the age uncertainties, the HBO episode in Texas coincides with the onset of Bølling warming in Greenland ice core temperature records, the resumption of AMOC, Meltwater Pulse 1a (MWP-1a) and Meltwater Flood 3 (MWF-3) in the GoM, among other northern Hemisphere climate records. The coincidence of the HBO with MWP-1a and MWF-3 corroborates that the most significant episode of LIS meltwater input to the GoM was contemporary with MWP-1a. As MWF-3 uniquely involved hyperpycnal flows (Aharon, 2006) and foraminifera are sparse or barren in this interval of Orca Basin (GoM) cores (Vetter et al., 2017), the impact of MWF-3 on GoM hydrography may not be fully appreciated. CWN-4 $\delta^{18}\text{O}$ time series support that meltwater delivery to the GoM during MWF-3 (and MWP-1a) was continuous.

We infer that deglacial hydroclimate in central Texas largely followed changes in AMOC, with a linkage of LIS meltwater input to the GoM. In this scenario, slow growth intervals in CWN-4 corresponded with cold North Atlantic episodes and fast growth followed warm North Atlantic episodes, with the possible exception of the HBO. The impact of AMOC variations in this region was to

change the interplay of factors affecting atmospheric moisture content and circulation, likely related to alternation in interactions between the North Atlantic Warm Pool and North Atlantic Sub-tropical High that governed the meridional position of north-directed low level jet systems. For the HBO, in particular, slow growth rates during MWF-3 could have been related to protracted cooling of GoM surface waters and reduction in atmospheric moisture. The common timing and duration of the HBO with shifts toward wetter conditions in many Northern Hemisphere climate records suggests common ocean-atmosphere teleconnections related to AMOC intensity. Based on these connections, we speculate that changes in GoM surface water $\delta^{18}\text{O}$ and growth rate recorded in speleothems could proxy AMOC variations. This hypothesis may be tested by reconstructing new deglacial growth rates and $\delta^{18}\text{O}$ records in speleothems from regions like the Edwards Plateau, where 1) effective precipitation is predominantly sourced from the GoM, and 2) the warm, semi-arid climate makes the region's climate sensitive to small changes in effective precipitation (Koster et al., 2004). Recognition that central Texas ventilation-style caves encode growth fabric seasonality will advance studies of regional impacts of abrupt global change events.

Credit author statement

Nathan Miller: Conceptualization, Methodology, data collection, analysis, Writing – original draft, Visualization, Supervision; Jay Banner: Conceptualization, Methodology, data collection, writing, Resources; Weimin Feng: Formal analysis, Investigation; Angelique Gonzales: Investigation; Reinhard Kozdon: SIMS analysis, Investigation. All authors reviewed and edited the manuscript.

Declaration of competing interest

The authors declare that they have no known competing financial interests or personal relationships that could have appeared to influence the work reported in this paper.

Acknowledgements

We thank Eric James for valuable input regarding speleothem growth rate as a moisture proxy; Jesse Nusbaumer and Corinne Wong for assistance quantifying central Texas moisture sources; Yua Li of Dell Children's Pediatric Research Center for assistance with CLFM imagery acquisition and processing; Darrel Tremaine for thoughtful input; and Kara Passo, Lakin Beal, Kendra Bunnell, Peter Carlson, Rachel Wright and other Banner Group lab members who aided with CWN monitoring efforts. We thank the owners, management and staff of CWN for assistance with field logistics and access. Marcy Davis (JSG-UTIG) is thanked for assistance with GIS mapping. John Valley assisted with SIMS analysis at the University of Wisconsin-Madison. This work was supported by the Geology Foundation of UT Austin, F.M. Bullard Professorship to JB, and the PaleoTexas project of Planet Texas 2050. We acknowledge support from the NSF Coupled Natural and Human Systems Program (1518541). WiscSIMS is supported by NSF (EAR = 1658823, –200 4618) and the University of Wisconsin.

Appendix A. Supplementary data

Supplementary data to this article can be found online at <https://doi.org/10.1016/j.quascirev.2021.107244>.

References

- Aharon, P., 2003. Meltwater flooding events in the Gulf of Mexico revisited: implications for rapid climate changes during the last deglaciation. *Paleoceanography* 18 (4), 1079. <https://doi.org/10.1029/2002PA000840>.
- Aharon, P., 2006. Entrainment of meltwaters in hyperpycnal flows during deglaciation superstorms in the Gulf of Mexico. *Earth Planet Sci. Lett.* 241, 260–270.
- Arienzo, M.M., Swart, P.K., Pourmand, A., Broad, K., Clement, A.C., Murphy, L.N., Vonhof, H.B., Kakuk, B., 2015. Bahamas speleothem reveals climate variability associated with Heinrich events. *Earth Planet Sci. Lett.* 430, 377–386.
- Arienzo, M.M., Swart, P.K., Pourmand, A., Broad, K., Clement, A.C., Pourmand, A., Kakuk, B., 2017. Multi-proxy evidence of millennial climate variability from multiple Bahamian speleothems. *Quat. Sci. Rev.* 161, 18–29.
- Arnold, T.E., Diefendorf, A.F., Brenner, M., Freeman, K.H., Baczynski, A.A., 2018. Climate response of the Florida peninsula to heinrich events in the north Atlantic. *Quat. Sci. Rev.* 194, 1–11.
- Asmerom, A., Polyak, V.J., Rasmussen, J.B.T., Burns, S.J., 2010. Variable winter moisture in the southwestern United States linked to rapid glacialclimate shifts. *Nat. Geosci.* 3, 114–117.
- Asmerom, A., Polyak, V.J., Rasmussen, J.B.T., Burns, S.J., Lachniet, M., 2013. Multi-decadal to multicentury scale collapses of Northern Hemisphere monsoons over the past millennium. *Proc. Natl. Acad. Sci. Unit. States Am.* 110, 9651–9656.
- Asmerom, Y., Polyak, V., Burns, S., Rasmussen, J., 2007. Solar forcing of Holocene climate: new insights from a speleothem record, southwestern United States. *Geology* 35, 1–4.
- Baker, A., Hartmann, A., Duan, W., et al., 2019. Global analysis reveals climatic controls on the oxygen isotope composition of cave drip water. *Nat. Commun.* 10, 2984. <https://doi.org/10.1038/s41467-019-11027-w>.
- Baker, A., Hellstrom, J., Hellstrom, J.C., Kelly, B.F.J., Mariethoz, G., Trouet, V., 2015. A composite annual-resolution stalagmite record of North Atlantic climate over the last three millennia. *Sci. Rep.* 5, 10307. <https://doi.org/10.1038/srep10307>, 2015.
- Baker, A.J., Matthey, D.P., Baldini, J.U.L., 2014. Reconstructing modern stalagmite growth from cave monitoring, local meteorology and experimental measurements of dripwater films. *Earth Planet Sci. Lett.* 392, 239–249.
- Baker, A., Smart, P.L., 1995. Recent flowstone growth rates: field measurements in comparison to theoretical predictions. *Chem. Geol.* 122, 121–128.
- Baker, A., Smart, P.L., Edwards, R.L., Richards, D.A., 1993. Annual growth banding in a cave stalagmite. *Nature* 364, 518–520.
- Baker, A., Smith, C.L., Jex, C., Fairchild, I.J., Genty, D., Fuller, L., 2008. Annually laminated speleothems: a review. *Int. J. Speleol.* 37, 193–206.
- Baldini, J.U.L., 2010. Cave atmosphere controls on stalagmite growth rate and palaeoclimate records. In: London, Geol Soc (Ed.), *Spec. Publ.* 336, 283–294.
- Banner, J.L., Guilfoyle, A., James, E., Stern, L.A., Musgrove, M., 2007. Seasonal variations in modern speleothem calcite growth in Central Texas, U.S.A. *J. Sediment. Res.* 77, 615–622.
- Bard, E., Hamelin, B., Fairbanks, R.G., 1990. U-Th ages obtained by mass spectrometry in corals from Barbados: sea level during the past 130,000 years. *Nature* 346, 456–458.
- Bassett, S.E., Milne, G.A., Bentley, M.J., Huybrechts, P., 2007. Modelling Antarctic sea-level data to explore the possibility of a dominant Antarctic contribution to meltwater pulse 1A. *Quat. Sci. Rev.* 26, 2113–2127.
- Billir, N., 2012. Evidence for Meltwater Pulse 1a in the Gulf of Mexico Based on Radiogenic Isotopes of Leachates. University of Florida at Gainesville Undergraduate Honors thesis, p. 39p.
- Bomar, G.W., 1995. *Texas Weather*. University of Texas Press, Austin, p. 265.
- Braithwaite, C.J.R., 1979. Crystal textures of recent fluvial pisolites and laminated crystalline crusts in Dyfed, South Wales. *J. Sediment. Petrol.* 49, 181–194.
- Broecker, W.S., Kennett, J.P., Flower, B.P., Teller, J.T., Trumbore, S., Bonani, G., Wolffli, W., 1989. Routing of meltwater from the Laurentide Ice Sheet during the Younger Dryas cold episode. *Nature* 341, 318–321.
- Broecker, W.S., 1979. A revised estimate of the radiocarbon age of the North Atlantic DeepWater. *J. Geophys. Res.* 84, 3218–3226.
- Broecker, W.S., 1998. Paleocirculation during the last deglaciation: A bipolar seesaw? *Paleoceanography* 13, 119–121.
- Buizert, C., Gkinis, V., Severinghaus, J.P., He, F., Lecavalier, B.S., Kindler, P., et al., 2014. Greenland temperature response to climate forcing during the last deglaciation. *Science* 345 (6201), 1177–1180. <https://doi.org/10.1126/science.1254961>.
- Bunnell, K., 2019. The Response of Central Texas Cave Drip Sites to Extreme Events: Implications for Paleoclimatology. University of Texas, Austin, p. 233 [MSc thesis].
- Burke, K.D., Williams, J.W., Chandler, M.A., Haywood, A.M., Lunt, D.J., Otto-Bliesner, B.L., 2018. Pliocene and Eocene provide best analogs for near-future climates. *Proceedings of the National Academy of Sciences, USA* 115, 13288–13293, 2018.
- Carlson, A.E., 2009. Geochemical constraints on the Laurentide Ice Sheet contribution to Meltwater Pulse 1A. *Quat. Sci. Rev.* 28, 1625–1630.
- Carlson, P.E., Miller, N.R., Banner, J.L., Breecker, D.O., Johnson, K., 2018. The potential of near-entrance stalagmites as high-resolution terrestrial paleoclimate

- proxies: Application of isotope and trace-element geochemistry to seasonally-resolved chronology. *Geochem. Cosmochim. Acta* 235, 55–75.
- Casteel, R.C., Banner, J.L., 2015. Temperature-driven seasonal calcite growth and drip water trace element variations in a well-ventilated Texas cave: implications for speleothem paleoclimate studies. *Chem. Geol.* 392, 43–58.
- Cheng, H., Sinha, A., Wang, X., Cruz, F., Edwards, L., 2012. The Global Paleomonsoon as seen through speleothem records from Asia and the Americas. *Clim. Dynam.* 39, 1045–1062.
- Chiang, J.C.H., Bitz, C.M., 2005. Influence of high latitude ice cover on the marine Intertropical Convergence Zone. *Clim. Dynam.* 25, 477–496.
- Clark, P.U., McCabe, A.M., Mix, A.C., Weaver, A.J., 2004. Rapid rise of sea level 19,000 years ago and its global implications. *Science* 304, 1141–1144.
- Clark, P.U., Shakun, J.D., Baker, P.A., Bartlein, P.J., Brewer, S., Brook, E., Carson, A.E., Cheng, H., Kaufman, D.S., Liu, Z., Marchitto, T.M., Mix, A.C., Morrill, C., Otto-Bliesner, B.L., Pahnke, K., Russe, J.M., Whitlock, C., Adkins, J.F., Blois, J.L., Clark, J., Coman, S.M., Curry, W.P., Flower, B.P., He, F., Johnson, T.C., Lynch-Stieglitz, J., Markgraf, V., McManus, J., Mitrovica, J.X., Moreno, P.L., William, J.W., 2012. Global climate evolution during the last deglaciation. *Proc. Natl. Acad. Sci. U.S.A.* 109, E1134–E1142.
- Cook, B.I., Ault, R.R., Smerdon, J.E., 2015. Unprecedented 21st century drought risk in the American Southwest and Central Plains. *Sci. Adv.* 1, 2015, e1400082-e1400082.
- Coplen, T.B., 2007. Calibration of the calcite–water oxygen-isotope geothermometer at Devils Hole, Nevada, a natural laboratory. *Geochem. Cosmochim. Acta* 71, 3948–3957.
- Cowan, B., Osborne, M., Banner, J.L., 2013. Temporal variability of cave-air CO₂ in central Texas. *J. Cave Karst Stud.* 75, 38–50.
- Cutler, K.B., Edwards, R.L., Taylor, F.W., Cheng, H., Adkins, J., Gallup, C.D., Cutler, P.M., Burr, G.S., Bloom, A.L., 2003. Rapid sea-level fall and deep-ocean temperature change since the last interglacial period. *Earth Planet Sci. Lett.* 206, 253–271.
- Cvijanovic, I., Chiang, J.H., 2013. Global energy budget changes to high latitude North Atlantic cooling and the tropical ITCZ response. *Clim. Dynam.* 40, 1435–1452.
- Deininger, M., Hansen, M., Fohlmeister, J., Schröder-Ritzrau, A., Burstyn, Y., Schlz, D., 2021. Are oxygen isotope fractionation factors between calcite and water derived from speleothems systematically biased due to prior calcite precipitation (PCP)? *Geochem. Cosmochim. Acta* 305, 212–227.
- Deschamps, P., Durand, N., Bard, E., Hamelin, B., Camoin, G., Thomas, A.L., Henderson, G.M., Okuno, Y., Yokoyama, Y., 2012. Ice-sheet collapse and sea-level rise at the Bolling warming 14,600 years ago. *Nature* 483, 559–564.
- Dietzel, M., Tang, J., Leis, A., Köhler, S.J., 2009. Oxygen isotopic fractionation during inorganic calcite precipitation – effects of temperature, precipitation rate and pH. *Chem. Geol.* 208, 107–115.
- Dirmeyer, P.A., Brubaker, K.L., 2007. Characterization of the global hydrologic cycle from a back-trajectory analysis of atmospheric water vapor. *J. Hydrometeorol.* 8, 20–37.
- Dreybrodt, W., 1988. Processes in Karst Systems – Physics, Chemistry and Geology. Springer Series in Physical Environments, vol. 5. Springer, Berlin, New York, p. 288.
- Dreybrodt, W., 1999. Chemical kinetics, speleothem growth and climate. *Boreas* 28, 347–356.
- Dutton, A., Rubin, K., McLean, N., Bowring, J., Bard, R., Edwards, R.L., Henderson, G.M., Yokoyama, Y., 2017. Data reporting standards for publication of U-series data for geochronology and timescale assessment in the earth sciences. *Quat. Geochronol.* 39, 142–149.
- Dykoski, C.A., Edwards, R.L., Cheng, H., Yuan, D., Cai, Y., Zhang, M., Lin, Y., Qing, J., An, Z., Revenaugh, J., 2005. A high-resolution, absolute dated Holocene and deglacial Asian monsoon record from Dongge Cave, China. *Earth Planet Sci. Lett.* 233, 71–86.
- Edwards, R.L., Beck, J.W., Burr, G.S., Donahue, D.J., Chappell, J.M.A., Bloom, A.L., Druffel, E.R.M., Taylor, F.W., 1993. A Large Drop in Atmospheric ¹⁴C/¹²C and Reduced Melting in the Younger Dryas, Documented with ²³⁰Th Ages of Corals. *Science* 260, 962–968.
- Ellwood, B.B., Gose, W.A., 2006. Heinrich H1 and 8200 yr B.P. climate events recorded in Hall's Cave, Texas. *Geology* 34, 753–756.
- Emiliani, C., Rooth, C., Stipp, J.J., 1978. The late Wisconsin flood into the Gulf of Mexico. *Earth Planet Sci. Lett.* 41, 159–162.
- El-Shenawy, M.I., Kim, S-T., Schwarz, H.P., 2020. Carbon and oxygen isotope systematics in cave environments: Lessons from an artificial cave “McMaster Cave”. *Geochem. Cosmochim. Acta* 272, 137–159.
- Emiliani, C., Gartner, S., Lidz, B., Eldridge, K., Elvey, D.K., Huang, T.C., Stipp, J.J., Swanson, M.F., 1975. Paleoclimatological analysis of late Quaternary cores from the northeastern Gulf of Mexico. *Science* 189, 1083–1088.
- Emmerich, W.E., 2003. Carbon dioxide fluxes in a semiarid environment with high carbonate soils. *Agric. For. Meteorol.* 116, 91–102.
- Erlingsson, U., 2008. A Jökulhlaup from a Laurentide Captured Ice Shelf to the Gulf of Mexico Could Have Caused the Bolling Warming, 90A. *Geografiska Annaler*, pp. 125–140.
- Escobar, J., Hodell, D.A., Brenner, M., Curtis, J.H., Gilli, A., Mueller, A.D., Anselmetti, F.S., Ariztegui, D., Grzesik, D.A., Pérez, L., Schwalb, A., Guilderson, T.P., 2012. A w43-ka record of paleoenvironmental change in the Central American lowlands inferred from stable isotopes of lacustrine ostracods. *Quat. Sci. Rev.* 37, 92–104.
- Fairbanks, R.G., Mortlock, R.A., Chiu, T.-C., Cao, L., Kaplan, A., Guilderson, T.P., Fairbanks, T.W., Bloom, A.L., Grootes, P.M., Nadeau, M.J., 2005. Radiocarbon calibration curve spanning 0 to 50,000 years BP based on paired ²³⁰Th/²³⁴U/²³⁸U and ¹⁴C dates on pristine corals. *Quat. Sci. Rev.* 24, 1781–1796.
- Fairbanks, R.G.A., 1989. 17,000-year glacio-eustatic sea level record; influence of glacial melting rates on the Younger Dryas event and deep-ocean circulation. *Nature* 342, 637–642.
- Fairchild, I.J., Smith, C.L., Baker, A., Fuller, L., Spötl, C., 2006. Modification and preservation of environmental signals in speleothems. *Earth Sci. Rev.* 75, 105–153.
- Feng, W., Banner, J., Guilfoyle, A., Musgrove, M., James, E.W., 2012. Oxygen isotopic fractionation between drip water and speleothem calcite: A 10-year monitoring study, central Texas, USA. *Chem. Geol.* 304–305, 53–67.
- Feng, W., Casteel, R.C., Banner, J.L., Heinz Fry, A., 2014a. Oxygen isotopes of precipitation, cave drip water and speleothem calcite from a well-ventilated cave in Texas, USA: Assessing a new speleothem temperature proxy. *Geochem. Cosmochim. Acta* 127, 233–250.
- Feng, W., Hardt, B.F., Banner, J.L., Meyer, K.J., James, E.W., Musgrove, M., Edwards, R.L., Cheng, H., Min, A., 2014b. Changing amounts and sources of moisture in the U.S. southwest since the Last Glacial Maximum in response to global climate change. *Earth Planet Sci. Lett.* 401, 47–56.
- Feng, Z., et al., 2019. Spatiotemporal characteristics and large-scale environments of mesoscale convective systems east of the Rocky Mountains. *J. Clim.* 32, 7303–7328. <https://doi.org/10.1175/JCLI-D-19-0137.1>.
- Fleitmann, D., Burns, S.J., Neff, U., Mudelsee, M., Mangini, A., Matter, A., 2004. Palaeoclimatic interpretation of high-resolution oxygen isotope profiles derived from annually laminated speleothems from Southern Oman. *Quat. Sci. Rev.* 23, 935–945.
- Flower, B.P., Hastings, D.W., Hill, H.W., Quinn, T.M., 2004. Phasing of deglacial warming and Laurentide Ice Sheet meltwater in the Gulf of Mexico: *Geology* 32, 597–600.
- Flower, B.P., Williams, C., Hill, H.W., Hastings, D.W., 2011. Laurentide Ice Sheet meltwater and the Atlantic Meridional Overturning Circulation during the last glacial cycle: a view from the Gulf of Mexico. In: Rashid, H., Polyak, L., Mosley-Thompson, E. (Eds.), *Abrupt Climate Change: Mechanisms, Patterns, and Impacts*. AGU, Washington, DC, pp. 39–56.
- Forman, S.L., Oglesby, R., Markgraf, V., Stafford, T., 1995. Paleoclimatic significance of late Quaternary eolian deposition on the Piedmont and High Plains, central United States. *Global Planet. Change* 11, 35–55.
- Frisia, S., Borsato, A., Preto, N., McDermott, F., 2003. Late Holocene annual growth in three Alpine stalagmites records the influence of solar activity and the North Atlantic Oscillation on winter climate. *Earth Planet Sci. Lett.* 216, 411–424.
- Frisia, S., Borsato, A., 2010. Karst. In: Alonso-Zarza, A.M., Tanner, L.H. (Eds.), *Developments in Sedimentology, Carbonates in Continental Settings*. Elsevier, The Netherlands, pp. 269–318.
- Fritsch, J.M., Kane, R.J., Chelius, C.R., 1986. The contribution of mesoscale convective weather systems to the warm-season precipitation in the United States. *J. Clim. Appl. Meteorol.* 25, 1333–1345.
- Genty, D., Baker, A., Vokal, B., 2001. Intra- and inter-annual growth rate of modern stalagmites. *Chem. Geol.* 176, 191–212.
- Genty, D., Quinif, Y., 1996. Annually laminated sequences in the internal structure of some Belgian stalagmites – importance for paleoclimatology. *J. Sediment. Res.* 66, 275–288.
- Gimeno, L., Stohl, A., Trigo, R., 2012. Oceanic and terrestrial sources of continental precipitation. *Rev. Geophys.* 50, 1–41.
- Golledge, N.R., Menviel, L., Carter, L., Fogwill, C.J., England, M.H., Cortese, G., Levy, R.H., 2014. Antarctic contribution to meltwater pulse 1A from reduced Southern Ocean overturning. *Nat. Commun.* 5, 5107. <https://doi.org/10.1038/ncomms6107>.
- Gornitz, V., 2012. The Great Ice Melt-down and Rising Seas: Lessons for Tomorrow, Science Briefs. NASA Goddard Institute for Space Studies. www.giss.nasa.gov/research/briefs/gornitz_10/.
- Gregoire, L.J., Payne, A.J., Valdes, P.J., 2012. Deglacial rapid sea level rises caused by ice-sheet saddle collapses. *Nature* 487, 219–222.
- Grimm, E.C., Watts, W.A., Jacobson Jr., G.L., Hansen, B.C.S., Almqvist, H.R., Dieffenbacher-Krall, A.C., 2006. Evidence for warm wet Heinrich events in Florida. *Quat. Sci. Rev.* 25, 2197–2211.
- Guilfoyle, A.L., 2006. Temporal and Spatial Controls on Cave Water and Speleothem Calcite Isotopic and Elemental Chemistry. Austin, University of Texas, p. 337 central Texas [M.S. Thesis].
- Gulf of Mexico Data Atlas, 2021. National Oceanic and Atmospheric Administration. National Centers for Environmental Information. <https://gulfatlas.noaa.gov/>.
- Hanebuth, T., Stattegger, K., Grootes, P.M., 2000. Rapid flooding of the Sunda Shelf: a late-glacial sea-level record. *Science* 288, 1033–1035.
- Higgins, R.W., Yao, Y., Yarosh, E.S., Janowiak, J.E., Mo, K., 1997. Influence of the Great Plains low-level jet on summer-time precipitation and moisture transport over the central United States. *J. Clim.* 10, 481–507.
- Hodell, D.A., Anselmetti, F.S., Ariztegui, D., Brenner, M., Curtis, J.H., Gilli, A., Grzesik, D.A., Guilderson, T.J., Müller, A.D., Bush, M.B., Correa-Metrio, A., Escobar, J., Kutterolf, S., 2008. An 85-ka record of climate change in lowland central America. *Quat. Sci. Rev.* 27, 1152–1165.
- Hodell, D.A., Nicholl, J.A., Bontognali, T.R.R., Danino, S.,adorador, J., Dowdeswell, J.A., Einsle, J., Kuhlmann, H., Martrat, B., Mlencek-Vautraviers, M.J., Rodríguez-Tovar, F.J., Röhl, U., 2017. Anatomy of Heinrich Layer 1 and its role in the last deglaciation. *Paleoceanography* 32, 284–303. <https://doi.org/10.1002/2016PA003028>.
- Holliday, V.T., 2000. Folsom drought and episodic drying on the Southern High

- Plains from 10,900–10,200 ^{14}C yr B.P. *Quat. Res.* 53, 1–12.
- Holmgren, K., Karlén, W., Lauritzen, S.E., Lee-Thorp, J.A., Partridge, T.C., Piketh, S., Repinski, P., Stevenson, C., Svanered, O., Tyson, P.D., 1999. A 3000-year high-resolution record of paleoclimate for north-eastern South Africa. *Holocene* 9, 295–309.
- Hu, J., Dee, S.G., Wong, C.I., Harman, C.J., Banner, J.L., Bunnell, K.E., 2021. Assessing proxy system models of cave dripwater $\delta^{18}\text{O}$ variability. *Quat. Sci. Rev.* 254. <https://doi.org/10.1016/j.quascirev.2021.106799>.
- Hughen, K.A., Overpeck, J.T., Peterson, L.C., Trumbore, S., 1996. Rapid climate changes in the tropical Atlantic region during the last deglaciation. *Nature* 380, 51–54.
- Hughen, K., Overpeck, J., Lehman, S., et al., 1998. Deglacial changes in ocean circulation from an extended radiocarbon calibration. *Nature* 391, 65–68. <https://doi.org/10.1038/34150>.
- Hughen, K.A., Southon, J.R., Lehman, S.J., Overpeck, J.T., 2000. Synchronous radiocarbon and climate shifts during the Last Deglaciation. *Science* 290, 1951–1954.
- Ivanovic, R.F., Gregoire, J.J., Kageyama, M., Roche, D.M., Valdes, P.J., Burke, A., Drummond, R., Peltier, W.R., Tarasov, L., 2016. Transient climate simulations of the deglaciation 21–9 thousand years before present (version 1) – MIP4 Core experiment design and boundary conditions. *Geosci. Model Dev. (GMD)* 9, 2563–2587.
- Ivanovic, R.F., Gregoire, L.J., Wickert, A.D., Valdes, P.J., Burke, A., 2017. Collapse of the North American ice saddle 14,500 years ago caused widespread cooling and reduced ocean overturning circulation. *Geophys. Res. Lett.* 44, 383–394. <https://doi.org/10.1002/2016GL071849>.
- James, E.W., Banner, J.L., Hardt, B., 2015. A global model for cave ventilation and seasonal bias in speleothem paleoclimate records: A global model for cave ventilation. *G-cubed* 16, 1044–1051.
- Karpuz, N.K., Jansen, E., 1992. A high-resolution diatom record of the last deglaciation from the SE Norwegian Sea: documentation of rapid climate changes. *Paleoceanography* 7, 499–520.
- Kendall, A.C., Broughton, P.L., 1978. Origin of fabric in speleothems of columnar calcite crystals. *J. Sediment. Petrol.* 48, 550–552.
- Kennett, J.P., Shackleton, N.J., 1975. Laurentide ice sheet meltwater recorded in Gulf of Mexico deep-sea cores. *Science* 188, 147–150.
- Kienast, M., Hanebuth, T.J.J., Pelejero, C., Steinke, S., 2003. Synchronicity of meltwater pulse 1a and the Bølling warming: New evidence from the South China Sea. *Geology* 31, 67–70.
- Knox, J.C., 2000. Sensitivity of Modern and Holocene floods to climate change. *Quat. Sci. Rev.* 19, 439–457.
- Koster, R.D., Dirmeyer, P., Guo, Z., Bonan, G., 2004. Regions of strong coupling between soil moisture and precipitation. *Science* 305, 1138–1140.
- Lachniet, M.S., 2009. Climatic and environmental controls on speleothem oxygen-isotope values. *Quat. Sci. Rev.* 28, 412–432.
- Lambeck, K., Rouby, H., Purcell, A., et al., 2014. Sea level and global ice volumes from the last Glacial maximum to the Holocene. *Proc. Natl. Acad. Sci. Unit. States Am.* 111, 15296–15303.
- Lauritzen, S.E., 1995. High-Resolution Paleotemperature Proxy Record for the Last Interglaciation Based on Norwegian Speleothems. *Quat. Res.* 43, 133–146.
- Lechleitner, F.A., Breitenbach, S.F., Rehfeld, K., Ridley, H.E., Asmerom, Y., Pruffer, K.M., Marwan, N., Goswami, N., Kennett, D.J., Aquino, V.V., et al., 2017. Tropical rainfall over the last two millennia: evidence for a low-latitude hydrologic seesaw. *Sci. Rep.* 7, 45809.
- Leventer, A., Williams, D.F., Kennett, J.P., 1982. Dynamics of the Laurentide ice sheet during the last deglaciation: Evidence from the Gulf of Mexico. *Earth Planet Sci. Lett.* 59, 11–17.
- Li, W., Fu, R., Deng, Y., Wang, H., 2011. Changes to the North Atlantic Sub-tropical High and its Role in the Intensification of Summer Rainfall Variability in the Southeastern United States. *J. Clim.* 24, 1499–1506.
- Licciardi, J.M., Teller, J.T., Clark, P.U., 1999. Freshwater routing by the Laurentide ice sheet during the last deglaciation. In: Clark, P.U., Webb, R.S., Keigwin, L.D. (Eds.), *Mechanisms of Global Climate Change at Millennial Time Scales*. *Geophysical Monthly Series*, No. 112. American Geophysical Union, pp. 177–201.
- Licht, K.J., 2004. The Ross Sea's contribution to eustatic sea level during meltwater pulse 1A. *Sediment. Geol.* 165, 343–353.
- Lin, Y., Hibbert, F.D., Whitehouse, P.L., Woodroffe, S.A., Purcell, A., Shennan, I., Bradely, S.L., 2021. A reconciled solution of Meltwater Pulse 1A sources using sea-level fingerprinting. *Nat. Commun.* 12. <https://doi.org/10.1038/s41467-021-21990-y>.
- Liu, K.B., Fearn, M., 2000. Reconstruction of prehistoric landfall frequencies of catastrophic hurricanes in Northwestern Florida from lake sediment records. *Quat. Res.* 54, 238–245.
- Liu, J.P., Milliman, J.D., 2004. Reconsidering melt-water Pulses 1A and 1B: global impacts of rapid sea-level rise. *J. Ocean Univ. China* 3, 183–190.
- Liu, Z., Otto-Bliesner, B.L., He, F., Brady, E., Tomas, R., Clark, P.U., Carlson, A.E., Lynch-Stieglitz, J., Curry, W., Brook, E., Erickson, D., Jacob, R., Kutzbach, J., Cheng, J., 2009. Transient simulation of last deglaciation with a new mechanism for Bølling-Allerød warming. *Science* 325, 310–314.
- Mackintosh, A.N., Verleyen, E., O'Brien, P.E., White, D.A., Jones, R.S., McKay, R., Dunbar, R., Gore, D.B., Fink, D., Post, A.L., Miura, H., Leventer, A., Goodwin, I., Hodgson, D.A., Lilly, K., Crosta, X., Gollledge, N.R., Wagner, B., Berg, S., van Ommen, T., Zwart, D., Roberts, S.J., Vyverman, W., Masse, G., 2014. Retreat history of the East Antarctic Ice Sheet since the Last Glacial Maximum. *Quat. Sci. Rev.* 100, 10–30.
- Marchitto, T.M., Wei, K.-Y., 1995. History of Laurentide meltwater flow to the Gulf of Mexico during the last deglaciation, as revealed by reworked calcareous nanofossils. *Geology* 23, 779–782.
- Mariethoz, G., Kelley, B.F.J., Baker, A., 2012. Quantifying the value of laminated stalagmites for paleoclimate reconstructions. *Geophys. Res. Lett.* 39, L05407. <https://doi.org/10.1029/2012GL050986>.
- Markel, B.R., Steig, E.J., Buizert, C., Schoenemann, S.W., Bitz, C.M., Fudge, T.J., Pedro, J.B., Diong, Q., Jones, T.R., White, J.W.C., Sowers, T., 2016. Global atmospheric teleconnections during Dansgaard–Oeschger events. *Nat. Geosci.* 10, 36–40.
- Masson-Delmotte, V., Schulz, M., Abe-Ouchi, A., Beer, J., Ganopolski, A., González Rouco, J.F., Jansen, E., Lambeck, K., Luterbacher, J., Naish, T., Osborn, T., Otto-Bliesner, B., Quinn, T., Ramesh, R., Rojas, M., Shao, X., Timmermann, A., 2013. Information from Paleoclimate Archives. In: Stocker, T.F., Qin, D., Plattner, G.-K., Tignor, M., Allen, S.K., Boschung, J., Nauels, A., Xia, Y., Bex, V., Midgley, P.M. (Eds.), *Climate Change 2013: The Physical Science Basis*. Contribution of Working Group I to the Fifth Assessment Report of the Intergovernmental Panel on Climate Change. Cambridge University Press, Cambridge, United Kingdom and New York, NY, USA.
- Maupin, C.R., Roark, N.B., Thirumalai, K., et al., 2021. Abrupt Southern Great Plains thunderstorm shifts linked to glacial climate variability. *Nat. Geosci.* 14, 396–401. <https://doi.org/10.1038/s41561-021-00729-1>.
- McManus, J.F., Francois, R., Gherardi, J.-M., Keigwin, L.D., Brown-Leger, S., 2004. Collapse and rapid resumption of Atlantic meridional circulation linked to deglacial climate changes. *Nature* 428, 834–837.
- Meckler, A.N., Schubert, C.J., Hochuli, P.A., Plessen, B., Birgel, D., Flower, B.P., Hinrichs, K.-U., Haug, G.H., 2008. Glacial to Holocene terrigenous organic matter input to sediments from Orca Basin, Gulf of Mexico — A combined optical and biomarker approach. *Earth Planet Sci. Lett.* 272, 251–263.
- Mickler, P.J., Banner, J.L., Stern, L., Asmerom, Y., Edwards, R.L., Ito, E., 2004. Stable isotope variations in modern tropical speleothems: Evaluating equilibrium vs. kinetic isotope effects. *Geochem. Cosmochim. Acta* 68, 4381–4393.
- Mielnick, P., Dugas, W.A., Mitchell, K., Havstad, K., 2005. Long-term measurements of CO₂ flux and evapotranspiration in a Chihuahuan desert grassland. *J. Arid Environ.* 60, 423–436.
- Montero-Serrano, J.C., Bout-Roumazielles, V., Carlson, A.E., Tribouillard, N., Bory, A., Meunier, G., Sionneau, T., Flower, B.P., Martinez, P., Billy, I., Riboulleau, A., 2011. Contrasting rainfall patterns over North America during Holocene and Last Interglacial as recorded by sediments of the northern Gulf of Mexico. *Geophys. Res. Lett.* 38, L14709.
- Morrow, J.E., Fiedel, S.J., Johnson, D.L., Kornfeld, M., Rutledge, M., Wood, W.R., 2012. Pre-Clovis in Texas? A critical assessment of the “Buttermilk Creek Complex”. *J. Archaeol. Sci.* 39, 3677–3682.
- Mortlock, R.A., Fairbanks, R.G., Bloom, A., Cao, L., Wright, J.D., Abdul, N., Mey, J., Ellins, K., Teneva, L., Brainard, C., 2010. Sea Level from 1,000 to 60,000 Years BP: The Fossil Coral Record from Barbados and Araki Island. Tenth International Conference on Paleoceanography, Program and Abstracts, San Diego, CA.
- Mulitza, S., et al., 2017. Synchronous and proportional deglacial changes in Atlantic meridional overturning and northeast Brazilian precipitation. *Paleoceanography* 32, 622–633.
- Musgrove, M., Banner, J.L., Mack, L.E., Combs, D.M., James, E.W., Cheng, H., Edwards, R.L., 2001. Geochronology of late Pleistocene to Holocene speleothems from central Texas: implications for regional paleoclimate. *GSA Bull.* 113, 1532–1543.
- Myoung, B., Nielsen-Gammon, J.W., 2010. The convective instability pathway to warm season drought in Texas. Part I: the role of convective inhibition and its modulation by soil moisture. *J. Clim.* 23, 4461–4473.
- Ng, H.C., Robinson, L.F., McManus, J.F., Mohamed, K.J., Jacobel, A.W., Ivanovic, R.F., Gregoire, L.J., Chen, T., 2018. Coherent deglacial changes in western Atlantic Ocean circulation. *Nat. Commun.* 9 (1). <https://doi.org/10.1038/s41467-018-05312-3>.
- Nielsen-Gammon, J.W., Banner, J.L., Cook, B.I., Tremaine, D.M., Wong, C.I., Mace, R.E., et al., 2020. Unprecedented drought challenges for Texas water resources in a changing climate: What do researchers and stakeholders need to know? *Earth's Future* 8, e2020EF001552. <https://doi.org/10.1029/2020EF001552>.
- Nürnberg, D., Ziegler, M., Karas, C., Tiedemann, R., Schmidt, M.W., 2008. Interacting loop current variability and Mississippi river discharge over the past 400 kyr. *Earth Planet Sci. Lett.* 272, 278–289.
- Nürnberg, D., Bahr, A., Mildner, T., Eden, C., 2015. Loop current variability—Its relation to meridional overturning circulation and the impact of Mississippi discharge. In: Schulz, M., Paul, A. (Eds.), *Integrated Analysis of Interglacial Climate Dynamics*, Springer Briefs in Earth Syst. Sci. Springer International, Cham, pp. 55–62. <https://doi.org/10.1007/978-3-319-00693-2>.
- Nusbaumer, J., Alexander, P.M., LeGrande, A.N., Tedesco, M., 2019. Spatial shift of Greenland moisture sources related to enhanced Arctic warming. *Geophys. Res. Lett.* 46 (24), 14723–14731.
- Oglesby, R.J., Maasch, K.A., Saltzman, B., 1989. Glacial meltwater cooling of the Gulf of Mexico: GCM implications for Holocene and present-day climates. *Clim. Dynam.* 3, 115–133.
- Orland, I.J., Bar-Matthews, M., Ayalon, A., Matthews, A., Kozdon, R., Ushikubo, T., Valley, J.W., 2012. Seasonal resolution of Eastern Mediterranean climate change since 34 ka from a Soreq cave speleothem. *Geochem. Cosmochim. Acta* 89, 240–255.
- Orland, I.J., Edwards, R.L., Cheng, H., Kozdon, R., Cross, M., Valley, J.W., 2015. Direct measurements of deglacial monsoon strength in a Chinese stalagmite. *Geology* 43, 555–558.

- Oster, K.L., Kelley, N.P., 2016. Tracking regional and global teleconnections recorded by western North American speleothem records. *Quat. Sci. Rev.* 149, 18–33.
- Oster, J.L., Warken, S.F., Sekhon, N., Arienzo, M.M., Lachniet, M., 2019. Speleothem Paleoclimatology for the Caribbean, Central America, and North America. *Quaternary* 2 (5). <https://doi.org/10.3390/quat2010005>.
- Otto-Bliesner, B.L., Brady, E.C., 2010. The sensitivity of the climate response to the magnitude and location of freshwater forcing: last glacial maximum experiments. *Quat. Sci. Rev.* 29, 56–73.
- Overpeck, J.T., Peterson, L.C., Kipp, N., Imbrie, J., Rind, R., 1989. Climate change in the circum-North Atlantic region during the last deglaciation. *Nature* 338, 553–557.
- Pape, J.R., Banner, J.L., Mack, L.E., Musgrove, M., Guilfoyle, A., 2010. Controls on oxygen isotope variability in precipitation and cave drip waters, central Texas, USA. *J. Hydrol.* 385, 203–215.
- Pausata, F.S.R., Battisti, D.S., Nisancioglu, K.H., Bitz, C.M., 2011. Chinese stalagmite $\delta^{18}\text{O}$ controlled by changes in the Indian monsoon during a simulated Heinrich event. *Nat. Geosci.* 4, 474–480.
- Peltier, W.R., Fairbanks, R.G., 2006. Global glacial ice volume and Last Glacial Maximum duration from an extended Barbados sea level record. *Quat. Sci. Rev.* 25, 3322–3337.
- Peltier, W.R., 2005. On the hemispheric origins of meltwater pulse 1a. *Quat. Sci. Rev.* 24, 1655–1671.
- Pérez, L., Curtis, J., Brenner, M., Hodell, D., Escobar, J., Lozano, S., Schwab, A., 2013. Stable isotope values ($\delta^{18}\text{O}$ & $\delta^{13}\text{C}$) of multiple ostracod species in a large Neotropical lake as indicators of past changes in hydrology. *Quat. Sci. Rev.* 66, 96–111.
- Peterson, L.C., Haug, G.H., Hughen, K.A., Röhl, U., 2000. Rapid changes in the hydrologic cycle of the tropical Atlantic during the Last Glacial. *Science* 290, 1947–1951.
- Polyak, V.J., Asmerom, Y., 2001. Late Holocene climate and cultural changes in the southwestern United States. *Science* 294, 148–151.
- Polyak, V.J., Burns, S.J., Asmerom, Y., 2010. Variable winter moisture in the southwestern United States linked to rapid glacial climate shifts. *Nat. Geosci.* 3, 114–117.
- Polyak, V.J., Rasmussen, J.B.T., Asmerom, Y., 2004. Prolonged wet period in the southwestern United States through the Younger Dryas. *Geology* 32, 5–8.
- Poore, R.Z., Dowsett, H.J., Verardo, S., Quinn, T.M., 2003. Millennial- to century-scale variability in Gulf of Mexico Holocene climate records. *Paleoceanography* 18 (2), 1048. <https://doi.org/10.1029/2002PA000868>.
- Poore, R.Z., Quinn, T.M., Verardo, S., 2004. Century-scale movement of the Atlantic Intertropical Convergence Zone linked to solar variability. *Geophys. Res. Lett.* 31, L12214. <https://doi.org/10.1029/2004GL019940>.
- Procter, C.J., Baker, A., Barnes, W.L., Gilmore, M.A., 2000. A thousand year speleothem proxy record of North Atlantic climate from Scotland. *Clim. Dynam.* 16, 815–820.
- Qin, X., Tan, M., Liu, T., Wang, X., Li, T., Lu, J., 1999. Spectral analysis of a 1000-year stalagmite lamina-thickness record from Shihua Cavern, Beijing, China, and its climatic significance. *Holocene* 9, 689–694.
- Railsback, L.B., 2018. A comparison of growth rate of late Holocene stalagmites with atmospheric precipitation and temperatures, and its implications for paleoclimatology. *Quat. Sci. Rev.* 187, 94–111.
- Railsback, L.B., Brook, G.A., Chen, J., Kalin, R., Fleisher, C.J., 1994. Environmental controls on the petrology of a Late Holocene speleothem from Botswana with annual layers of aragonite and calcite. *J. Sediment. Res.* A64, 147–154.
- Railsback, L.B., Akers, P.D., Wang, L., Holdridge, G.A., Voarintsoa, N.R., 2013. Layer-bounding surfaces in stalagmites as keys to better paleoclimatological histories and chronologies. *Int. J. Speleol.* 42, 167–180.
- Ramseyer, K., Miano, T.M., D'Orazio, V., Wildberger, A., Wagner, T., Geister, J., 1997. Nature and origin of organic matter in carbonates from speleothems, marine cements and coral skeletons. *Org. Geochem.* 26, 361–378.
- Rasmussen, J.B.T., Polyak, V.J., Asmerom, Y., 2006. Evidence for Pacific-modulated precipitation variability during the late Holocene from the southwestern USA. *Geophys. Res. Lett.* 33, L08701.
- Rasmussen, S.O., Bigler, M., Blockley, S.P., Blunier, T., Buchardt, S.L., Clausen, H.B., Cvijanovic, I., Dahl-Jensen, D., Johnsen, S.J., Fischer, H., Gkinis, V., Guillevic, M., Hoek, W.Z., Lowe, J.J., Pedro, J.B., Popp, T., Seierstad, I.K., Steffensen, J.P., Svensson, A.M., Vallenga, P., Vinther, B.M., Walker, M.J.C., Wheatley, J.J., Winstrup, M., 2014. A stratigraphic framework for abrupt climatic changes during the Last Glacial period based on three synchronized Greenland ice-core records: refining and extending the INTIMATE event stratigraphy. *Quat. Sci. Rev.* 106, 14–28.
- Rind, D., Peteet, D., Broecker, W.S., McIntyre, A., Ruddiman, W., 1986. The impact of cold North Atlantic sea surface temperatures on climate: implications for the Younger Dryas cooling (11–10 k). *Clim. Dynam.* 1, 3–33.
- Roche, D.M., Renssen, H., Weber, S.L., Goosse, H., 2007. Could meltwater pulses have been sneaked unnoticed into the deep ocean during the last glacial? *Geophys. Res. Lett.* 34, L24708. <https://doi.org/10.1029/2007GL032064>.
- Roy, P.D., Rivero-Navarrete, A., Sánchez-Zavala, J.L., Beramendi-Orosco, L.E., Muthu-Sankar, G., Lozano-Santaruz, R., 2016. Atlantic Ocean modulated hydroclimate of the subtropical northeastern Mexico since the last glacial maximum and comparison with the southern US. *Earth Planet Sci. Lett.* 434, 141–150.
- Schwartz, B.F., Schwinning, S., Gerard, B., Kukowski, K.R., Stinson, C.L., Dammeyer, H.C., 2013. Using hydrogeochemical and ecophysiological responses to understand epikarst processes in semi-arid systems, Edwards Plateau, Texas, USA. *Acta Carsol.* 42, 315–325.
- Seager, R., Lis, N., Feldman, J., Ting, M., Williams, A.P., Nakamura, J., Liu, H., Henderson, N., 2018. Whither the 100th Meridian? The Once and Future Physical and Human Geography of America's Arid–Humid Divide. Part I: The Story So Far. *Earth Interact.* 22. <https://doi.org/10.1175/EI-D-17-00111>.
- Severinghaus, J.P., Brook, E.J., 1999. Abrupt Climate Change at the End of the Last Glacial Period Inferred from Trapped Air in Polar Ice. *Science* 286, 930–934.
- Shakun, J.D., Burns, S.J., Fleitmann, D., Kramers, J., Matter, A., Al-Subary, A., 2007. A high-resolution, absolute-dated deglacial speleothem record of Indian Ocean climate from Socotra Island, Yemen. *Earth Planet Sci. Lett.* 259, 442–456.
- Shopov, Y.Y., Ford, D.C., Schwarcz, H.P., 1994. Luminescent microbanding in speleothems: High-resolution chronology and palaeoclimate. *Geology* 22, 407–410.
- Sinha, A., Cannariato, K.G., Stott, L.D., Li, H.-C., You, C.-F., Cheng, H., Edwards, R.L., Singh, I.B., 2005. Variability of southwest Indian summer monsoon precipitation during the Bolling-Allerod. *Geology* 33, 813–816.
- Slade, R.M., Patton, J., 2003. Major and Catastrophic Storms and Floods in Texas. Open-File Report – US Geological Survey, OF 03-0193.
- Stanford, J.D., Rohling, E.J., Hunter, S.E., Roberts, A.P., Rasmussen, S.O., Bard, E., McManus, J., Fairbanks, R.G., 2006. Timing of meltwater pulse 1a and climate responses to meltwater injections. *Paleoceanography* 21, PA4103. <https://doi.org/10.1029/2006PA001340>.
- Stoll, H.M., Moreno, A., Mendez-Vicente, A., Gonzalez-Lemos, S., Jimenez-Sanchez, M., Dominguez-Cuesta, M.J., Edwards, R.L., Cheng, H., Wang, X., 2013. Paleoclimate and growth rates of speleothems in the northwestern Iberian Peninsula over the last two glacial cycles. *Quat. Res.* 80, 284–290.
- Sun, C., Shanahan, T.M., Partin, J., 2019. Controls on the isotopic composition of precipitation in the south-central United States. *J. Geophys. Res.: Atmospheres* 124, 8320–8335. <https://doi.org/10.1029/2018JD029306>.
- Sun, C.J., Shanahan, T., Tian, L., Partin, J., Gao, Y., Piatrunia, N., and Banner, J. in review. Controls on the Isotopic Composition of Precipitation during Tropical Cyclones and Implications for Paleotempestology. *Communications Earth & Environment*.
- Tan, M., Baker, A., Genty, D., Smith, C., Esper, J., Cai, B., 2006. Applications of stalagmite laminae to paleoclimate reconstructions: Comparison with dendrochronology/climatology. *Quat. Sci. Rev.* 25, 2103–2117.
- Tarasov, L., Peltier, W.R., 2005. Arctic freshwater forcing of the Younger Dryas cold reversal. *Nature* 435, 662–665.
- Tarasov, L., Dyke, A.S., Neal, R.M., Peltier, W.R., 2012. A data-calibrated distribution of deglacial chronologies for the North American ice complex from glaciological modeling. *Earth Planet Sci. Lett.* 315–316, 30–40.
- Toomey, R.S., Blum, M.D., Valastro, S., 1993. Late Quaternary climates and environments of the Edwards Plateau, Texas. *Global Planet. Change* 7, 299–320.
- Tremaine, D.M., Froelich, P.N., Wang, Y., 2011. Speleothem calcite formed in situ: Modern calibration of $\delta^{18}\text{O}$ and $\delta^{13}\text{C}$ paleoclimate proxies in a continuously-monitored natural cave system. *Geochim. Cosmochim. Acta* 75, 4929–4950.
- Uccellini, L.W., Johnson, D.R., 1979. The coupling of upper and lower tropospheric jet streaks and implications for the development of severe convective storms. *Mon. Weather Rev.* 107, 682–703.
- US Climate Data, 2021. www.usclimatedata.com/climate/boerne.
- van Beynen, P., Polk, J.S., Asmerom, Y., Polyak, V., 2017. Late Pleistocene and mid-Holocene climate change derived from a Florida speleothem. *Quat. Int.* 449, 75–82.
- van der Ent, R.J., Savenije, H.H.G., 2013. Oceanic sources of continental precipitation and the correlation with sea surface temperature. *Water Resour. Res.* 49, 3993–4004.
- van der Ent, R.J., Savenije, H.H.G., Schaeffli, B., Steele-Dunne, S.C., 2010. Origin and fate of atmospheric moisture over continents. *Water Resour. Res.* 46, W09525. <https://doi.org/10.1029/2010WR009127>.
- Veni, G., 1994. Geomorphology, Hydrogeology, Geochemistry, and Evolution of the Karstic Lower Glen Rose Aquifer, South-Central Texas. Department of Geosciences, Pennsylvania State University, p. 721. Doctoral Dissertation.
- Vetter, L., Spero, H.J., Eggins, S.M., Williams, C., Flower, B.P., 2017. Oxygen isotope geochemistry of Laurentide ice-sheet meltwater across Termination I. *Quat. Sci. Rev.* 178, 102–117.
- Wagner, J.D.M., Cole, J.E., Beck, J.W., Patchett, P.J., Henderson, G.M., Barnett, H.R., 2010. Moisture variability in the southwestern United States linked to abrupt glacial climate change. *Nat. Geosci.* 3, 110–113.
- Wang, C., Enfield, D.B., 2001. The tropical Western Hemisphere warm pool. *Geophys. Res. Lett.* 28, 1635–1638.
- Wang, C., Fiedler, P.C., 2006. ENSO variability and the eastern tropical Pacific: a review. *Prog. Oceanogr.* 69, 239–266.
- Wang, H., Fu, R., 2007. The influence of Amazon rainfall on the Atlantic ITCZ through convectively coupled Kelvin waves. *J. Clim.* 20, 1188–1201.
- Wang, Y., Cheng, H., Edwards, R.L., Kong, X., Shao, X., Chen, S., Wu, J., Jiang, Z., Wang, X., An, Z., 2008. Millennial- and orbital-scale changes in the East Asian monsoon over the past 224,000 years. *Nature* 451, 1090–1093.
- Wang, Y.J., Cheng, H., Edwards, R.L., An, Z.S., Wu, J.Y., Shen, C.-C., Dorale, J.A., 2001. A high-resolution absolute-dated late Pleistocene monsoon record from Hulu Cave, China. *Science* 294, 2345–2348.
- Warken, S.F., Scholz, D., Spötl, C., Jochum, K.P., Pajón, J.M., Bahr, A., Mangini, A., 2019. Caribbean hydroclimate and vegetation history across the last glacial period. *Quat. Sci. Rev.* 218, 75–90.
- Water Data for Texas, 2021. <https://waterdatafortexas.org/drought/pdsi/monthly?time=2021-04>.
- Waters, M.R., Forman, S.L., Jennings, T.A., Nordt, L.C., Driese, S.G., Feinburg, J.M.,

- Keene, J.L., Halligan, J., Lindquist, A., Pierson, J., Hallmark, C.T., Collins, M.B., Wiederhold, J.E., 2011. The Buttermilk Creek complex and the Origins of Clovis at the Debra L. Friedkin site, Texas. *Science* 331, 1599–1603.
- Weaver, A.J., Saenko, O.A., Clark, P.U., Mitrovica, J.X., 2003. Meltwater Pulse 1A from Antarctica as a Trigger of the Bølling-Allerød Warm Interval. *Science* 299, 1709–1713.
- Webster, J.M., Clague, D.A., Riker-Coleman, K.E., Gallup, C.D., Potts, D.C., Paull, C.K., 2004. Drowning of the 2150 m reef off Hawaii: a casualty of global meltwater pulse 1A? *Geology* 32, 249–252.
- Weiss, J.L., Overpeck, J.T., Cole, J.E., 2012. Warmer led to drier: Dissecting the 2011 drought in the southern U.S. Southwest. *Climate Outlook* 11, 3–4.
- Whitehouse, P.L., Bentley, M.J., Le Brocq, A.M., 2012. A deglacial model for Antarctica: geological constraints and glaciological modelling as a basis for a new model of Antarctic glacial isostatic adjustment. *Quat. Sci. Rev.* 32, 1–24.
- Williams, C., Flower, B.P., Hastings, D.W., 2012. Seasonal Laurentide Ice Sheet-melting during the “Mystery Interval” (17.5–14.5 ka). *Geology* 40, 955–958.
- Williams, C., Flower, B.P., Hastings, D.W., Guilderson, T.P., Quinn, K.A., Goddard, E.A., 2010. Deglacial abrupt climate change in the Atlantic Warm Pool: a Gulf of Mexico perspective. *Paleoceanography* 25, PA4221. <https://doi.org/10.1029/2010pa001928>.
- Williams, D.F., 1984. Correlation of Pleistocene marine sediments of the Gulf of Mexico and other basins using oxygen isotope stratigraphy. In: Healy-Williams, N. (Ed.), *Principles of Pleistocene Stratigraphy Applied to the Gulf of Mexico*. Int. Human Resour. Dev. Corp., Boston, Mass, pp. 65–118.
- Wong, C.I., Banner, J.L., Musgrove, M., 2015. Holocene climate variability in Texas, USA: An integration of existing paleoclimate data and modeling with a new, high-resolution speleothem record. *Quat. Sci. Rev.* 127, 155–173.
- Wong, C., Banner, J.L., 2010. Response of cave air CO₂ and drip water to brush clearing in central Texas: Implications for recharge and soil CO₂ dynamics. *J. Geophys. Res.* 115. <https://doi.org/10.1029/2010JG001301>.
- Wong, C.I., Banner, J.L., Musgrove, M., 2011. Seasonal dripwater Mg/Ca and Sr/Ca variations driven by cave ventilation: Implications for and modeling of speleothem paleoclimate records. *Geochem. Cosmochim. Acta* 75, 3514–3529.
- Wycech, J.B., Kelly, D.C., Kozdon, R., Orland, I.J., Spero, H.J., Valley, J.W., 2018. Comparison of $\delta^{18}\text{O}$ analyses on individual planktic foraminifer (*Orbulina universa*) shells by SIMS and gas-source mass spectrometry. *Chem. Geol.* 483, 119–130.
- Xia, Q.K., Zhao, J.X., Collerson, K.D., 2001. Early-Mid Holocene climatic variations in Tasmania, Australia: multi-proxy records in a stalagmite from Lynds cave. *Earth Planet Sci. Lett.* 194, 177–187.
- Zhao, J.-X., Xia, Q.K., Collerson, K.D., 2001. Timing and duration of the Last Interglacial inferred from high resolution U-series chronology of stalagmite growth in Southern Hemisphere. *Earth Planet Sci. Lett.* 184, 633–644.
- Ziegler, M., Nürnberg, D., Karas, C., Tiedemann, R., Lourens, L.J., 2008. Persistent summer expansion of the Atlantic Warm Pool during glacial abrupt cold events. *Nat. Geosci.* 1, 601–606.